KU LEUVEN

ARENBERG DOCTORAL SCHOOL
FACULTY OF BIOSCIENCE ENGINEERING

Gas exchange modeling in fruit using diffusivity maps computed from X-ray CT images

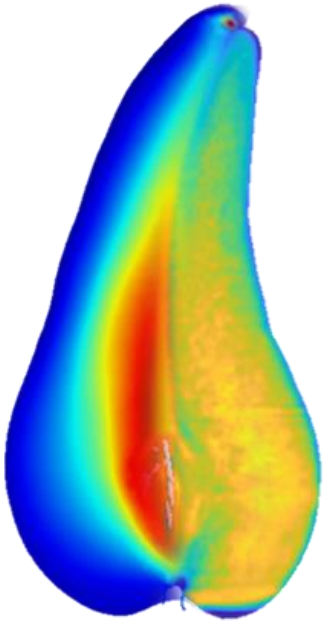

Bayu NUGRAHA

Supervisors:
Prof. dr. ir. Bart Nicolaï
Dr. ir. Pieter Verboven

Dissertation presented in partial fulfilment of the requirements for the degree of Doctor of Bioscience Engineering (PhD)

September 2021

GAS EXCHANGE MODELING IN FRUIT USING DIFFUSIVITY MAPS COMPUTED FROM X-RAY CT IMAGES

Bayu NUGRAHA

Supervisors:

Prof. Bart Nicolaï
Dr. Pieter Verboven

Members of the Examination Committee:

Prof. René De Mot, Chair
Prof. Wouter Saeys
Prof. Dany Bylemans
Prof. Matthieu Boone (Gent University)
Dr. Dorien Vanhees

Dissertation presented in partial fulfilment of the requirements for the degree of Doctor of Bioscience Engineering (PhD)

September 2021

Doctoraatsproefschrift nr. 1722 aan de faculteit Bio-ingenieurswetenschappen van de KU Leuven

© 2021 BAYU NUGRAHA
Uitgegeven in eigen beheer, Bayu Nugraha, Willem de Croylaan 42, B-3001 Leuven, Belgium

Alle rechten voorbehouden. Niets uit deze uitgave mag worden vermenigvuldigd en/of openbaar gemaakt worden door middel van druk, fotokopie, microfilm, elektronisch of op welke andere wijze ook zonder voorafgaandelijke schriftelijke toestemming van de uitgever.

All rights reserved. No part of the publication may be reproduced in any form by print, photoprint, microfilm, electronic or any other means without written permission from the publisher.

Acknowledgements

Alhamdulillah, all praises to Allah SWT for His loves, blessings and mercies in helping me to finish in this PhD study.

First and foremost, I offer my sincere gratitude to my promotor Prof. Bart Nicolaï for giving me a great opportunity to pursue a doctoral degree at his research group. His wisdom and advice have made this long PhD journey running smoothly. Likewise, I am extremely grateful to my supervisor Dr. Pieter Verboven who consistently guided and supported me to complete my PhD study in these past few years.

I am also thankful to the members of examination committee Prof. René De Mot (chair), Prof. Wouter Saeys, Prof. Dany Bylemans, Prof. Matthieu Boone and Dr. Dorien Vanhees. I greatly appreciate their enthusiasm in my PhD topic, taking time out of their schedules to provide constructive suggestions and comments to improve this PhD dissertation.

Furthermore, a big thank to all my colleagues and friends in postharvest group, KU Leuven, and in Indonesian Student Association (PPI) Belgium for helps, supports, discussions and fun talks during the free times.

I specially thank all my family members, especially my parents (Mamah, Ibu, Bapak), my wife Qurrotul Ayun and my son Rafka Y. Nugraha, for their prayer and never-ending support.

Gent, September 2021

Abstract

Decreased O_2 and slightly increased CO_2 partial pressures of controlled atmosphere (CA) storage slow down the postharvest respiration processes of pear and apple fruit and, therefore, ensure their year round availability. While the O_2 partial pressures of the storage atmosphere can be precisely controlled, gas diffusion resistance of the fruit tissue and O_2 consumption may create too low O_2 levels inside the fruit, potentially leading to the development of internal physiological disorders. To understand the effect of hypoxic storage on the physiology of the fruit, the O_2 level inside the fruit needs to be known. A modeling approach is so far the best option since the direct measurement of internal gas concentration of fruit is destructive and not practical. Available gas transport models for O_2 typically assume a homogeneous gas transport parameter. However, there is now evidence that fruit tissue microstructure is quite heterogeneous over the entire fruit and this would likely result in a heterogeneous gas diffusivity. In this dissertation, the heterogeneity of the tissue microstructure is mapped based on X-ray computed tomography (CT) images and integrated into existing respiratory gas exchange models to investigate its effect on the O_2 concentration inside the fruit.

A method was developed to create three dimensional (3D) porosity maps. The method was based on a regression model between the grayscale intensity of low resolution CT images and the actual tissue porosity at identical locations. The latter was calculated from high resolution CT images of the same tissue in which pores and cells could be distinguished. The model was constructed for four products that have considerably different tissue microstructures; pear, apple, eggplant and turnip. Grayscale values of juice of the sample and air representing 0 and 100 % porosity, respectively, were included in the data as extreme values. Using the model, the porosity distribution could be mapped based on juice scans only. The constructed porosity maps reflect the heterogeneity of the tissue microstructure both within and between products.

The porosity mapping method was then extended to create effective O_2 diffusivity maps. A model for relating the effective O_2 diffusivity to the total porosity was developed for the same products. The model did not predict the O_2 diffusivity well in regions with low connectivity and/or high tortuosity of the pore microstructure. The relationship between the O_2 diffusivity and the open porosity and tortuosity was, therefore, also explored. The O_2 diffusivity was calculated based on a microscale gas transport model; the total and open porosity and tortuosity were derived from segmented high resolution images of tissues sampled along radial direction of the product. The O_2 diffusivity correlated better with the open than total porosity. The addition of the tortuosity in the model did not improve the fit of the correlation. For eggplant and turnip the model based on total porosity was sufficiently accurate as these products consist of more open and less tortuous pores. On the other hand, better results were obtained with the model based on open porosity for pear and apple which have less open channels. An open porosity map was, therefore, estimated for intact apple and pear fruit using a regression model between total porosity and open porosity. Finally, maps of effective O_2 diffusivity coefficients were calculated for apple, pear, eggplant and turnip based on the previously created porosity maps.

The O_2 diffusivity maps were then used to study gas transport in 'Conference' pear and its impact on internal browning. Late harvested pear fruit were stored under CA with browning-inducing conditions: no pre-cooling period, 0.5 kPa O_2, 0.7 kPa CO_2 at 1 ^oC. Porosity and effective O_2 diffusivity distributions were mapped in pears before and after storage using the developed methods. The effective CO_2 diffusivity were used in respiratory gas exchange calculations to obtain the spatial distribution of the O_2 and CO_2 concentration and the respiratory quotient (RQ) in the fruit. The resulting concentration contours were quite heterogeneous and the low oxygen concentrations and high RQ values found in the core region of the fruit indicated the occurrence of fermentation. Moreover, the gas concentration and RQ contours corresponded well with tissue that was affected by browning and cavities after 8-months storage. In contrast, when

homogeneous O_2 and CO_2 diffusivities were used for computing the internal gas and RQ distributions, smooth contours were obtained that did not correspond to contours of the tissue affected by browning and cavities; nowhere the thresholds indicative for the development of browning were exceeded.

In future research, the porosity mapping technique may be integrated into inline systems of fruit quality sorting based on X-ray radiography and tomography, although this will require significant further research in terms of optimizing speed and cost of the systems and development of adequate processing algorithm for inline applications. For the diffusivity mapping, more complex multiphase transport models and orthotropic diffusivity tensors should be considered to describe gas transport more appropriately, compared to a local isotropic diffusivity. Furthermore, the gas transport models should be validated using appropriate methods. The developed and validated models can then be extended to other respiration-related gasses. Finally, browning-related change of respiration, tissue microstructure and, inherently, effective tissue diffusivity during storage should be further investigated to explore the dynamic change of internal gas distribution.

Beknopte samenvatting

Verlaagde O_2 en licht verhoogde CO_2 partieeldrukken tijdens gecontroleerde atmosfeer (CA) bewaring vertragen de respiratieprocessen van appel en peer fruit na de oogst en verzekeren zo hun beschikbaarheid het hele jaar door. Hoewel de O_2 partieeldruk in de bewaaromgeving nauwkeurig gecontroleerd kan worden, kunnen de diffusieweerstand voor gassen O_2 consumptie van het fruitweefsel zorgen voor te lage O_2 niveaus binnenin het fruit, wat potentieel kan leiden tot de ontwikkeling van interne fysiologische defecten. Om het effect van zuurstofarme bewaring op de fysiologie van het fruit te begrijpen, moet het zuurstofniveau in de vrucht gekend zijn. Op dit ogenblik is een benadering op basis van modellen de beste optie, aangezien de directe meting van de interne gasconcentratie van fruit destructief en onpraktisch is. De beschikbare gastransportmodellen voor O_2 en CO_2 veronderstellen typisch een homogene effectieve diffusiviteit van het weefsel. Er zijn echter aanwijzingen dat de microstructuur van fruitweefsel heterogeen is over de volledige vrucht, wat vermoedelijk ook resulteert in een heterogene gasdiffusiviteit. In dit proefschrift wordt de heterogeniteit van de weefselmicrostructuur en -diffusiviteit in kaart gebracht, gebaseerd op X-ray computed tomography (CT) beelden en geïntegreerd in bestaande respiratoire gasuitwisselingsmodellen, om het effect hiervan op de O_2-en CO_2-concentratie in vruchten te onderzoeken.

Er werd een methode ontwikkeld om driedimensionale (3D) porositeitskaarten te genereren. De methode is gebaseerd op een lineair regressiemodel dat de grijswaarde-intensiteit van lage resolutie CT-beelden linkt aan de werkelijke porositeit van het weefsel op dezelfde locatie. Deze laatste werd berekend op basis van hoge resolutie CT-beelden van dezelfde weefsels, waarin poriën en cellen onderscheiden kunnen worden. Het model werd opgesteld voor vier tuinbouwproducten met een aanzienlijk verschillende microstructuur van hun weefsels; peer, appel, aubergine en knolraap. De grijswaarden van het sap van elk staal, alsook de lucht, die respectievelijk een porositeit van 0 en 100%

vertegenwoordigen, werden meegenomen in de data als extreme waarden. Gebruik makend van het model kon de porositeitsverdeling vervolgens bepaald worden op basis van de sap scans alleen. De porositeitskaarten geven de heterogeniteit van de microstructuur van het weefsel weer, zowel binnenin elk product als tussen de verschillende producten onderling.

De methode om porositeitskaarten te maken werd vervolgens uitgebreid om kaarten van de effectieve zuurstofdiffusiviteit te genereren. De O_2-diffusiviteit werd berekend op basis van een microschaal gastransport model opgelost met de hoge resolutie CT beelden. Een regressiemodel dat de effectieve O_2-diffusiviteit koppelt aan de totale porositeit van het weefsel werd ontwikkeld met data van de bovenvermelde producten. Het model was echter niet in staat om de O_2-diffusiviteit goed te voorspellen weefsel met een lage connectiviteit en/of een hoge tortuositeit van de poriën in de microstructuur. De verbanden tussen de O_2-diffusiviteit en open porositeit (die enkel de geconnecteerde poriën in rekening brengt) en de tortuositeit werden daarom ook verder onderzocht. De totale en open porositeit en de tortuositeit werden afgeleid uit gesegmenteerde hoge resolutie CT beelden van weefsels gesampled langsheen de radiale richting van elke van de producten. De O_2-diffusiviteit correleerde beter met de open dan met de totale porositeit. De tortuositeit toevoegen aan het model verbeterde de fit van de correlatie echter niet. Voor aubergine en knolraap was het model gebaseerd op totale porositeit voldoende nauwkeurig, aangezien deze producten meer open en minder tortueuze poriën bevatten. Anderzijds werden voor peer en appel, die minder open poriekanalen hebben, betere resultaten verkregen met het model gebaseerd op open porositeit. Daarom werd een open porositeitskaart geschat voor vruchten van appel en peer, die gebruik maakt van een correlatie model tussen totale en open porositeit. Tenslotte werden kaarten van de effectieve zuurstofdiffusiviteit berekend voor appel, peer, aubergine en knolraap, gebaseerd op de eerder gemaakte porositeitskaarten.

De O_2-diffusiviteitskaartenwerden vervolgens gebruikt voor het bestuderen van gastransport in ‘Conference’ peer en de impact op interne bruining. Laat geplukte peren werden opgeslagen onder gecontroleerde atmosfeer condities die bruinverkleuring induceren: zonder voorkoelingsperiode gingen de peren meteen op zeer lage zuurstofbewaring bij 0.5 kPa O_2, 0.7 kPa CO_2 bij 1°C. De porositeits- en effectieve O_2-diffusiviteitskaarten van de peren voor en na bewaring werden aangemaakt met behulp van de ontwikkelde methoden. Ook de verdeling van de effectieve CO_2-diffusiviteit werd gebruikt in de berekening van de respiratoire gasuitwisseling, om zo de ruimtelijke verdeling van de O_2- en CO_2-concentraties en het respiratie-quotiënt (RQ) in het fruit te bekomen. De resulterende gasconcentraties waren vrij heterogeen verdeeld. De lage zuurstofconcentraties en hoge RQ waarden, die gevonden konden worden in de kern van de vruchten, duidden op het voorkomen van fermentatie. Bovendien kwamen de contouren van de kritische gasconcentraties en RQ-waarden goed overeen met de zones in de vrucht die aangetast waren door bruinverkleuring en holtevorming na 8 maanden bewaring. Daartegenover, wanneer homogene O_2- en CO_2-diffusiviteiten werden gebruikt om de interne gas en RQ verdelingen te berekenen, werd een meer homogene verdeling van gassen en RQ verkregen die niet overeenstemden met de aantastingspatronen na bewaring; nergens werden de drempelwaarden die duiden op de ontwikkeling van bruinverkleuring overschreden.

In de toekomst kan de techniek van porositeitskaarten geïntegreerd worden in inline systemen voor het sorteren van fruit op basis van interne kwaliteit die gebruik maken van X-stralen radiografie en tomografie, hoewel dit nog aanzienlijk verder onderzoek zal vereisen op het gebied van optimalisatie van de snelheid en de kost van de huidige systemen en de ontwikkeling van adequate verwerkingsalgoritmes voor inline toepassingen. Met betrekking tot de diffusiviteitskaarten moeten complexere meerfazige transportmodellen en orthotropische diffusiviteitstensoren overwogen worden om de relatie tussen het gastransport en de lokale (an)isotrope diffusiviteit nauwkeuriger te beschrijven.

Verder moeten de gastransportmodellen gevalideerd worden, gebruik makend van geavanceerde methoden die profielen van de gasconcentraties in de vruchten kunnen meten. De ontwikkelde en gevalideerde modellen kunnen verder uitgebreid worden naar andere respiratie-gerelateerde gassen. Tot slot moeten aan bruinverkleuring -gerelateerde respiratieveranderingen, weefselmicrostructuur en, noodzakelijkerwijs, effectieve weefseldiffusiviteit tijdens de bewaring verder onderzocht worden om de dynamische veranderingen van de interne gasverdeling beter te begrijpen.

List of symbols

Abbreviations

1D	One dimensional
2D	Two dimensional
3D	Three dimensional
ACP	Anaerobic compensation point
ADH	Alcohol dehydrogenase
ATP	Adenosine triphosphate
BHC	Beam hardening correction
CA	Controlled atmosphere
CDP	Carbon dioxide production
CF	Chlorophyll fluorescence
CR	Core region
CT	Computed tomography
CTs	Cortex tissue
DCA	Dynamic controlled atmosphere
DEM	Discrete element method
CDP	Carbon dioxide production
EDC	Endocarp
EPC	Epicarp
ET	Ethanol production
FOV	Field of view
FT	Fermentation threshold

LDH	Lactate dehydrogenase
LOL	Lower oxygen limit
MMD	Microscale model-based diffusivity
MRI	Magnetic resonance imaging
OP	Open porosity
OPD	Open porosity-based diffusivity
PDC	Pyruvate decarboxylase
PE	Pedicle end
PPO	Polyphenoloxidase
REV	Representative elementary volume
RMSE	Root mean square error
ROI	Region of interest
RPP	Radial porosity profile
S	Seeds
SD	Standard deviation
SE	Standard error
TCA	Tricarboxylic acid
TEM	Transmission electron microscopy
TDP	Total porosity-based diffusivity
TP	Total porosity
UD	Uniform or single diffusivity
ULO	Ultra low oxygen
VB	Vascular bundle

VOI	Volume of interest

Symbols

A	Tissue area (m^2)
CO_2	Carbon dioxide
C_i	Concentration of component *i* (mol m^{-3})
D_i	Diffusivity of component *i* (m^2 s^{-1})
d	Diameter (m)
$E_{a,V_{m,O_2}}$	Activation energy for O_2 consumption (kJ mol^{-1})
$E_{a,V_{m,f,CO_2}}$	Activation energy for fermentative CO_2 production (kJ mol^{-1})
f_o	Stoichiometric coefficient of ATP production due to respiration
f_f	Stoichiometric coefficient of ATP production due to fermentation
g	Grayscale intensity
H_i	Henry's constant for component *i* (mol m^{-3} Pa^{-1})
H_2O	Water
I	Transmitted X-ray intensity
I_0	Incident X-ray intensity
K	Tissue permeability (m^2)
K_{m,O_2}	Michaelis-Menten constant for O_2 consumption (mol m^{-3})
K_{mn,CO_2}	Michaelis-Menten constant for non-competitive inhibition by CO_2 (mol m^{-3})
K_{m,f,O_2}	Michaelis-Menten constant for the inhibition of O_2 on fermentative CO_2 production (mol m^{-3})

L	Thickness of tissue (m)
n	Mass flow rate (mol s^{-1})
N_2	Nitrogen
O_2	Oxygen
P	Pressure (Pa)
P	Percentage (%)
P_i	Permeability of component i (m s^{-1})
p	Probability
R	Universal gas constant (Pa m^3 mol^{-1} K^{-1})
R_i	Respiration rate for component i (mol m^{-3} s^{-1})
RQ	Respiratory quotient
r	Radius (m)
$r_{q,ox}$	Respiration quotient at high O_2 levels
T	Temperature (K)
t	Time (s)
$\mathbf{u}$	Convective velocity vector (m s^{-1})
V	Volume (m^3)
V_{m,O_2}	Maximal O_2 consumption rate of the tissue (mol m^{-3} s^{-1})
V_{m,f,CO_2}	Maximal fermentative CO_2 production rate of the tissue (mol m^{-3} s^{-1})
x	Actual length of pore channel (mm)

Greek Symbols

α_i	Tissue gas capacity
Δ	Difference
ε	Total porosity of tissue
ε_o	Open porosity of tissue
ε_c	Closed porosity of
$\varepsilon_{c,l}$	Porosity of tissue without open pores
μ	Gas viscosity (Pa s)
μ_E	Attenuation coefficient
τ	Tortuosity
$\Omega(E)$	Energy spectrum
∇	Gradient operator (m^{-1})

Sub- and superscripts

*	Critical value
at	Affected tissue (browning and cavities)
c	Closed
b	Brown tissue
c	Cavities
E	Energy dependency
eff	Effective
g	Gas phase
l	Liquid phase

m	Cell membrane
n	Fitting parameter of model
o	Open
p	Pear
S	Path of X-ray beam
w	Cell wall

Contents

Acknowledgements ..... **i**

Abstract ..... **ii**

Beknopte samenvatting ..... **v**

List of symbols ..... **ix**

Contents ..... **xv**

1 General introduction **1**

1.1 Problem statement 1

1.2 Objectives and outline of the thesis 3

2 Literature review **7**

2.1 Introduction 7

2.2 Fruit and vegetables 8

2.2.1 Anatomy of selected fruit and vegetables 8

2.2.2 Microstructure 11

2.2.3 Respiration 16

2.3 Storage of fruit and vegetables 19

2.3.1 Controlled atmosphere storage 19

2.3.2 Internal browning disorder 21

2.4 Modeling of respiratory gas exchange 23

2.4.1 Reaction-diffusion-permeation models for gas transport in pome fruit 23

2.4.2 Models for effective transport parameters 28

2.5 Microstructure analysis and modeling 31

2.5.1 X-ray computed tomography (CT) 31

2.5.2 CT image reconstruction 33

2.5.3 CT image processing 35

2.5.4 X-ray CT factors 36

2.5.5 Geometrical models of fruit microstructure 40

2.5.6 Geometrical model of entire fruit 42

2.6 Conclusion ... 43
3 Non-destructive porosity mapping of fruit and vegetables using X-ray CT ... 45
3.1 Introduction ... 45
3.2 Materials and methods ... 48
3.2.1 Samples ... 48
3.2.2 X-ray computed tomography ... 48
3.2.3 Reconstruction and image processing ... 51
3.2.4 Regression analysis ... 53
3.2.5 Statistical analysis ... 54
3.3 Results ... 54
3.3.1 Beam hardening correction (BHC) implementation ... 54
3.3.2 Correlation between grayscale intensity and porosity ... 55
3.3.3 Radial porosity profile (RPP) ... 57
3.3.4 Porosity map of fruit and vegetables ... 59
3.4 Discussion ... 62
3.5 Conclusions ... 65
4 Oxygen diffusivity mapping of fruit and vegetables based on X-ray CT ... 67
4.1 Introduction ... 67
4.2 Materials and methods ... 69
4.2.1 Approach ... 69
4.2.2 Sample ... 71
4.2.3 X-ray CT scans and image processing ... 71
4.2.4 Calculation of tissue structure properties ... 72
4.2.5 Effective O_2 diffusivity ... 73
4.2.6 Model of effective O_2 diffusivity ... 76
4.2.7 Relation between open and total porosity ... 78
4.2.8 Model Testing ... 78
4.2.9 Mapping effective O_2 diffusivity ... 79
4.3 Results ... 79

4.3.1 Profiles of total and open porosity, tortuosity and effective O_2 diffusivity 79
4.3.2 Effective O_2 diffusivity versus total porosity 81
4.3.3 Effective O_2 diffusivity versus open porosity 83
4.3.4 Effect of pore tortuosity on effective O_2 diffusivity 83
4.3.5 Radial profile of the diffusivity based on total porosity 84
4.3.6 Open porosity prediction 85
4.3.7 Radial profile of the diffusivity based on open porosity 87
4.3.8 Map of effective O_2 diffusivity 88
4.4 Discussion 89
4.5 Conclusions 94
5 Gas exchange model using effective diffusivity map to study internal browning in 'Conference' pear 97
5.1 Introduction 97
5.2 Materials and methods 99
5.2.1 Pear fruit 99
5.2.2 X-ray CT scans and 3D pear geometry construction 99
5.2.3 Regression model linking the effective O_2 and CO_2 diffusivities 100
5.2.4 Mapping of effective O_2 and CO_2 diffusivities 102
5.2.5 Internal browning segmentation 102
5.2.6 Respiratory gas exchange model for intact fruit 103
5.2.7 Gas exchange simulation using effective diffusivity maps 106
5.2.8 Critical oxygen level 106
5.3 Results 108
5.3.1 Incidence of internal breakdown after storage 108
5.3.2 Map of effective O_2 and CO_2 diffusivity 110
5.3.3 Gas exchange simulations 113
5.3.4 Difference between map and uniform diffusivity-based simulations 117
5.3.5 Critical O_2 limit and internal browning occurrence 119
5.4 Discussion 120

5.5 Conclusions 124
6 General conclusions and future perspectives 125
6.1 General conclusions 125
6.2 Future perspectives 126
Appendix A 129
A.1. Representative elementary volume (REV) analysis 129
A.2. Correlation of total porosity versus open porosity for eggplant and turnip 133
A.3. Relation of effective O_2 diffusivity to grayscale intensity 134
A.4. Oxygen concentration profiles 135
Appendix B 136
B.1. Effect of permeation on internal O_2 concentration 136
B.2. O_2 diffusivity profiles of the original and binned maps 137
B.3. Porosity map of sound and affected pears 138
B.4. Profiles of porosity, O_2 and CO_2 diffusivities 139
References 141

Chapter 1

General introduction

1.1 Problem statement

Consumption of fruit and vegetables helps individuals to fulfill their daily requirements for dietary fibers, vitamins and minerals (Wallace *et al*., 2020). Both the WHO and FAO recommend adults to consume at least 2 servings of fruit and 3 servings of vegetables per day to reduce the risk of major chronic diseases (Nishida et al., 2004; USDA, 2015). Therefore, a sufficient supply of high-quality fruit and vegetables has become important in all countries.

In terms of total production volume, Belgium ranks 11th in the European Union (EU) for both fruit and vegetables (Fruit Logistica, 2020). Belgian fruit production is dominated by apple (*Malus x domestica* Borkh.) and pear (*Pyrus communis* L.) with 331,000 and 229,000 tons in 2019, respectively. A large part is exported to other EU countries and more to non-EU countries around the world. Year-round supply of apples and pears to long term storage to Belgian consumption and distant markets remains a challenge. As the fruit stay alive and continue their respiratory metabolism after harvest, they may undergo unexpected fast deterioration before reaching the consumers. Degradation of initial fruit quality is to be anticipated. To ensure year round availability of high quality fruit, continuous innovation efforts are required to prolong the fruit storage and shelf life with minimal quality loss.

Controlled atmosphere (CA) storage has become a popular commercial storage procedure to preserve pome fruit for a long term before being marketed. In CA storage, the respiration rate and respiration-dependent metabolism are slowed down by decreasing oxygen (O_2) and slightly increasing carbon dioxide (CO_2) partial pressures in the storage headspace, in combination with low temperature. The decreased O_2 partial pressure is maintained well above the low O_2 limit below which a switch of aerobic respiration to fermentation may occur. As the

lower O_2 limit of the plant tissues varies over different conditions (Ho *et al*., 2016), the constant O_2 partial pressure applied in CA storage is set safely above the limit, but sub-optimal to preserve the fruit quality. More advanced versions of CA storage, so-called dynamic CA (DCA) techniques, have been proposed. In DCA, the O_2 level of the storage atmosphere is dynamically adapted based on a biological signal indicating the low O_2 limit of the fruit, so that a more optimal O_2 partial pressure can be achieved to better maintain quality while avoiding low oxygen storage disorders (Bessemans *et al*., 2016, 2020).

While the gas partial pressures in the storage atmosphere can be precisely measured and controlled, the diffusion resistance presented by skin and cortex tissue of the fruit leads to steep O_2 and CO_2 gradients inside the fruit (Ho *et al*., 2010a,b, 2011) that are invasively difficult to measure inside a storage room. The internal gradients potentially create localized hypoxic or anoxic conditions inside the fruit, depending on its metabolic activity and structural properties (Ho *et al*., 2011, 2013b, 2016). Such a condition may cause an imbalance in the energy metabolism and lead to the production of off-flavors (Boeckx *et al*., 2019), gradually triggering cell breakdown and disorders such as internal browning (Franck *et al*., 2007). Information on the internal gas composition is, therefore, a key factor to know the critical concentration limit of the gasses and improve CA and DCA storage applications. Thereto, reliable determination of the gas composition inside the fruit is required.

Invasive measurements of internal gas concentration have been conducted using gas sensor probes inserted into the fruit, but such a measurement may locally induce tissue damages affecting the respiration activities and the measured gas levels. *In-silico* estimation/simulation of gas concentrations based on respiratory gas exchange models is a viable non-destructive alternative (Ho *et al*., 2010a,b, 2011). Using a so-called multiscale modeling approach, the effect of the fruit (micro)structural properties, such as porosity, can be successfully incorporated in the analysis (Ho *et al*., 2011). This has made it possible to calculate gas exchange properties of the fruit tissues required to compute internal gas

gradients. However, it has so far been assumed that fruit consists of homogeneous tissues characterized by average properties. Realizing that fruit tissue microstructure varies considerably across the fruit (Herremans *et al*., 2015a,b; Janssen *et al*., 2020a; Wang *et al*., 2020), it is hypothesized that heterogeneity in the tissue microstructure leads to heterogeneity in gas diffusion properties and, thus, gas concentration distribution in intact fruit that may affect the optimal settings in CA and DCA storage. To verify this hypothesis, it will be necessary to calculate the heterogeneity of the tissue microstructure and gas transport properties, and then incorporate this heterogeneity into the models to predict internal gas level.

This PhD will have a final application focus on pome fruit, as they are commercially highly relevant horticultural products in Belgium and in many other countries around the world, while storage of pome fruit is mainly under (D)CA. For the sake of demonstrating the genericity of the developed methods to a wider range of products, as well as for expanding the validity range of the models, also other products (eggplant and turnip) will be also considered.

1.2 Objectives and outline of the thesis

The overall objective of this PhD is to quantify the heterogeneity in tissue microstructure of fruit and vegetables and its effect on internal gas concentrations in (D)CA storage conditions. To this end, a novel quantitative imaging approach based on X-ray computed tomography (CT) is developed, verified and applied to map the porosity of fruit and vegetables. Regression models are estimated to compute gas diffusivity maps from the porosity and, for the first time, heterogeneous gas exchange models are applied to predict the internal gas concentrations during ultra-low oxygen storage under DCA conditions and interpreted in relation to the development of internal disorders in pear fruit.

The outline of this dissertation is as follows:

In Chapter 2, the state of the art in anatomical, physiological and technical aspects of fruit in relation to CA and DCA storage of fruit is reviewed.

In the third chapter, the development of a novel quantitative X-ray CT method to predict and map non-destructively the heterogeneous porosity of fruit and vegetables is discussed. Thereto, a regression model between grayscale values of the CT image of whole fruit and tissue porosity is developed for different products covering a wide range of porosity and internal structures, namely pear, apple, eggplant and turnip. Eggplant has higher porosity than apple, while that of turnip is between apple and pear. The developed model is used to transform CT images of intact fruit and vegetables into 3D porosity maps of the products.

In Chapter 4, a methodology to translate a 3D total porosity map into an effective O_2 diffusivity map is presented. Thereto, a regression model is developed to predict the effective O_2 diffusivity from the porous structure characteristics of the tissues of the different products considered in Chapter 3. The effective diffusivity is calculated from high resolution micro-CT images using previously developed models (Ho *et al.,* 2011). To establish the regression models, in addition to total porosity, open porosity and pore tortuosity are also considered. Diffusivity values predicted by the regression models are compared against computed values for independent tissue samples.

In Chapter 5, the developed techniques for porosity and diffusivity mapping are implemented to enable more accurate computations of the internal gas gradients in 'Conference' pear during storage under DCA conditions compared to previously published models. A procedure is developed to use the diffusivity maps in a respiration-diffusion model of pear fruit solved with the finite element method. The simulation results obtained with the heterogeneous model are compared to those computed using a single homogeneous effective O_2 diffusivity. Storage experiments are conducted in controlled conditions, and the extent of internal disorders is assessed in different individual pear fruit. From the

results of the model, the distribution of the respiratory quotient inside the fruit is computed and interpreted with respect to the occurrence of internal disorders.

Finally, based on the results of the research chapters, general conclusions and future perspectives are formulated in Chapter 6.

Chapter 2

Literature review

2.1 Introduction

Respiration of fruit and vegetables continuously occurs throughout the postharvest period to convert sugar reserves into energy in the form of adenosine triphosphate (ATP) (Kader and Saltveit, 2002). The energy is essentially required for regulation and maintenance processes of the cell and membranes (Kader and Saltveit, 2002; Gibbs and Greenway, 2003; Huang *et al*., 2005). At the same time, intermediates in the respiration process are the source of important flavor components, because they are the starting point for the biosynthesis of many volatiles, while the consumption of substrates such as sugars leads to quality loss. High respiration of newly harvested products may lead to rapid ripening and quality loss, thereby shortening storage and shelf life of the products. Respiration can be mainly reduced by lowering the temperature and oxygen (O_2) concentration in the storage room (Wills and Golding, 2016), while scrubbing the produced carbon dioxide (CO_2) to control its level to maintain an optimal value (Kader, 1989; Franck *et al*., 2007). This is typically applied in so-called controlled atmosphere (CA) storage systems. However, if O_2 concentration is too low, local anoxic conditions inside the fruit may occur, leading to oxidative stress and shifting the respiration to the energetically less efficient fermentation pathway (Franck *et al*., 2007). Volatiles produced by fermentation (ethanol, acetaldehyde, and ethyl acetate) may cause off-flavors (Ke and Kader, 1990; Ke *et al*., 1991) while the available energy is then insufficient for normal cell maintenance (Franck *et al*., 2007), eventually leading to physiological storage disorders in pear fruit, such as browning and core breakdown.

Respiration involves oxygen supply and carbon dioxide release from and to the storage headspace, respectively, through the heterogeneous tissue of the fruit or vegetable. Hence, the ability of tissues of fruit or vegetable organs to exchange

the respiratory gasses has become of interest as gas gradients inside the products were shown to exist (Rajapakse *et al.*, 1990; Perez and Beaudry, 1998; Zhang and Bunn, 2000; Ho *et al.*, 2011, 2013b, 2016) and affect the sensitivity of products to develop storage disorders (Ho *et al*., 2016). As *in-situ* measurements of gas concentrations and exchange rates inside fruit or vegetable organs are difficult, a modeling approach has been proposed (Mannapperuma *et al*., 1991; Lammertyn *et al*., 2003a; Ho *et al*., 2006b, 2011).

In this literature review, the relevant anatomical, structural and metabolic properties of fruit and vegetables are first discussed for understanding, modeling and optimizing CA storage conditions. Second, a more elaborate explanation is given of CA storage and storage disorders. Third, the state of the art of modeling of gas exchange in fruit is discussed. Finally, the method of X-ray computed tomography is introduced and how it can be used to visualize and quantify microstructure and shape properties that can be used in the models. Open questions are identified in the conclusions, which are the basis for the research in this PhD that is reported in the next chapters.

2.2 Fruit and vegetables

2.2.1 Anatomy of selected fruit and vegetables

The anatomy of fruit and vegetables can be defined as the layout of the different tissue types of the plant organ and how they are established during growth. We will focus here on the anatomy of pome fruit, eggplant and turnip as they will be used in the reminder of this dissertation to test various methods. According to the origin of the formation, fruit can be grouped as true fruit and false fruit. True fruit develop from the ovary of flowers, and the floral parts are just withered remains (Choudhary and Mehta, 2010). The ovary generally forms tissue layers of the fruit that are named the pericarp. From the outer to the inner part of the fruit organ, the pericarp is constructed by three layers, namely exocarp, mesocarp and endocarp (Choudhary and Mehta, 2010; Dardick and Callahan, 2014). False

or accessory fruit grow from the top of the flower stalk rather than from the ovary (Choudhary and Mehta, 2010).

Pome fruit like apple (*Malus x domestica*) and pear (*Pyrus communis* L.) are classified as false fruit. The hypanthium, a flower part where sepals, petals, and stamens are all fused to the ovary, evolves into most of the fleshy part of pear and apple fruit (Ireland *et al*., 2013), as illustrated in Figure 2.1.

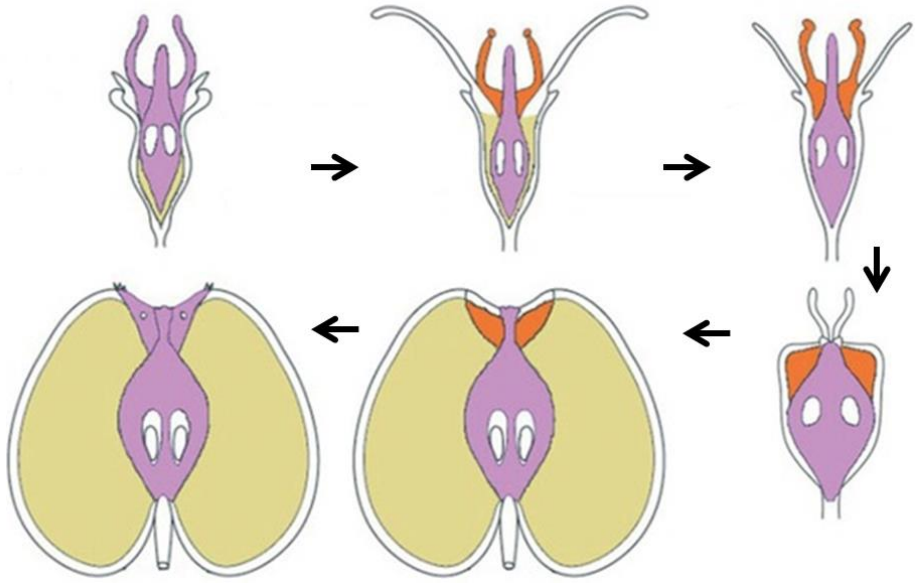

Figure 2.1. Illustration of flower-to-apple development. Yellow, purple and orange colors represent hypanthium, carpel-derived tissue and stamen-related tissue, respectively. The image is modified from Ireland *et al*. (2013).

At a mature stage, the skin directly covers the hypanthium of pome fruit. It consists of cuticle, epidermal and hypodermal cells (Wang *et al*., 2020). The cuticle protects the fruit from water loss and pathogen infection (Veraverbeke *et al*., 2003; Martin and Rose, 2013; Cohen *et al*., 2017). Below the hypanthium, the three tissue layers of the pericarp are located. The exocarp or also called epicarp links the hypanthium with the mesocarp, while the endocarp directly surrounds the seed lobes and seeds. The parenchyma, i.e., the fleshy tissue, of the hypanthium is often referred to as the (outer) cortex, while the parenchyma of the mesocarp as the inner cortex, or further denoted core region (Figure 2.2).

Spread out in the cortex tissue area are the vascular bundles that are responsible for delivering water and sugar to support fruit growth (Herremans *et al*., 2015b).

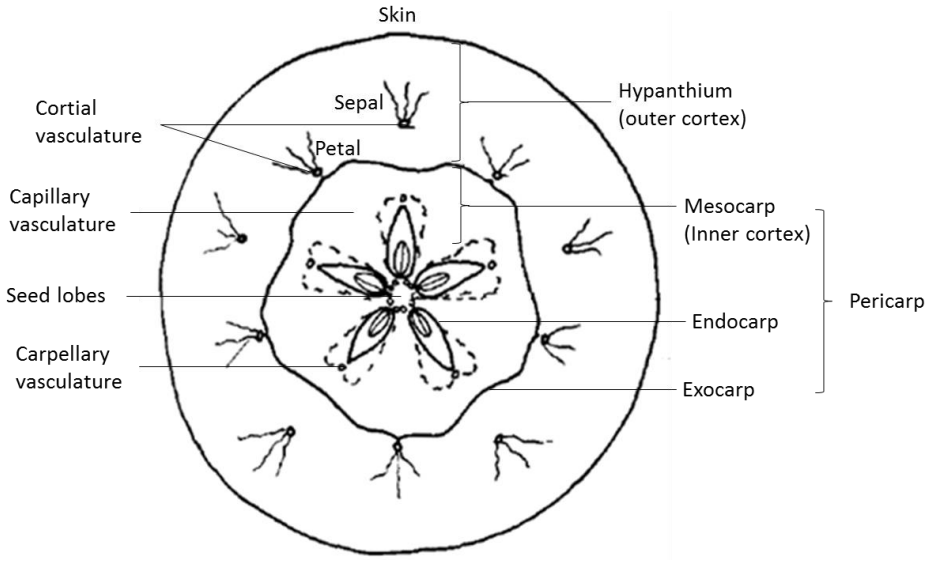

Figure 2.2. A Cross-section sketch of an apple showing outlines of different tissue areas and vascular system. The image is adapted from Macdaniels (1940).

Edible vegetable such as eggplant (*Solanum melongena* L.) is botanically classified as a true fruit (Choudhary and Mehta, 2010). Eggplant consists of multi-chamber berries with different shapes that vary from spherical, through oval, ovoid, to elongated and spiral, depending on the cultivar (Kowalska, 2008). The outermost tissue of eggplant is the epicarp which consists of the epidermis and 4 to 5 layers of rounded cells (Puig *et al*., 2012). The eggplant surface is covered by a uniform and non-porous waxy layer while the rest of the fleshy part of an eggplant is endocarp providing the spongy texture to the eggplant due to its large fraction of intercellular air space (Puig *et al*., 2012).

Turnip (*Brassica rapa* subsp. *rapa*) is an edible underground plant organ, which is typically categorized as a root vegetable. Turnip tubers consist of a hypocotyl and main root forming a fleshy organ through secondary growth by a vascular cambium (Zhang *et al*., 2014).

2.2.2 Microstructure

Fruit has anatomical features from the nanoscale to the macroscale (Mebatsion *et al*., 2008; Ho et al., 2013a). Ho *et al*. (2013a) mentioned that at the microscale level (10^{-6} – 10^{-3} m) cells and intercellular spaces of the fruit tissue can be differentiated. The microstructure can thus be defined as the architecture or layout of cells and intercellular spaces (pores) in tissue (Aguilera *et al*., 2000), distinguishing 3D shape and size characteristics of individual cells and pores and how they are interconnected, as described in Figure 2.3. Further, a single cell consists of smaller features such as the cell wall and plastids that were classified by Ho *et al*. (2013a) as mesoscale (10^{-7} – 10^{-6} m) objects. The microstructural elements participate in transport properties and physical behavior (Aguilera, 2005). Tissues of fruit and vegetables can be considered porous materials, as they may consist of up to 30 % of air spaces that exist in-between the cells and that may have developed from cell separation (schizogen) or cell death (lysigen) during growth of the organs. Of fruit and vegetables, most information of tissue microstructure is available for apple and pear, as they have been extensively explored for more than a decade now using X-ray computed tomography, see section 2.4 (Mendoza *et al*., 2007; Verboven *et al*., 2008; Herremans *et al*., 2015a,b; Janssen *et al*., 2020a; Wang *et al*., 2020; Chigwaya *et al*., 2021b). It has been shown that sizes, shapes, orientations and interface areas of cells and pores vary considerably between and within tissues of pome fruits. For eggplant and turnip, little information of their tissue microstructural features is available in the literatures, in addition to their tissue porosity.

In the cortex tissue, 'Jonagold' apple generally consists of larger parenchyma cells than that of 'Conference' pear (Verboven *et al*., 2008; Herremans *et al*., 2015a). The mean cell size described by their equivalent spherical diameter is 210 µm and 159 µm, respectively. Apple cells have distorted shapes while pear cells have a more round shape (Verboven *et al*., 2008). The cortex tissue of pear has air spaces that show triangular, rectangular and few polygonal cross sections between 2 or 3 cells (Verboven *et al*., 2008), typical for schizogenous formation

(Raven, 1996). Meanwhile, void spaces in apple tissue show large polygonal concave cross sections with similar sizes as those of the cells (Verboven *et al*., 2008), indicating a lysigenous origin (Raven, 1996).

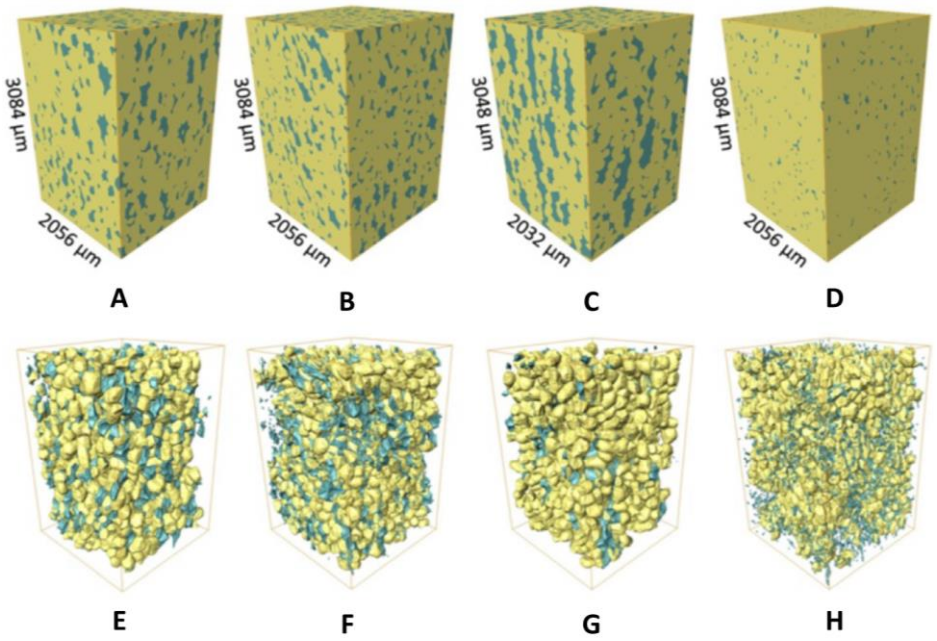

Figure 2.3. Microstructure model of (A) 'Braeburn'. (B) 'Kanzi', (C) 'Jonagold' apple and (D) 'Conference' pear cortex tissues. (E), (F),(G), and (H) represent isolated cells (yellow) and pore spaces (blue) of the tissue above them (Herremans *et al*., 2015a).

The pore spaces in 'Jonagold' apple are larger than those in 'Conference' pear (Verboven *et al*., 2008; Herremans *et al*., 2015a), as shown in Figure 2.3C, D and Figure 2.4. Among pome fruits, the small pore channels of the pear, however, continuously extend over the cells while the larger air pathways of the apple form irregular and more disconnected channels (Verboven *et al*., 2008; Herremans *et al*., 2015a). This indicates a higher pore connectivity in 'Conference' pear than in 'Jonagold' apple. Stone cells (branchysclereids) of the pear tissue, however, cause local discontinuities of the pore network (Verboven *et al*., 2008) (Figure 2.4B). Branchysclereids are small cells promoted by lignin synthesis during pear development (Yan *et al*., 2014). Finally, the proportion of

the cell-to-void area is much different between apple (41.7 %) and pear (21.8 %) (Herremans *et al*., 2015a). This value indicates the area of the cell surface that is the interface between cell and intercellular spaces. In addition, the microstructure of the pore space may be anisotropic. Apple pores in 'Jonagold' structurally orient along the radial axis while pear pores form a more isotropic network in between parenchyma cells (Verboven *et al*., 2008).

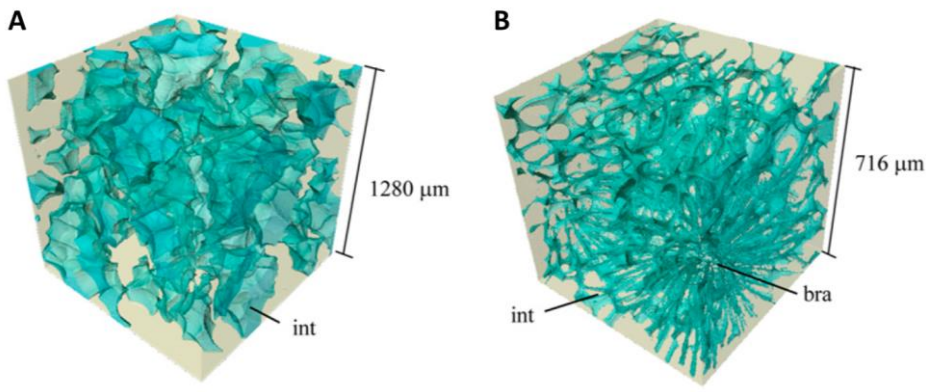

Figure 2.4. 3D pore network of (A) 'Jonagold' apple and (B) 'Conference' pear tissues imaged at high resolution (Verboven *et al*., 2008). The pointed elements are the intercellular spaces (int) and the branchysclereids (bra). The vertical axis is oriented along the radial direction of the pore network in the fruit.

Skin tissue consists of cuticle, epidermis and hypodermis. In the hypodermis layer, pear and apple are composed of smaller and more densely arranged cells, causing a smaller pore fraction in both fruit, and less connected pore structure for pear (Verboven *et al*., 2008). The stone cells are also found abundant below the epidermis of pear, interrupting many radial void networks. In apple, four layers of tightly packed collenchyma cells can be found (Verboven *et al*., 2008). Variability of the cell features was also found below the surface among apple cultivars (Wang *et al*., 2020).

During fruit development, the apple tissue microstructure in different positions changes considerably, marked by the increasing size of the cells and pore spaces, as well as by increasing porosity (Herremans *et al*., 2015b). So far, microstructure changes in 'Conference' pear have not been explored. The tissue

microstructure also undergoes changes due to the development of physiological browning disorders during storage. Tissues typically become denser (due to cell damage and cell liquid leakage into pores), then less dense again because of air space formation due to diffusion of the intercellular liquid towards the fruit boundary and into the storage atmosphere that leads to so called cavities (Lammertyn *et al*., 2003c,d; Chigwaya *et al*., 2021b).

Physical features of pore networks have crucial consequences to respiratory gas transport and, therefore, have become subject of study of tissue microstructure in relation to unraveling the respiration metabolism. These features are fundamentally characterized by porosity and pore connectivity or tortuosity that determines effective transport properties such as diffusivity and permeability (Herremans *et al*., 2015a). Typically, from the fruit surface inward, tissue porosity is small in the skin due to the dense packing of epidermal and hypodermal cells (Wang *et al*., 2020), increases to a maximum in the cortex tissue and decreases again at the core region (Dražeta *et al*., 2004.; Herremans *et al*., 2013; Janssen *et al*., 2020a). For pear, less detailed information is available. So far, it is known that the porosity of skin and cortex tissues are different, while the porosity of pear is considerably lower than that of apple (Verboven *et al*., 2008; Ho *et al*., 2010a; Herremans *et al*., 2015a). Table 2.1 summarizes the porosity values (%) that have been reported for different fruit and vegetables.

Table 2.1. Porosity (%) of different fruit and vegetable.

Products	Porosity (%)	Remarks	Methods
'Jonagold' apple	25.4 ± 2.60 (1)	mean ± SD of 4 cortex tissues	X-ray CT
'Kanzi' apple	12.1 ± 3.00 (1)		
'Braeburn' apple	18.4 ± 4.40 (1)		
'Conference' pear	5.70 ± 1.40 (1)		
'Follere' pear	7.60 ± 0.50 (2)	mean ± SD of 8 cortex tissues	X-ray CT
'Chili' pear	1.70 ± 0.17 (3)	mean ± SD	X-ray CT
'Carabao' manggo	11.7 ± 1.7 (4)	mean ± SD of 4 outer mesocarp	X-ray CT
'Fuyu' persimmon	4.00 – 69.0 (5)	range of different tissue areas	X-ray CT
Eggplant	59.6 ± 0.50 (6)	mean ± SE	Pycnometer
Zucchini	18.0 ± 2.00 (6)	mean ± SE	Pycnometer
Carrot	0.30 ± 0.80 (6)	mean ± SE	Pycnometer
Beetroot	6.00 ± 200 (6)	mean ± SE	Pycnometer

(1) Herremans *et al*. (2015a), (2) Muziri *et al*. (2016), (3) Duan *et al*. (2020), (4) Cantre *et al*. (2014), (5) Tanaka *et al*. (2018), (6) Gras *et al*. (2002).

Because respiratory gasses diffuse easily through the intercellular air space (Ho *et al*., 2011), tissues with smaller, less connected and more tortuous pore pathways will restrict the transport of gasses more. Pore connectivity of the tissue can be described by the measures open or closed porosity relative to the overall or total porosity. The total porosity counts the whole pore fraction of the tissue (Janssen *et al*., 2020b). The open and closed porosities only take into account the connected and unconnected pores of the total tissue volume, respectively, are typically smaller than the total porosity. However, few reports can be found on the open or closed porosity in fruit and vegetable tissues. Contrary to oxygen, the features of the pore microstructure most likely have less effect on carbon dioxide diffusion as it also diffuses through the liquid phase of the cells due to

its high solubility in water (Ho *et al*., 2011). To summarize, in addition to porosity topological cell features also play a role in respiratory gas diffusion.

Another important parameter of the pore network structure is tortuosity. As shown in Figure 2.5, tortuosity is defined as the ratio of tortuous pore length (red line, x) to the straight-line length (L) of the medium (Ghanbarian *et al*., 2013; Tjaden *et al*. 2016; Al-Raoush and Madhoun, 2017). It describes the fact that respiratory gasses diffuse through the meandering pore channels of the tissue that are longer than the actual tissue length. Higher tortuosity thus reduces the ability of tissue to transport gasses across them (Alean *et al*., 2018; Sun *et al*., 2019). Tortuosity generally declines with increasing porosity (Alean *et al*., 2018). So far, little information of tortuosity in plant tissues is found in literature.

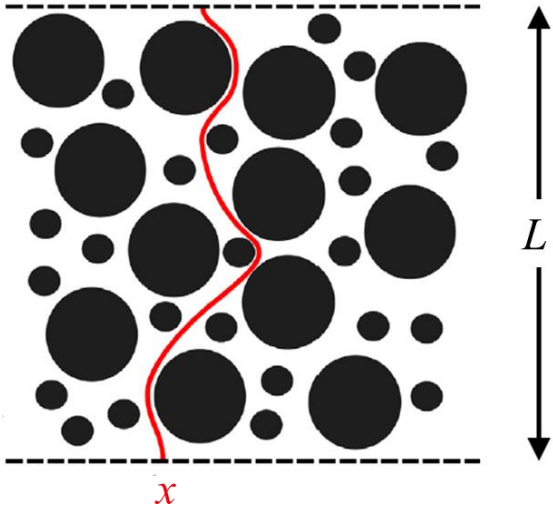

Figure 2.5. Illustration of pore tortuosity modified from Tjaden *et al*. (2016). The red line (x) is the actual pore path at the mass transport direction. It is longer than the medium length (L).

2.2.3 Respiration

While fresh products continuously respire after harvest and undergo rapid deterioration, the control of the respiration process is the scientific basis for maintaining the quality of the products for a long term. With sufficient oxygen (O_2) supply, respiration oxidizes complex substrates to carbon dioxide (CO_2),

water (H_2O) and energy (van Dongen *et al*., 2011). This process is carried out in three metabolic processes: the glycolysis and the tricarboxylic acid (TCA) cycle, in which CO_2 are produced, and oxidative phosphorylation, in which O_2 is consumed. The energy produced by the respiration activities is required by living cells for maintenance and growth (Gibbs and Greenway, 2003; Millar *et al*., 2011). Temperature in the cool room is the most influential aspect to control the respiration rate, followed by the O_2 and CO_2 partial pressures (Hertog *et al*., 1998; Lammertyn *et al*., 2001; Boeckx *et al*., 2019). The effect of temperature on O_2 consumption is given by the activation energy in a typical Arrhenius relationship. At a given temperature, the respiration rate, quantified by the O_2 consumption and total CO_2 production, declines as the O_2 concentration is decreased (Figure 2.6) (Boeckx *et al*., 2019). Combination of these practices helps to extend the storage period of many fruit and vegetables.

When the O_2 concentration in the storage atmosphere drops excessively, partial deficiency (hypoxia) or absolute absence (anoxia) of O_2 in the plant tissue may result (Figure 2.6). Such a condition causes the metabolic activity of the cells to change from aerobic respiration to fermentation. Depending on temperature, the increase and decrease of oxygen clearly speed up respiration and fermentation, respectively (Hertog *et al*., 1998). Anaerobic compensation point (ACP) is defined as the oxygen concentration at which the CO_2 production rate is minimal. Below the ACP, fermentation dominates aerobic respiration and thus increases the CO_2 production rate, provoking the development of off-flavors and storage disorders (Boersig *et al*., 1988; Yearsley *et al*., 1996; Geigenberger, 2003; Franck *et al*., 2007). Above the ACP, CO_2 production rate increases with respiration rate as a function of the increasing O_2 concentration.

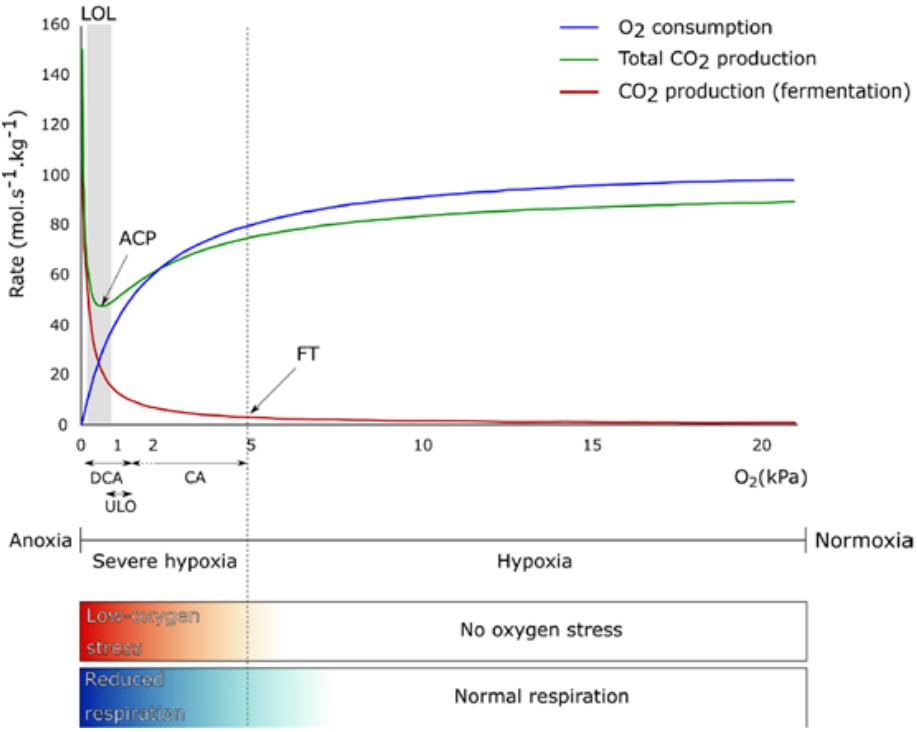

Figure 2.6. Effect of O_2 concentration on O_2 consumption (blue line), total CO_2 production (green line), and CO_2 production from fermentation (red line) by apple. The anaerobic compensation point (ACP), fermentation threshold (FT), and lower O_2 limit (LOL) are indicated. The range of O_2 partial pressure applied in CA, ULO and DCA storage is plotted. The range for no O_2 stress is where O_2 levels are sufficient for a normal respiratory metabolism. Low-O_2 stress occurs where O_2 levels are limited (severe hypoxia) or completely absent (anoxia) in the storage headspace and the fruit needs to adapt their respiratory metabolism. The color gradient explains the gradual transition between no O_2 stress and low-O_2 stress and between normal respiration and reduced respiration (Boeckx *et al*., 2019).

The activation of the fermentation pathway is initiated when an anaerobic event occurs (Tadege, 1999; Bailey-Serres and Voesenek, 2008). Fermentation leads to a reduced supply of ATP for energy-demanding activities (Boeckx *et al*., 2019). In the fermentation pathway, the energy yield is only 2 moles ATP per mole glucose compared to 36 moles by aerobic respiration (Franck *et al*., 2007). To compensate for insufficient energy production, the glycolytic flux in plants naturally increases to generate more energy by transforming glucose to pyruvate,

well known as the Pasteur's effect (Barker *et al*., 1964). Fruit hydrolyzes starch to provide sufficient sucrose for the high glycolytic flux. As the flux increases, accumulation of pyruvate occurs due to stalled transport of pyruvate into the TCA cycle. Transformation of pyruvate to ethanol and CO_2 can take place throughout the fermentation process, simultaneously stabilizing the redox balance in the cell by the formation of NAD^+. Pyruvate is reduced to lactic acid by lactate dehydrogenase (LDH) in the cytoplasm (Tadege, 1999). The lactic acid that accumulates may result in cytoplasmic acidosis, causing cell damage. Acidification of the cytoplasm inactivates LDH and activates pyruvate decarboxylase (PDC) (Roberts *et al*., 1984; Boeckx *et al*., 2019), which decarboxylates pyruvate and forms acetaldehyde, which in turn is converted into ethanol by alcohol dehydrogenase (ADH) and to ethyl acetate by the enzyme alcohol acyl transferase. The resulting fermentation metabolites, ethanol, acetaldehyde, and ethyl acetate, cause off-flavor development in the fruit (Tadege, 1999).

For a short time, the cells may naturally adapt to the hypoxic or anoxic condition by allowing ATP regeneration (Drew, 1997; Toro and Pinto, 2015). However, for extended low oxygen periods, the low energy status resulting from the low-O_2 stresses (Drew, 1997; Franck *et al*., 2007) can be a paradox of the benefit of lowered O_2 concentration in the storage atmosphere. Gibbs and Greenway. (2003) revealed that attention to low O_2 concentration in the cells is crucial, even under external normoxia conditions, because of the high O_2 transport resistance of the tissue, highlighting the importance of the tissue microstructure discussed in the previous section.

2.3 Storage of fruit and vegetables

2.3.1 Controlled atmosphere storage

The essential role of the respiration control in extending storage life of fruit and vegetables has driven the development of controlled atmosphere (CA) storage over the years. In CA, the fruit or vegetable is exposed to a storage environment

with reduced temperature, low oxygen and modified carbon dioxide partial pressure. In regular CA, the O_2 gas concentration is kept at a safe and steady level above the ACP throughout the storage period, as indicated in Figure 2.6. The ACP is different for different cultivars. For example, it was found to be 0.7 – 1.8 kPa O_2 for apple (Gran and Beaudry, 1993; Yearsley *et al*., 1997), 1.6 – 1.7 kPa for pear (Boersig *et al*., 1988), and 1.44 – 1.81 kPa O_2 for avocado (Valle-Guadarrama *et al*., 2004). In ultra-low oxygen (ULO) storage, the O_2 concentration is further reduced to be closer to or at the ACP to gain the optimal benefit of the CA (Thewes *et al*., 2015; Mditshwa *et al*., 2018). However, since the ACP of the fruit varies among the cultivars or batches, the use of static gas composition is suboptimal and brings the risk of inducing storage disorders (Bessemans *et al*., 2016). CA is sometimes combined with a pre-cooling treatment under atmospheric conditions, known as delayed-CA. The fruit is then initially stored at low temperature for some days or weeks before being exposed to the modified gas compositions (Lammertyn *et al*., 2003b). This method has been found to decrease the sensitivity of pome fruit to internal browning (Franck *et al*., 2007).

A more advanced version of CA storage is dynamic CA (DCA) that involves automatic control of the set gas compositions along the storage period based on the biological response produced by the stored fruit measured by a sensor (Thewes *et al*., 2020). Three typical sensor principles used in DCA are chlorophyll fluorescence (CF), ethanol production (ET) and respiratory quotient (RQ) (Mditshwa *et al*., 2018). However, in ET- and CF-based DCA, a detection bias of the low O_2 stress may occur due to the high solubility of ethanol in aqueous environments (Knee and Hatfield, 1976; Gupta *et al*., 2000) and non-O_2 stress triggers of chlorophyll fluorescence (Ögren, 1990; Wright *et al*., 2010), respectively. Recently, a new DCA concept has been introduced based on carbon dioxide production (DCA-CDP) (Thewes *et al*., 2020). The increase of the CO_2 production rate when the O_2 concentration is continuously decreased makes it possible to estimate the low oxygen limit. This method keeps the induction of anaerobic metabolites at save levels with fewer storage disorders.

In the MeBioS Postharvest Group, a method was developed to measure the O_2 stress signal during DCA storage based on RQ (Bessemans *et al*., 2020, 2016). The RQ is the ratio of CO_2 production rate to the oxygen consumption rate and ranges from 0.7 to 1.3 in aerobic conditions (Kader and Saltveit, 2002). As the O_2 level further decreases and CO_2 levels increase due to fermentation, the RQ exponentially increases (Gran and Beaudry, 1993; Yearsley *et al*., 1997). RQ-DCA has been used successfully to automatically control the O_2 and CO_2 levels and detect low O_2 stress throughout the storage period (Bessemans *et al*., 2016). Compared to regular CA, RQ-DCA storage was found to minimize the incidence of storage disorder such as superficial scald on 'Granny Smith' apple (Bessemans *et al*., 2016).

However, Bessemans *et al*. (2020) found a higher internal RQ in the pear tissue than the external RQ in the storage headspace. This was most likely caused by the gas diffusion resistance of the pear skin and tissue. This implies that the oxygen stress may have already occurred inside the fruit while the headspace RQ is still below the threshold. Since pear tissue is known to be heterogeneous, prediction of the internal RQ level taking into account the variability of the tissue structure may help to more precisely identify the internal RQ which is the O_2-stress signal needed for optimal DCA storage. For regular CA, the evolution of the internal RQ level is also useful for determination of the safe O_2 level.

2.3.2 Internal browning disorder

Besides the effects of pre-harvest factors (orchard, altitude, temperature, position on the tree), internal browning is a typical consequence of excessively low O_2 and high CO_2 concentrations in the storage headspace (Lammertyn *et al*., 2000; Franck *et al*., 2007). As the fruit tissue and skin cause gas diffusion barriers, the internal O_2 and CO_2 can be lower and higher, respectively, than the external ones (Lammertyn *et al*., 2003b; Franck *et al*., 2007; Ho *et al*., 2011). Areas of browning disorder do not develop in size, but the affected tissue becomes more severe, and cavities are eventually formed (Veltman, 2002; Lammertyn *et al*., 2003 c,d).

As explained above, fermentation at hypoxic or anoxic conditions inside (Figure 2.6) the fruit may cause cell membrane damage and trigger enzymatic oxidation of phenolic compounds to o-quinones by polyphenoloxidase (PPO). The highly reactive o-quinones form brown colored pigmentation on the fruit tissue (Veltman *et al*., 2003; Franck *et al*., 2007). Cytoplasm of impaired cells fills up the internal air space of the tissue and eventually diffuses to the fruit surface where it evaporates, creating cavities in the affected fruit tissue (Lammertyn *et al*., 2003c,d; Franck *et al*., 2007). The liquid-filled intercellular spaces increase gas diffusion resistance into and out of the fruit. As a result, the O_2 concentration may be further lowered while the CO_2 concentration increases inside the fruit (Franck *et al*., 2007), further triggering the breakdown of the affected tissue. Experimental evidence has shown that low O_2 levels combined with too high CO_2 levels increased the incidence of browning in pears (Veltman, 2002; Lammertyn *et al*., 2003a,b). Veltman *et al*. (2003) found that browning incidence in pear fruit occured faster at 5 % CO_2 than at 0 % CO_2 (Veltman *et al*., 2003). The affected tissue is typically observed more abundantly in the center of the fruit, while tissue closer to the skin is less affected (Lammertyn *et al*., 2003c,d). Denser tissue regions and, inherently, lower effective diffusivity most likely contribute to a higher susceptibility of internal browning at the fruit center.

Lammertyn *et al*. (2000) found that late-harvested pears were more sensitive to browning disorder than early-harvest pears. This is either due to a larger size of late harvested pear or increased respiration rate (Franck *et al*., 2007). Pears initially treated with pre-cooling for 21 d at -1 ^{o}C exhibited less internal browning during CA storage than fruit immediately stored under CA (Verlinden *et al*., 2002). This protocol gives very good results for pear fruit picked at commercial and late harvest dates (Franck *et al*., 2007). In this way, the respiration rate has been reduced considerably by the cooling process before the storage atmosphere is changed. In terms of size, larger pears developed more brown tissue and cavity than smaller pears (Lammertyn *et al*., 2000). Similarly, larger apples showed a higher sensitivity to internal browning, indicated by a higher Michaelis-Menten constant K_{m,O_2} of intact fruit (Ho *et al*., 2011), a

measure for respiration saturation with respect to oxygen level. The K_{m,O_2} value highly depends on the fruit size as the diffusion resistance increases with size.

2.4 Modeling of respiratory gas exchange

As explained above, the O_2 and CO_2 partial pressures that are applied in CA storage depend on species, cultivar, origin, season, and harvest date. This requires a large experimental effort both in terms of human capacity as well as storage resources. Alternatively, mathematical models can be used to quantify the relevant processes inside the product and, further, determine critical external and internal factors affecting storage. These models could also help in optimizing storage methods by determining conditions which avoid storage disorders while maximizing quality retention. Attempts to develop a model of respiration and gas diffusion in fruit and vegetables started decades ago. Lee *et al*. (1991) introduced Michaelis-Menten kinetics to describe respiration of a whole fruit. Peppelenbos and Leven. (1996a) and Hertog *et al*. (1998) modified the Michaelis-Menten model to incorporate different types of CO_2 inhibition. The extended models were implemented to express O_2 intake and CO_2 production rates as a function of O_2 and CO_2 partial pressures. These lumped models, while often used for optimizing modified atmosphere packaging, provide no direct insight in the internal O_2 and CO_2 concentrations.

2.4.1 Reaction-diffusion-permeation models for gas transport in pome fruit

Reaction-diffusion models incorporating the actual fruit geometry were developed by Lammertyn *et al*. (2003a,b) to predict profiles of O_2 and CO_2 concentrations in 'Conference' pear and their effect on the spatial development of internal physiological disorders. The model managed to describe the gas gradients caused by the diffusion resistance of the pear tissue. Thereto, effective diffusivity values of the tissues were measured with dedicated setups. The fact that the effective CO_2 diffusivity was found higher than the effective O_2 diffusivity (Lammertyn *et al*., 2001; Ho *et al*., 2006a) indicated that, in addition

to gas diffusion, respiratory gas transport is also stimulated by permeation as the result of the total pressure difference. Ho *et al*. (2006b) thereto integrated a permeation term into the respiration-diffusion model that consequently needed to take into account nitrogen (N_2) transport in addition to O_2 and CO_2 transport. The general equation for gas transport of component *i* (O_2, CO_2 or N_2) in the fruit tissue was then expressed as:

$$\alpha_i \frac{\partial C_{i,g}}{\partial t} + \nabla \cdot (\mathbf{u}\mathbf{C}_{i,g}) = \nabla \cdot D_{i,eff} \nabla C_{i,g} + R_i \qquad (2.1)$$

with

$$\alpha_i = \varepsilon + (1-\varepsilon) RTH_i = \frac{C_{i,tissue}}{C_{i,g}} \qquad (2.2)$$

with α_i the tissue gas capacity for component i, $C_{i,g}$ (mol m^{-3}) the concentration of gas i in the gas phase, t (s) the time, ∇ (m^{-1}) the gradient operator, $\mathbf{u}$ (m s^{-1}) the effective convection velocity vector, $D_{i,eff}$ (m^2 s^{-1}) the effective tissue diffusivity for gas i. R_i (mol m^{-3} s^{-1}) the tissue respiration rate, ε the (total) tissue porosity, R (Pa m^3 mol^{-1} K^{-1}) the universal gas constant, T (K) the temperature, H_i (mol m^{-3} Pa^{-1}) Henry's constant for gas i and $C_{i,tissue}$ (mol m^{-3}) the volume-averaged concentration of gas i. The model described by Equation 2.1 and 2.2 implies gas equilibrium in the tissue described by Henry's law of solubility with water as the liquid phase. Permeation caused by the pressure gradient was expressed by Darcy's law:

$$\mathbf{u} = -\frac{K}{\mu} \nabla P = -\frac{KRT}{\mu} \nabla \left(\sum C_{i,g} \right) \qquad (2.3)$$

with K (m^2) the permeation coefficient, P (Pa) the total gas pressure, and μ (Pa s) the gas viscosity. It was assumed that the relation of gas concentration and pressure follows the ideal gas law ($P = CRT$).

After the developed permeation-diffusion-reaction model was found appropriate for the simulation of gas transport in disk-shape geometries (Ho *et al*., 2006b), the model was applied to calculate internal gas gradients in intact pear (Ho *et al*, 2008). Measurement of the effective diffusivity, permeability and respiration kinetics parameters was performed on tissue samples that were excised from representative fruit. However, this approach did not allow to relate tissue microstructure to the parameter values. Moreover, practical issues such as flooding of intercellular spaces by the cell liquids during sample cutting caused artifacts in the measured properties. Therefore, a multiscale modeling strategy was developed (Ho *et al*., 2011). A multiscale model combines a continuum gas exchange model of the fruit with the parameters provided by smaller-scale models taking into account microscale features of representative volumes of the tissues (Ho *et al*., 2011; 2013a; Verboven *et al*., 2012).

In the multiscale modeling approach, the effective diffusivity is calculated using a transport model applied to a geometry that resolves the tissue microstructure. The so-called microscale model predicts mass transport of respiratory gasses in the intercellular space (pore), cell wall, cell membrane, and into the cytoplasm (Ho *et al*., 2009). Due to the fact that exact details of microscale heterogeneity play a significant role in gas transport, microscale models cover the limitations of the macroscale model explained above (Ho *et al*., 2013a). The microscale gas-exchange model developed by Ho *et al*. (2009) was initially solved using the finite element method applied to processed images of 2D cross sections of tissues. Later, it was extended to 3D to account for the highly tortuous microstructure of the tissues (Ho *et al*., 2011). Thereto, solvers using either the finite volume method or a pore network approach were implemented. The latter has the advantage of being more computationally efficient, making it more useful for large tissue geometries (Ho *et al*., 2014), while requiring more effort to construct the network topology.

At the interface between pores and cells, O_2 diffuses through the cell wall and membrane that are both assumed to be in the liquid phase (Ho *et al*., 2011). At that contact area, the gas and liquid concentrations of O_2 are equivalent according to Henry's law:

$$C_{i,l} = RTH_i C_{i,g} \tag{2.4}$$

where R (8.314 J mol^{-1} K^{-1}) is the universal gas constant, T (K) the temperature and H_i (mol m^{-3} kPa^{-1}) is Henry's constant for gas i. The indices l and g represent the cells (liquid) and pores (gas) phase. Interface flux, J_i (mol m^{-2} s^{-1}), was described as

$$J_i = P_{i,eff}\left(RTH_i C_{i,g} - C_{i,l}\right) \tag{2.5}$$

where $P_{i,eff}$ (m s^{-1}) is the effective permeability of membrane and cell wall that can be written as

$$P_{i,eff} = \frac{1}{\frac{L_w}{D_{i,w}} + \frac{L_m}{D_{i,m}}} \tag{2.6}$$

where $D_{i,w}$ and $D_{i,m}$ (m^2 s^{-1}) are the gas diffusivities of cell wall and cell membrane, respectively, while L_w and L_m are the thicknesses of those compartments.

Based on simulations with the microscale model local gradients in gas concentrations and fluxes through the tissues were simulated. These were used to compute the effective transport parameters of the tissue, using for example Fick's law diffusion (Ho *et al*., 2009; 2011). The models applied at the microscale were:

$$J_{i,total} = -D_{i,eff}\frac{\Delta C_i}{L} \tag{2.7}$$

with $J_{i,total}$ (mol m^{-2} s^{-1}), the total flux of gas i diffusing through the tissue (mol m^{-2} s), $D_{i,eff}$ (m^2 s^{-1}) the effective diffusivity of gas i, ΔC_i (mol m^{-3}) the given concentration difference of gas i, and L (m) the thickness of the tissue.

The computational results compared well to experimentally measured diffusivities carried out on disk-shape tissue samples of 'Jonagold' apple (Ho *et al*., 2011). For denser tissues like pear tissue, lower experimental diffusivities than the computed ones were likely due to cell leaking during the sample cutting (Ho *et al*., 2016). This was further verified by Ho *et al*. (2016) by doing the microscale model computation by assuming pores to be blocked. They found that the presence of cellular liquid in the pore space indeed reduced the effective gas diffusivity. Therefore, the microscale model-based method may reasonably be applied to determine effective gas diffusivity of fruit and vegetable tissues. Because of the heterogeneity of the tissues and the different microstructure of different tissues Ho *et al*. (2016) computed the gas diffusivity at different positions inside the fruit and characterized them statistically. Subsequently, they used a Monte Carlo method to assign a variable O_2 and CO_2 diffusivity to different places inside the cortex tissue and incorporated them into the existing gas exchange model to predict internal O_2 and CO_2 gradients in 'Conference' pear (Ho *et al*., 2016). The multiscale model was utilized to study the incidence of internal browning in 'Braeburn' apple (Herremans *et al*., 2014a), local ATP deficiency in apple during CA storage (Ho *et al*., 2013b), and the effect of biological variation in pear related to harvest date, temperature and fruit size (Ho *et al*., 2016).

A more advanced method has been recently developed. Two-phase effective O_2 diffusivity coefficients (cell and pore) computed over the microscale tissue from four tissue compartments (skin, high porosity cortex, low porosity cortex, and core) were used to establish a non-equilibrium respiratory gas exchange model (Janssen *et al*., 2020b). The results showed that the internal O_2 concentration gradient was affected by features of the local microstructures, more specifically the open porosity. Bessemans *et al*. (2020) developed lumped models of

respiratory gas exchange that largely relied on the skin resistance of the pear skin at the environment-intercellular space interface and the cell resistance at the intercellular space-cell interface. With this approach they found a difference in gas concentrations and respiratory quotient (RQ) between the headspace, intercellular spaces and cells.

Still, available approaches so far have not considered the spatial heterogeneity of tissue microstructure in intact fruit. As described earlier, the tissue microstructure varies across and between tissues, which would cause space-dependent effective properties across a fruit. It is reasonable to expect that this may lead to a more heterogeneous gas concentration profile than that predicted by the aforementioned gas transport models.

2.4.2 Models for effective transport parameters

Since the effective diffusivity of porous materials is microstructure dependent, theoretical and empirical models for effective gas diffusivity with respect to microstructural parameters of the porous medium have been proposed.

Ho *et al*. (2010b) and Herremans *et al*. (2015a) found that the effective O_2 diffusivity increases with tissue porosity. In porous media, the simplest approach is to define effective diffusivity as an exponential function of porosity, following Archie's law (Navarre-Sitchler *et al*., 2009; Peng *et al*., 2012; Gao *et al*., 2013):

$$D_{i,eff} = \varepsilon^n D_{i,g} \tag{2.8}$$

with ε (%) the porosity of the porous medium, n a fitting parameter that reflects the specific characteristic of the pore geometry, $D_{i,eff}$ ($m^2\ s^{-1}$) the effective gas diffusivity of the porous medium, and $D_{i,g}$ ($m^2\ s^{-1}$) the molecular diffusivity of the gas i. The exponent n should estimate from experimental data and varies across different porous media (Peng *et al*., 2012; Gao *et al*., 2013). Its value typically ranges from 1.3 to 3. The porosity (ε) in the model can also be either the total or open porosity depending on the pore structure (Navarre-Sitchler *et al*., 2009).

Other models for effective gas diffusivity with respect to the porosity of porous media have been reported in the literature (Neale and Nader, 1973; Tomadakis and Sotirchos, 1993; Mezedur et al., 2002). Those empirically developed by simplifying assumptions of complex micro-morphologies of porous media, however, did not predict the effective diffusivity well in the low porosity range (< 50 %) (Mu *et al*., 2007).

However, respiratory gasses diffuse not only through pore channels of the tissue, but also through cells which mostly consist of liquid water. Therefore, the model presented above is not sufficient to express the effective tissue diffusivity of oxygen and carbon dioxide. An extended model for effective diffusivity is required to include the two main phases in the plant tissue. To this end, structural properties of each phase need to be taken into account in order to set a proper mixing model (Silva *et al*., 2000). An expression for the effective gas diffusivity of fruit tissue was previously formulated by Ho *et al*. (2006b) as:

$$D_{i,eff} = \varepsilon D_{i,g} + (1-\varepsilon) D_{i,l} RTH_i \tag{2.9}$$

The first and second terms on the right side represent diffusion of gas i in the intercellular space and in the cells, respectively; ε is the tissue porosity; $D_{i,g}$ ($m^2 s^{-1}$) is the diffusivity of gas i in air; and $D_{i,l}$ ($m^2 s^{-1}$) is the diffusivity of gas i in liquid. However, this model is still limited by the fact that the pore space network is highly heterogeneous and tortuous, making the relationship between the effective diffusivity and the structural properties is not necessarily linear as proposed by the formula.

Analysis of the tissue geometry is, therefore, required to realistically determine the structural properties of each fraction of the tissue such as total porosity, pore connectivity and tortuosity. Connectivity of pores and cells is an important geometrical feature that can only be well described by the 3D tissue geometry (Ho *et al*., 2011). Pore connectivity can be described by the open porosity, which only considers the connected pores over the total tissue domain in the direction of diffusion.

As described earlier, the tortuous pore structure causes the effective diffusivity in more tortuous porous media to be lower than that in media with more straight channels, even if the porosity is similar (Garrouch *et al*., 2001). Therefore, in the fundamentals of porous media, tortuosity is a main geometric parameter defining the pore structure (Clennell, 1997; Ghanbarian *et al*., 2013). The simplest effective diffusivity model related to tortuosity and porosity is typically expressed as (Rashapov and Gostick, 2016):

$$D_{i,eff} = \frac{\varepsilon}{\tau} D_{i,g} \tag{2.10}$$

with τ the pore tortuosity. As shown in Figure 2.5, pore tortuosity is modeled as (Ghanbarian *et al*., 2013; Al-Raoush and Madhoun, 2017):

$$\tau = \frac{x}{L} \tag{2.11}$$

where x (m) is the actual length of the diffusion path and L (m) the straight length of the material.

The relationship between effective diffusivity and tortuosity were theoretically described by Currie (1960). The model was developed based on a simple porous geometry described as a volume element, or a block, with a tortuous pore channel that crosses between two opposite sides of the block. The mass rate through the channel described using Fick's first law was assumed to be the same as the rate in the block as a whole. The final formula was $D_{eff} = D_{i,g}\ \varepsilon / \tau^2$. However, due to the fact that a porous material generally has a complex structure, it was suggested to empirically adapt the ratio D_{eff} / D_g to structural parameters of the material for complex porous materials (Troeh and Jabro, 1982).

To incorporate the different phases and structural complexity of the fruit and vegetable tissues, new models for effective gas diffusivity should be explored that take into account microstructure.

2.5 Microstructure analysis and modeling

As respiratory gas transport is a structure-dependent process, the actual geometry of fruit or vegetable and its tissue is necessary as a model input to compute gas transport in a whole organ or a tissue. To this end, non-destructive tomographic imaging such as magnetic resonance imaging (MRI) and X-ray computed tomography (CT) are powerful techniques to realistically construct a 3D geometry of the fruit or vegetable. X-ray CT is, however, preferred in this case due to its ability to image both the detailed tissue microstructure of tissue samples at a high resolution and the structure of whole fruit at lower resolution (Herremans *et al*., 2014b).

2.5.1 X-ray computed tomography (CT)

X-ray CT scanning is based on the propagation of X-ray energy through the scanned sample. In general, X-ray CT scanning can be performed using two different types of sources (Salvo *et al*., 2003): a synchrotron and an X-ray tube. The former transmits X-ray beams which are nearly monochromatic (allowing dose optimization) and laminar (allowing a reduction in scattered radiation) (Bravin *et al*., 2013). The use of a synchrotron source enables a quantitative reconstruction without geometrical and beam hardening artifacts (Salvo *et al*., 2003). However, its accessibility is limited compared to X-ray tubes which generate a polychromatic and divergent beam (Salvo *et al*., 2003).

In principle, the X-rays propagating through the scanned material are partially absorbed and scattered, resulting in energy attenuation of the X-ray beam. Attenuation measurement is determined by catching the remaining X-rays by way of an X-ray detector (Figure 2.7).

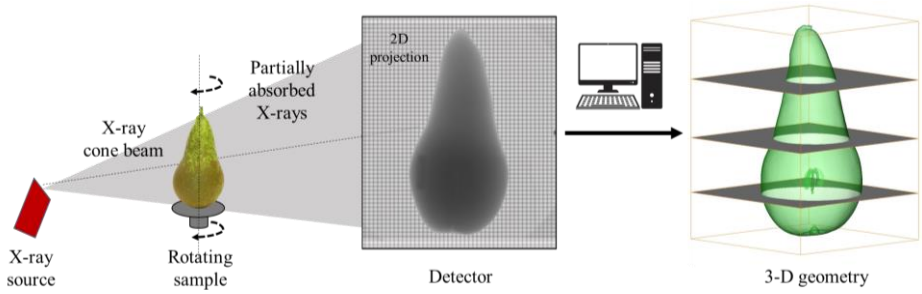

Figure 2.7. Illustration of the principle of X-ray CT applied to a 'Conference' pear. The source generates X-rays which traverse through the rotating sample. The absorbed X-ray energy is dependent on the local composition and density of the fruit and the traversing rays are captured on an X-ray sensitive detector resulting in a 2D projection image. To obtain a 3D image, multiple projection images obtained from different angles are combined to compute the tomogram, consisting of cross-sectional slices, that reflects the internal structure of the fruit.

For a monochromatic (monoenergetic) X-ray beam and a material of homogeneous density and atomic number this relationship is typically expressed by Lambert-Beer's law (Hsieh, 2009):

$$I = I_0 e^{-\int \mu_{E,S} dS} \tag{2.12}$$

where I and I_o represent the transmitted and incident X-ray intensities, $\mu_{E,S}$ is the energy- and location-dependent attenuation coefficient. For polychromatic X-ray beam, an energy spectrum of $\Omega(E)$ can be set into many bins based on their energies. The response of the material to the polychromatic X-ray flux is the integration of the response of all bins. When the attenuation coefficient $\mu_{E,S}$ as a function of the X-ray energy input is known, the relationship between the incident and the transmitted X-ray flux is written as (Hsieh, 2009):

$$I = I_0 \int \Omega(E) e^{-\int \mu_{E,S} dS} dE \tag{2.13}$$

where I and I_o represent the total transmitted and incident X-ray intensities, respectively.

The expected resolution can be set by moving the specimen and/or detector as the specimen has to be in the field of view (FOV) of the detector. Spatial resolution of image is a measure of ability to distinguish structures as separate and distinct from each other. It is typically related to voxel size, which is the smallest volume element of 3D image. The voxel is the 3D analog of a pixel. The X-ray source can be a fan beam, cone beam or parallel beam geometry, while the detector can be one-dimensional (1D) line detector (fan-beam) or two-dimensional (2D) CCD camera (cone beam) (Salvo *et al*., 2003).

High resolution X-ray CT systems, or typically called X-ray micro-CT, are different from medical CT scanners (De Chiffre *et al*., 2014). First, in the micro CT the scanned material rotates while the X-ray source and detector are stationary. Second, since the dose of radiation penetrating the material is typically not critical in micro CT, a greater intensity of radiation can be applied than those used in medical CT. Third, scanning parameters are typically different from medical CT as the resolution and accuracy requirements are different. Finally, most X-ray micro-CT scanners use a cone beam and a flat panel (2D) detector as it results in a hundredfold reduction in scanning time (multiple slices taken in one rotation) and good quality images.

The X-ray CT scanning process produces a two-dimensional (2D) radiographic image at each angular position of the rotating sample (Kruth *et al*., 2011). To extract physical parameters of the scanned sample, the next steps are reconstruction and image processing.

2.5.2 CT image reconstruction

The multiple 2D projection images are reconstructed into a 3D image of the attenuation coefficient using mathematical principles to sequentially generate cross-sectional image slices of the scanned sample. Reconstruction of the projection images is commonly solved by filtered-backprojection based on the linear integral transformation, a model originally developed by J. Radon in 1917 (Kruth *et al*., 2011). In principle, the backprojection method distributes the

projection intensity of the object among all pixels on the X-ray path (Hsieh, 2009). Figure 2.8 shows a simple illustration where the object of interest is a cylinder with significant absorption.

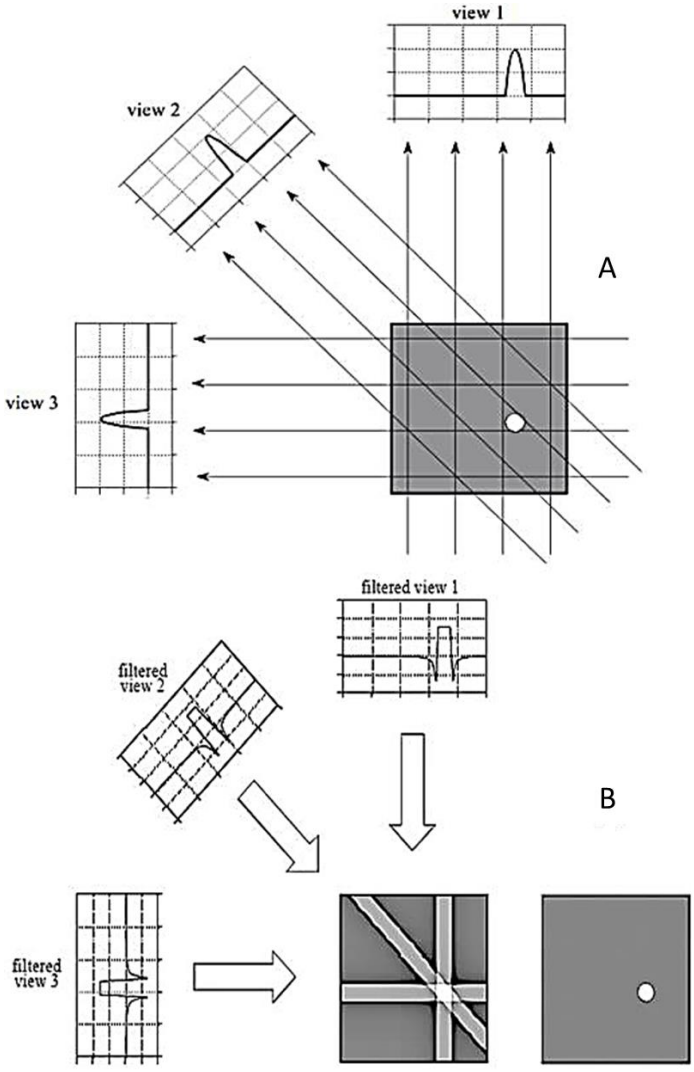

Figure 2.8. Scheme illustrating the filtered backprojection method for reconstruction of X-ray CT images. (A) Cross-sectional simple specimen (cylinder), with arrows describing X-ray energy propagation and the line integrals indicating local X-ray attenuation of the specimen at different angles. (B) The 2D image is reconstructed by backprojection method taking and filtering each view along the path it is originally imaged. Filtering is performed before the back-projection step to remove blurring (Smith, 1999).

The radiographic images of the object captured from different angular positions express a decrease in intensity corresponding to the position of the investigated object. The backprojection algorithm reconstructs an image by smearing each view back along the path it is originally acquired. This process is repeated for all projection images from different angles and the image of the scanned object is then reconstructed. A full 3D virtual sample is built while the reconstructed CT images are rendered (Smith, 1999). The image, as a 3D matrix, can be viewed from different orientations such as coronal, sagittal, and transaxial 2D planes. In image processing, the reconstructed CT images can be flexibly processed, manipulated, and modified (Alsleem and Davidson, 2013).

2.5.3 CT image processing

The reconstructed CT image basically only interprets the density difference of the scanned material from its distinct grayscale intensity. For the other material properties (area, volume, etc.) and 3D visualization, the CT image subsequently needs to be processed and manipulated to extract the required information. The success of image processing is frequently disturbed by noise that represent unreal features in the image (Russ, 2015). Three main sources of the noise in an image are quantum noise, physical limitations of the system, and the generation process of the image (Hsieh, 2009). The quantum noise is related to the X-ray flux influenced by scanning protocols (the energy, speed, slice thickness, etc.). The physical system limitations include electronic noise in the detector photodiode and data acquisition system, and scattered radiation. The image generation process is related to the reconstruction algorithms, reconstruction settings, and effective calibration. The removal of the noise is required to enhance the appearance of the actual objects and, hence, ease the next steps of image processing.

Noise removal can be done by means of filtering which works directly on the actual pixels of the image; a number of different filtering methods are available such as mean filtering, median filtering, and Gaussian filtering (Solomon and Breckon, 2011). For grayscale images, the median filter is the most common

filter to minimize the image noise by simply searching the median of the range of the gray values and replacing the extreme gray value with that median value (Solomon and Breckon, 2011; Russ, 2015). Excessive filtering may, however, degrade fine details of the image (Balafar, 2012). Image segmentation is the next step of image processing when a specific object needs to be isolated and analyzed. It is straightforward once the targeted object poses distinct pixel values from the other objects. The method commonly used is based on a t-test, searching the limit or threshold value that separates the lighter and darker intensity values (Otsu, 1979).

2.5.4 X-ray CT factors

2.5.4.1 Spatial resolution

Spatial resolution of the X-ray CT scan is a key factor that determines the quality of CT images and, hence, the reconstructed 3D geometry. It is the ability of the reconstructed CT image to visualize specific features with different contrasts in the image (Mendoza *et al*., 2007). Sufficient resolution is required, not only for the visualization of tiny features of the sample but also for image processing steps. In the field of postharvest research, a high resolution scan allows to detect tiny features of the fruit tissue, such as pores and cells. As air or gasses have a much lower density than water, the resulting X-ray attenuation coefficient of both phases is different, producing sufficient contrast between the pore (air) and cell (water) fractions (Vincent, 2019). Using high resolution X-ray CT with a voxel resolution of 1 to 5 µm, Verboven *et al*. (2008) discovered 3D gas exchange channels in 'Jonagold' apple and 'Conference' pear. As the contrast between cytoplasm and cell wall is much smaller, it proved to be difficult to segment dense cell clusters into individual cells. Wang *et al*. (2017) improved the image contrast using contrast agents such as cesium iodide to segment dense cell clusters in micro CT images of apple.

Mendoza *et al*. (2007) found that pores and cells of 'Jonagold' apple tissue could not be well segmented in X-ray CT images when the resolution was below 13.7 µm per pixel. However, an increase in resolution typically implies a decrease in the field of view (FOV). For imaging entire fruit, for example, creation of geometrical models of intact fruit (Ho *et al*., 2011; 2013b) or inspection of internal defects in horticultural products, a large FOV is required and the resolution that can be obtained is currently considerably coarser than would be required for segmenting cells and pores (Lammertyn *et al*., 2003a,b; Herremans *et al*., 2014b; van Dael *et al*., 2017). As the FOV increases so does the pixel size; resulting in a decrease of spatial resolution. The reconstructed CT image will rather only show varying grayscale intensities that are affected by the local density and porosity of the tissue within one image voxel (partial volume effect) (Tanaka *et al*., 2018). Recently, an attempt to overcome this limitation was conducted by Janssen *et al*. (2020a). Pore and cell populations in a 'Braeburn' apple were successfully defined by optimizing the segmentation procedure of the coarse image based on a corresponding segmented high resolution tissue image. This allowed them to analyze the porosity and connectivity in the coarse image of the entire fruit.

2.5.4.2 Image artifacts

Another issue in applications of X-ray CT are artifacts in the reconstructed CT images (Tan *et al*., 2012; De Chiffre *et al*., 2014). Streaks, rings, motions and beam hardening are the artifacts commonly encountered. Understanding of these artifacts and their correction procedure is crucial as quantitative analyses of CT images that rely on the measured grayscale intensity may be impaired by the artifacts. Quality assessment of the X-ray CT image is normally carried out by scanning a homogeneous water phantom (Ritschl *et al*., 2010; Gulliksrud *et al*., 2014).

Consistency and uniformity are two aspects that have to be taken into account in the quality assessment of CT number or grayscale intensity of the phantom CT image (Hsieh, 2009). Grayscale consistency means that the grayscale intensity

of the phantom imaged is not largely affected by its dimensions when taken at different times or when imaged together with other objects (Hsieh, 2009). Variation in the greyscale of a scanner over time most likely implies less consistency that can be caused by scattered radiation (Shaw, 2014), unstable energy affecting inconsistency in the exposure (Brown and Brown, 2018), system malfunction (Goldman, 2007), and sample motion (Goldman, 2007; Shaw, 2014). Grayscale uniformity dictates that a homogeneous phantom should ideally have the same grayscale intensity at different positions in the selected region of interest (Hsieh, 2009).

Beam hardening is the artifact that considerably changes the uniformity and consistency of the grayscale intensity of a homogeneous material. This artifact is basically caused by the polychromatic X-ray beam traveling into the material. When low energy photons (i.e., soft X-rays) are completely attenuated at the material edge, the remaining high energy photons (i.e., hard X-rays) are just less attenuated and reach the detector (Davis and Elliott, 2006; Kruth *et al*., 2011). This effect leads to a darker region at which the sample appears less dense at the center of the homogeneous material than at its boundary (Davis and Elliott, 2006; Meganck *et al*., 2009; Tan *et al*., 2012), as shown in Figure 2.9. This artifact highly affects the accuracy of density measurement (Segal *et al*., 1987; Zou *et al*., 2011). As most laboratory CT systems utilize sources that radiate polychromatic X-ray spectra, errors due to beam hardening must be corrected by accurate quantitative analysis of the image (Meganck *et al*., 2009).

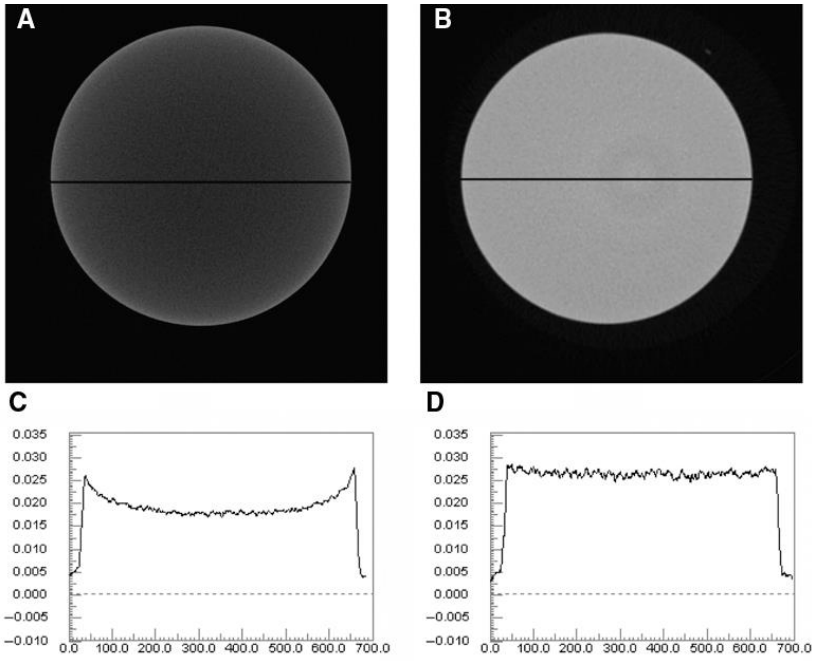

Figure 2.9. Correction of the beam hardening artifact. (A) cross-section of 12-mm homogeneous sample without application of a beam hardening correction. (B) The same sample as (A), but with application of beam hardening correction. (C) X-ray intensity profile across the image (A). (D) The profile across the image (B) (Zou *et al.*, 2011).

A reduction method of beam hardening artifact is to place a thin plate, e.g., Cu or Al, in between the X-ray source and the scanned material to filter out the soft X-rays and to allow the CT attenuation measurement with only the hard beam spectrum (Kruth *et al*., 2011). However, this approach may reduce the intensity of X-ray and has to be compensated by the increase of the exposure and measurement time, which potentially causes dehydration of the fruit tissue sample. Beam hardening can be corrected during the image reconstruction using reconstruction softwares. In principle, it numerically fixes beam hardening using a polynomial correction (Kruth *et al*., 2011). Beam hardening correction (BHC) improves the uniformity of CT images of single phase materials (Tan *et al*., 2012) and, therefore, minimizes the dimensional errors in the scanned object (De Chiffre *et al*., 2014).

2.5.5 Geometrical models of fruit microstructure

As described above, the tissue microstructure of fruit and vegetables is complex and varies between species, cultivars, individuals, and between positions within the individual fruit. Realistic tissue microstructure models are crucial, because they are used to compute gas transport properties in the multiscale concept. X-ray micro CT is a powerful technology to provide detailed 3D images of a tissue based on which microscale geometrical models can be constructed. Such geometrical models can then be used to compute gas transport by means of a voxel-based finite element method (Ho *et al*., 2011). However, since the 3D microstructure image consists of a large number of voxels, the calculation process may require large computer resources and long computational times (Mebatsion *et al*., 2009).

Alternative approaches of X-ray CT have been proposed to realistically model the 3D geometry of fruit tissue, cell walls, pore channels and cells (Mebatsion *et al*., 2009). The cell models were generated based on a novel ellipsoid tessellation algorithm that also creates a 3D pore network. The cell wall thickness was obtained from transmission electron microscopy (TEM) since the resolution of the CT scan was not sufficient to measure it. Once the *x*,*y*,*z*-coordinates of each cell wall from the CT image were set up, ellipsoids that match these points were created by means of a Least Squares Fitted Ellipsoid (LSFE) algorithm (Mebatsion *et al*., 2008; 2009). The resulting virtual model of the fruit tissue was comparable to the actual CT image (Figure 2.10). It described geometrical features of cells and cell walls and the connectivity of the pore network, which are crucial for mass transport.

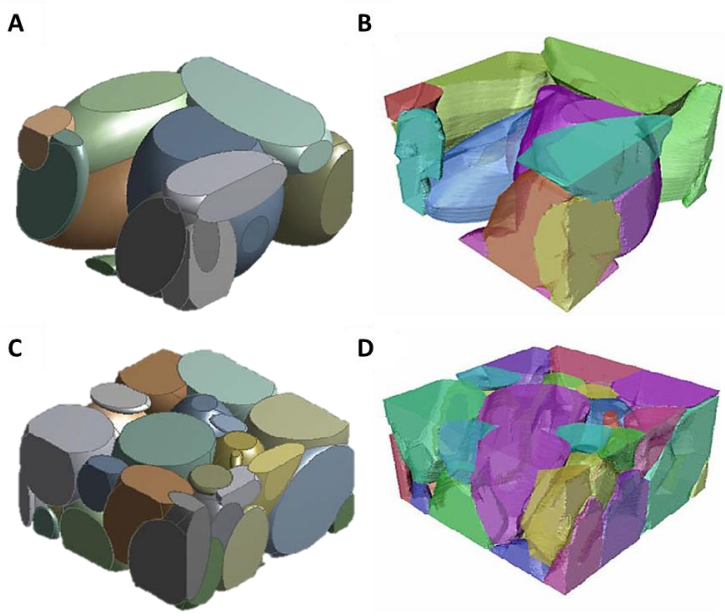

Figure 2.10. Tissue geometries of (A and B) apple and (C and D) pear obtained based on (A and C) the geometrical model and (B and D) X-ray CT. The sample dimensions were 315×315×168 µm. The images are adapted from Mebatsion *et al*. (2009).

Physical damage in fruit such as bruises causes cell wall rupture and intercellular separation. As the micro-mechanical behavior of that process was not quantified yet, Diels *et al*. (2019) developed a 3D tissue model based on the discrete element method (DEM). The model represented the tissue as a mass-spring system to model mechanical behavior of tomato tissue upon large stresses. The cell was modeled as a deformable shell, represented by a visco-elastoplastic triangulated mesh under turgor pressure. In the cell wall, deformation was modeled under the assumption that (i) the cell wall can be considered as a spring connection that breaks at a certain critical stretch ratio, and (ii) a ruptured cell is turgorless. The modeled tissue (cell area, volume, and anisotropy distribution) was in agreement with X-ray micro-CT images of real tomato tissue.

The topology of the pore network affects the gas transport through the porous tissue. In our research group, an alternative way of modeling microscale gas

transport in porous media has been proposed by Ho *et al*. (2014) who used a pore network scale model. The approach basically relies on a simplification of the real pore structure by representing the pores as nodes connected by networks. Construction of the pore networks is based on an X-ray CT scan of which the resolution allows capturing cell and pore fractions of the tissue. Each fraction is further separated into individual pore and cell by employing a distance transformation to those voxels belonging to the cell region. The final pore scale network is composed of nodes connected to their neighbors where each node represents the individual pores and cells. The pore network scale model enables to compute effective O_2 and CO_2 diffusivities that were comparable to measured data and predicted diffusivities based on the microscale continuum model (Ho *et al*., 2014). This approach offers a promising alternative for gas transport modeling, especially for a larger tissue sample.

2.5.6 Geometrical model of entire fruit

The shape of a horticultural product determines the transport of respiratory gasses inside it. In gas exchange modeling, a geometrical model of the fruit or vegetable is required as a model input to predict internal gas gradients. Basic shapes, such as spheres and cylinders, which are to some extent similar to the investigated sample have been used before (Mannapperuma *et al*., 1991; Abdul-Baki and Solomos, 1994), but important shape features were lost. This may result in a less realistic prediction of internal gas concentration.

Realistic fruit or vegetable geometries have been constructed based on photographs of slices (Goñi *et al*., 2007), or from different angles (Moustakides *et al*., 2000; Lammertyn *et al*., 2003a), X-ray CT (Ho *et al*., 2011; Herremans *et al*., 2014a) and MRI (Goñi *et al*., 2008). However, the use of such techniques is not practical when many geometrical models are needed. A fast shape model generator was developed by Rogge *et al*. (2015) based on actual 3D shapes of apple extracted from X-ray CT. Coordinates of the outer shape contour were transformed to spherical coordinates and described with 2D Fourier descriptors that were statistically characterized. New geometrical models of apple were

constructed by generating samples of the descriptors using a Monte Carlo technique and then applying the reverse procedure. The created geometries can be readily used as inputs for gas exchange simulations. A similar procedure that uses principal components instead of trigonometric functions as basic functions was developed (van Dael *et al*., 2017; Huijs *et al*., 2018).

2.6 Conclusion

Many attempts have been made to model respiratory gas transport for predicting internal gas concentrations in pome fruit, but some issues remain unsolved. As fruit or vegetables are composed of different tissue layers with a heterogeneous microstructure, the assumption of uniform gas transport parameters in the model may result in inaccurate predictions, particularly in very low oxygen conditions such as encountered under ULO or DCA. Such conditions may cause lower O_2 levels inside the fruit than the O_2 in the storage atmosphere due to the tissue resistance. While uniform models would result in smooth gas gradients across tissues, accounting for the heterogeneous structure could result in more complex patterns. Also, a heterogeneous model may result in different local minima of the oxygen concentration or RQ value inside the fruit. Both aspects are expected to allow interpreting the occurrence of disorders better.

However, because of the difficulty of currently available X-ray CT systems to obtain images with a FOV that covers the entire fruit while providing micrometer resolution it is currently impossible to map the microstructure of entire fruit and vegetables and solve respiratory gas exchange models directly over this computational domain. Alternative approaches will be required that combine low and high resolution X-ray imaging and advanced gas transport models. This will be explored in the next chapters.

Chapter 3

Non-destructive porosity mapping of fruit and vegetables using X-ray CT

This chapter is adapted from **Nugraha, B.,** Verboven, P., Janssen, S., Wang, Z., Verboven, P. Nicolaï, B. 2019. *Non-destructive porosity mapping of fruit and vegetables using X-Ray CT*. Postharvest Biology and Technology, 150, 80-89. doi: 10.1016/J.Postharvbio.2018.12.016

3.1 Introduction

Some quality changes in fruit and vegetables are known to be related to transport of respiratory gasses during the postharvest supply chain and storage (Lammertyn *et al.*, 2003b; Herremans *et al*., 2013). Fruit and vegetables contain heterogeneously distributed pores that affect transport phenomena of respiratory gasses (Janssen *et al*., 2020b). Parts of a plant tissue that have smaller intercellular air spaces can potentially restrict gas diffusion leading to decreased internal O_2 and accumulated internal CO_2 concentrations (Dražeta *et al*., 2004; Ho *et al*., 2011; Yamauchi *et al*., 2018). Franck *et al*. (2007) explained that fermentation in apple might occur locally at a particular position depending on the tissue microstructure. This hypoxic or anoxic stress may result in cell death, eventually causing internal disorders and cavities (Pedreschi *et al*., 2009). Porosity measurements at a particular area of a plant organ are not sufficient to describe the heterogeneity of porosity in the whole organ (Mendoza *et al*., 2007) that may determine respiratory gas transport. Therefore, quantitative mapping of porosity distribution in an entire plant organ is highly essential for better understanding gas transport and how it affects respiration after harvest. Additionally, porosity also plays a role in the textural properties of cellular foods (Gueven and Hicsasmaz, 2011; Ozuna *et al*., 2014).

A large number of techniques have been implemented to calculate the porosity of fruit and vegetables. X-ray computed tomography (CT) is a well-known technique for quantification and characterization of internal structures in porous materials. At the macroscale level, the application of X-ray CT has been utilized

for investigating the change of tissue structure as a consequence of mealiness development in pear (Muziri *et al*., 2016), or browning disorder and cavities in pear and apple (Lammertyn *et al*., 2003a,b; Herremans *et al*., 2014b). At the microscale, X-ray CT has been used to visualize and assess the porosity of agricultural products such as mango (Cantre *et al*., 2014), apple (Mendoza *et al*., 2007; Herremans *et al*., 2015a,b), and pear (Herremans *et al*., 2015a). However, the direct ability of X-ray CT to enable quantification of porosity of a whole product has been limited by the fact that high resolution X-ray imaging is only possible for a limited field of view (FOV) and requires destructive sampling of the product to obtain a specimen with an appropriate size for imaging. The heterogeneity of the porosity of a whole apple and tomato has been successfully quantified and mapped by utilizing magnetic resonance imaging (MRI) (Musse *et al*., 2010; Winisdorffer *et al*., 2015). MRI detects differences in magnetic sensitivity between intercellular pores and their environment inside fruit tissue. However, the typical spatial resolution obtained by MRI is much lower than that of X-ray CT (Herremans *et al*., 2014b).

The variation in grayscale intensity of CT images is a consequence of differences in X-ray attenuation, mainly expressing variation in density of the internal structure of biological materials (Azeredo *et al*., 2013). While plant tissues are composed of similar elements with similar attenuation, differences in cell composition will not largely affect attenuation. On the other hand, air has a much lower X-ray attenuation than organic material (Seeram, 2010); therefore high intensity voxels in an X-ray CT image of horticultural products indicate a more dense tissue structure. Hence, it can be reasonably assumed that CT image grayscale variations correlate well with porosity. Once the correlation is known, the stack of the grayscale CT images can be translated into 3D porosity maps of fruit and vegetables. A porosity map of a persimmon based on X-ray CT images was generated by Tanaka *et al*. (2018). However, two essential aspects of the CT performance evaluation, namely uniformity and consistency of the produced images, were not addressed but need to be considered to make the method easily transferable to other species or products.

As mentioned earlier, uniformity is a measure of how identical grayscale intensities are in each region of interest within a homogenous phantom object (Hsieh, 2009). It is commonly linked to beam hardening artifacts that may reduce the accuracy of the grayscale CT image-based analyses (De Chiffre *et al*., 2014). Consistency is a measure of how similar the results are of the same phantoms scanned at different times (Hsieh, 2009). Inconsistency may result in a large variation of grayscale intensity between CT measurements (Shaw, 2014). The robustness of X-ray CT-based approaches to predict and depict variability of entire product pore structures of a wide range of fruit and vegetables has not been widely explored.

In this chapter, a validated and reproducible method is elaborated to map the porosity distribution of different fruit and vegetables extracted from CT images for a range of horticultural products. Four different plant organs representing fruit and vegetables with different porosities were investigated: 'Jonagold' apple, 'Conference' pear, 'Purple-top' turnip and 'Purple-globe' eggplant. Uniformity and consistency assessments were introduced by including a homogeneous water phantom to evaluate the CT image quality by means of beam hardening correction (BHC). Furthermore, to ensure that the method is easily transferable to other devices and products, as well as accounting for time effects, a normalization procedure of the images is proposed using appropriate water and juice phantoms, thereby progressing beyond the available porosity mapping methods.

3.2 Materials and methods

3.2.1 Samples

'Jonagold' apple (*Malus x domestica* cv. 'Jonagold'), 'Purple-globe' eggplant (*Solanum melongena*), 'Purple-top' turnip (*Brassica rapa subsp. rapa*) and 'Conference' pear (*Pyrus communis L.* cv. 'Conference') were collected from the local market and immediately transported to the laboratory for scanning. These products have different microstructural characteristics. Pear has the densest microstructure with a 6 % porosity (Herremans *et al*., 2015a) followed by turnip and apple with a porosity of 21 – 25 % (Mendoza *et al*., 2010; Lech *et al*., 2018), and eggplant with 60 % void spaces (Gras *et al*., 2002). Five replicates of each product were imaged and analyzed. Appearance and absence of physical defects were the basis of product selection.

3.2.2 X-ray computed tomography

3.2.2.1 Low resolution CT scan

Figure 3.1A describes the general scheme of the research method. Firstly, the individually intact samples were scanned with a Microfocus Computer Tomography AEA Tomohawk system (Department of Materials Engineering, University of Leuven, Belgium) operated at a voltage of 120 kV and a current of 215 µA, without a filter. These powers enabled the X-ray beam to propagate through soft tissue materials such as fruit and vegetables, producing CT images with low noise levels. The sample and detector distances to the X-ray source were set at 746 mm and 1085 mm, respectively, to accommodate an entire sample scan with 132.2 µm pixel resolution, approximately lasting for 30 min per scan. Combination of these settings was inadequate to visualize individual pores of the samples, but appropriate to describe tissue density differences in the entire sample organ with distinct grayscale levels. Proper grayscale CT images are crucial to generate a porosity distribution map.

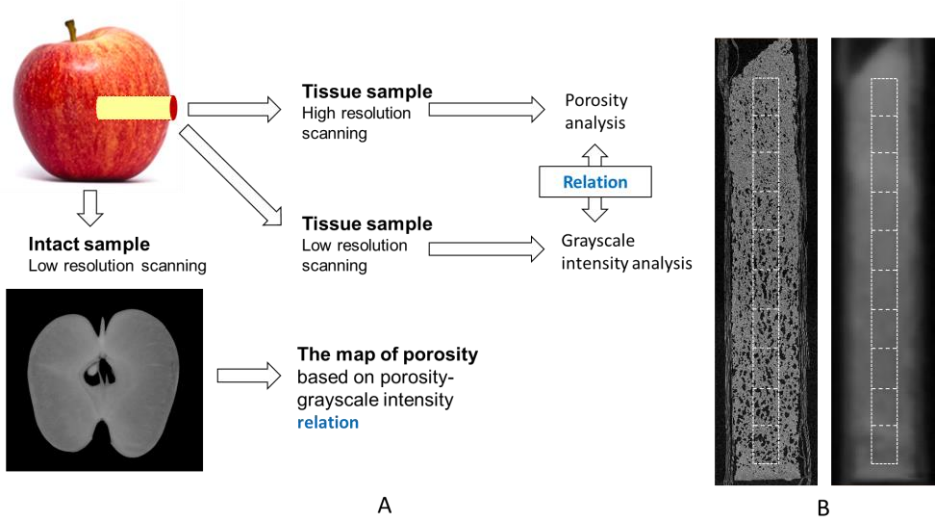

Figure 3.1. (A) Schematic flow of the experimental procedure. (B) X-ray CT images of radially cylindrical tissue at high (left) and low (right) resolution. The dashed lines on both tissue images indicate the VOIs used for the regression analysis.

Secondly, a cylindrical tissue sample with a diameter of 3.8 mm was excised along the equator of the intact sample and scanned under the same setting as the intact sample (Figure 3.1B). The tissue sample was then covered by a parafilm to prevent water loss during scanning. In the end, the remaining individual samples were juiced and then scanned in a small plastic tube under the same setting to image a zero porosity reference of each sample.

Uniformity and stability of grayscale intensity of the X-ray CT images were evaluated using water due to its similar X-ray attenuation to biological tissues. Two kinds of phantoms were prepared from distilled water boiled up to remove microscopic air bubbles. The first phantom was distilled water inserted into a plastic ball or a bottle approximately fitted with the size of the scanned sample. This sample-like phantom was imaged in every scanning batch of the same products under the same setting to evaluate the uniformity. The second was a small water-filled tube (diameter 3.50 mm) scanned together with the sample (cylindrical tissue or intact sample) to check the consistency of the resulting grayscale values of X-ray CT scanning over time.

3.2.2.2 High resolution CT scan

In order to quantify the actual porosity, high resolution X-ray CT scans of the excised cylindrical tissue were performed at 2.60 µm (pear) and 4.00 µm (apple) pixel size using a Phoenix Nanotom-m system (GE Inspection Technology, Wunstorf, Germany) and at 4.87 µm (eggplant and turnip) pixel size using a Skyscan 1172 system (Bruker micro CT, Kontich, Belgium) as shown in Figure 3.1B. The first system was operated at 66 kV and 200 µA; the second was run at 60 kV and 167 µA. Good protocols for the Skyscan had already been established for apple in our previous work (Herremans *et al*., 2013; 2015a,b) and these were implemented for the turnip and eggplant, which are both high porosity tissues. However, due to some limitations, the system is insufficient for pear with low porosity. Therefore, the more technically capable Nanotom system for higher resolution scans (> 4.00 µm) was used for pear. Nanotom could have been used for all samples, but practical constraints (availability of the machine) did not allow so. However, since the Skyscan protocols are reliable, this is not an issue. The implemented resolutions were adequate to visualize the cells and void spaces of the excised cortex tissue (Figure 3.2). A multiple-scan mode was selected to scan long radial tissue samples that were larger than the field of view of the X-ray detector. This mode divided the scanned cortex tissue into 5 to 7 parts. Eventually, a complete structure profile of radial tissue was obtained after 2 – 4 hours of scanning for each sample.

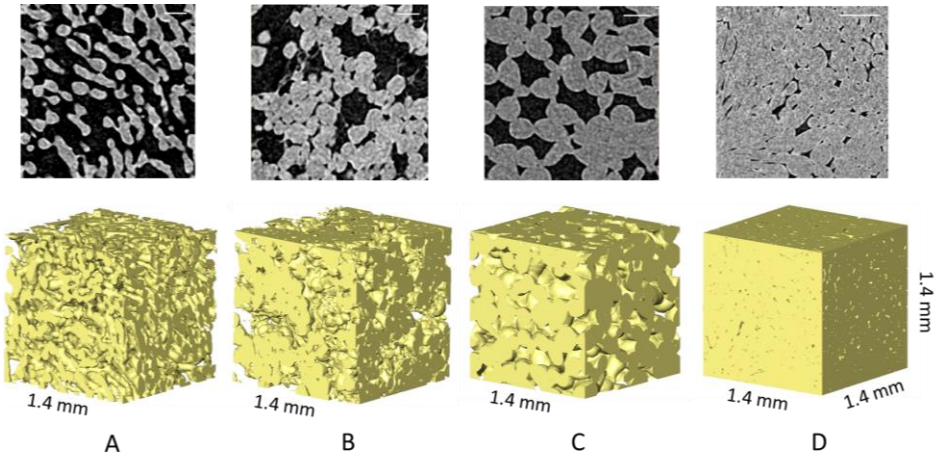

Figure 3.2. High resolution tissue images (top) and 3D tissue models (bottom) of (A) eggplant, (B) turnip, (C) apple and (D) pear at the middle of radial cortex tissue. Gray pixels represent the cells of the tissues. Scale bar indicates 600 μm.

3.2.3 Reconstruction and image processing

The projection images from the low resolution scans were reconstructed using Octopus Reconstruction (Octopus Imaging Software, Ghent, Belgium), while the images from high resolution scans were reconstructed using Phoenix Datos x CT Software (GE Inspection Technology, Germany) and NRecon (Bruker micro CT, Kontich, Belgium). These reconstructions generated stacks of 8-bit grayscale images.

The sample-like phantom was reconstructed with different beam hardening correction (BHC) levels to evaluate the uniformity. Beam hardening artifacts were present when the center part of the uniform phantom appeared darker than its periphery. To remove this artifact, the polychromatic X-ray beam leading to beam hardening errors is transformed into an equivalent monochromatic X-ray beam with a linearization procedure (Zou *et al.*, 2011). This is done by polynomial beam hardening correction (Ketcham and Hanna, 2014). Once the value of the so-called BHC factor is set properly, the beam hardening error can be minimized.

The reconstructed phantom images with different BHC levels were imported into Matlab 17.b (The Mathworks, Inc., Natick, MA) to further check the grayscale intensity profiles along the diameter line of the phantom image. The BHC level relatively producing a constant grayscale profile was then implemented for the reconstructions of all low resolution projection images of the samples. In addition, five small volumes of interest (VOI) at different positions of the corrected phantom image were selected and mean gray values in each VOI were calculated. With 95 % confidence level, the confidence interval of the means revealed that grayscale values varied within an acceptable range (± 2 on the 256 scale).

The following image processing steps were performed using Avizo 9.4 (VSG, Bordeaux, France), Data viewer (Bruker micro CT, Kontich, Belgium) and Matlab. Separated parts of the high resolution-scanned cortex tissues were merged by registering and merging the overlapping regions of each tissue section. VOI were determined along the tissue sample by excluding the sample edges that were damaged due to sampling. A median filter was then implemented to reduce image noise. Next, the pores and cells were segmented by Otsu's thresholding, a well-known method for grayscale image segmentation, which selects the best threshold of the image based on a sufficient contrast between objects and backgrounds (Goh *et al*., 2018). The method, therefore, allows the separation of pores (as zeros) and cells (as ones) of the tissue image. Porosity was calculated from the ratio between the volume of pore fraction and the total volume of the analyzed cortex tissue.

To obtain a correlation, the VOI on the low resolution tissue images was approximately positioned at the same VOI on the high resolution tissue images. Once the identical VOI were found, the unspecified tissue region of the low resolution tissue images was excluded. Both the low- and high resolution tissue images were then imported into Matlab for regression analysis.

The background of the intact plant product image was cleaned to exclude objects such as tape, the small water phantom and noise to only obtain the sample image

for porosity mapping. To this end, a mask was first generated by binarization of the original CT images by means of Otsu's thresholding. Second, the small water phantom and tape were removed manually. Some small low resolution parts in the cortex tissue, which were not selected as tissue during mask binarization, were closed by a filling operation to have them included in the final mask. The original CT images were then masked with this image to clean the surrounding background.

3.2.4 Regression analysis

Regression models between the grayscale intensity and the actual porosity were developed. To achieve this goal, the actual porosity and grayscale intensity were calculated on ten defined VOIs of both tissue cylinder images as described in Figure. 3.1B. The sizes of the VOI were different among the tissue samples depending on the length of radial axis of the cortex cylinder. However, the VOI size was sufficient (± 6.0 mm^3) to compute the representative porosity for apple as the minimum elementary volume which has been estimated to be 1.3 mm^3 (Mendoza *et al*., 2007). It is assumed that the VOI is large enough for the other products as well; a detailed elementary volume analysis was not performed. One millimeter under the skin part was set as the edge of the VOI to avoid an inaccurate analysis due to the damaged peel region of the cropped tissues caused by pressure during sample collection. The grayscale intensity and actual porosity quantified from the identical VOI were then regressed. Grayscale values of the juice and image background (air) defined 0 % and 100 % porosity, respectively, in the correlations.

A single correlation formula for all individual products was defined by means of a normalization procedure. Grayscale intensity values of eggplant, turnip and pear juices were normalized with respect to the grayscale values of apple juice producing the same point of 0 % and 100 % porosities. The linear regression models were fitted by means of the least square's method.

A VOI analysis was performed to determine a VOI size showing the best agreement between calculated and predicted porosity profiles along the radial tissue sample. This was calculated by means of the moving average method. The largest size is the VOI used for the regression analysis, which was then reduced to obtain the other five different VOI sizes: 2.74 mm^3, 1.37 mm^3, 0.53 mm^3, 0.06 mm^3 and 0.01 mm^3. The single regression formula, along with the optimal VOI size, was used to translate the grayscale values of intact fruit CT images into porosity maps.

3.2.5 Statistical analysis

The error of the prediction interval and confidence interval around the regression trend was quantitatively estimated at 95 % confidence level to describe the accuracy of the model. Significance test of difference between the slopes of each product was conducted. The mean plant organ porosity of the repeated analyses was statistically compared by means of ANOVA and Tukey's HSD post hoc test at a significant level of 5 %. Five samples were used for each product. These statistical analyses were conducted using JMP Pro 13 and 15 (SAS Institute Inc., USA).

3.3 Results

3.3.1 Beam hardening correction (BHC) implementation

There are no visual differences on grayscale intensity between corrected and uncorrected phantom images (Figure 3.3A, B and C). However, differences can be recognized in the grayscale intensity profiles along the phantom diameter (Figure 3.3D, E, and F). A concave shape along the diameter of the phantom without BHC indicates beam hardening (Figure 3.3D). After polynomial beam hardening correction, a relatively constant grayscale profile was observed (Figure 3.3E). This showed that the artifact had been corrected. An excessive correction was achieved when the correction factor was increased to 0.15, resulting in a convex grayscale intensity profile (Figure 3.3F).

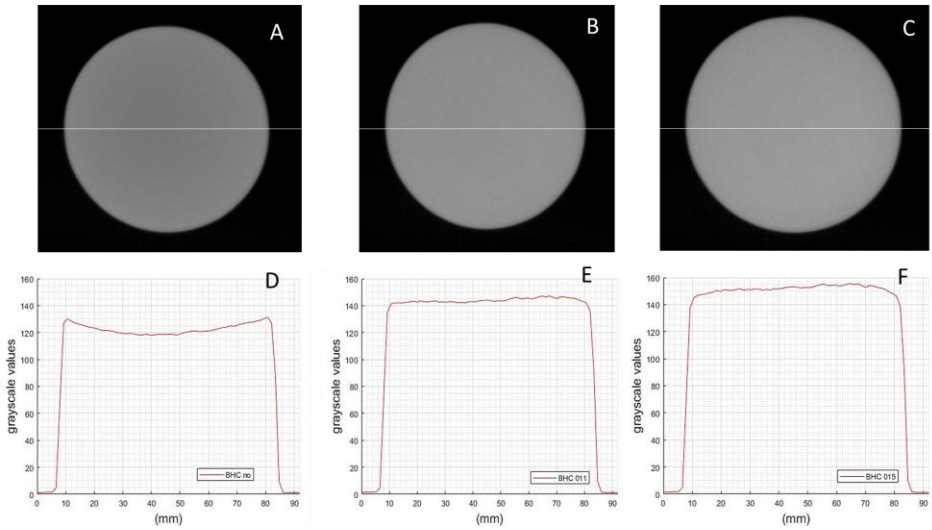

Figure 3.3. Illustration of the beam hardening correction (BHC) applied to a homogeneous water phantom, which has a diameter identical to the analyzed sample. Top images describe the reconstructed phantom images: (A) without BHC, (B) 0.11 BHC and (C) 0.15 BHC. Bottom images are grayscale intensity profiles through the diameter line of the phantom CT images above (D, E, F).

The BHC procedure proved that a suboptimal correction may cause unrealistic gray shades in the reconstructed CT images of the samples, eventually leading to unreliable porosity distribution maps. The optimal value of the BHC was then applied in the reconstruction setting of radiographic images of the samples to refine the beam hardening artifact. The optimum correction value was slightly different for each scanning batch at different time points (0.08 – 0.11), depending on the severity of the artifacts.

3.3.2 Correlation between grayscale intensity and porosity

Grayscale intensity values were plotted versus actual porosity of the excised radial cylinders to study the correlation between both. In this study, the products with the same cultivar were imaged at the same day, yielding identical grayscale of the small phantom of each sample scan. This showed that the correction on grayscale intensities of five replicates of the same product was not conducted. Linear regressions between the grayscale intensity and porosity for the individual products were observed (Figure 3.4A). The grayscale intensity correlated well

with porosity for each product with determination coefficients (R^2) above 0.95 and an RMSE of less than 3 % (Table 3.1). The different slopes of the regression lines ($P < 0.05$) for each species might be caused by the scanning time effect influencing the resulting grayscale values. The normalization procedure on the grayscale value of the juices successfully aligned the regression lines through the same points of 0 and 100 % porosity (Figure 3.4B). This procedure enabled the estimation of a single linear regression model with $R^2 = 0.99$, independent of the scanned samples (Figure 3.4C).

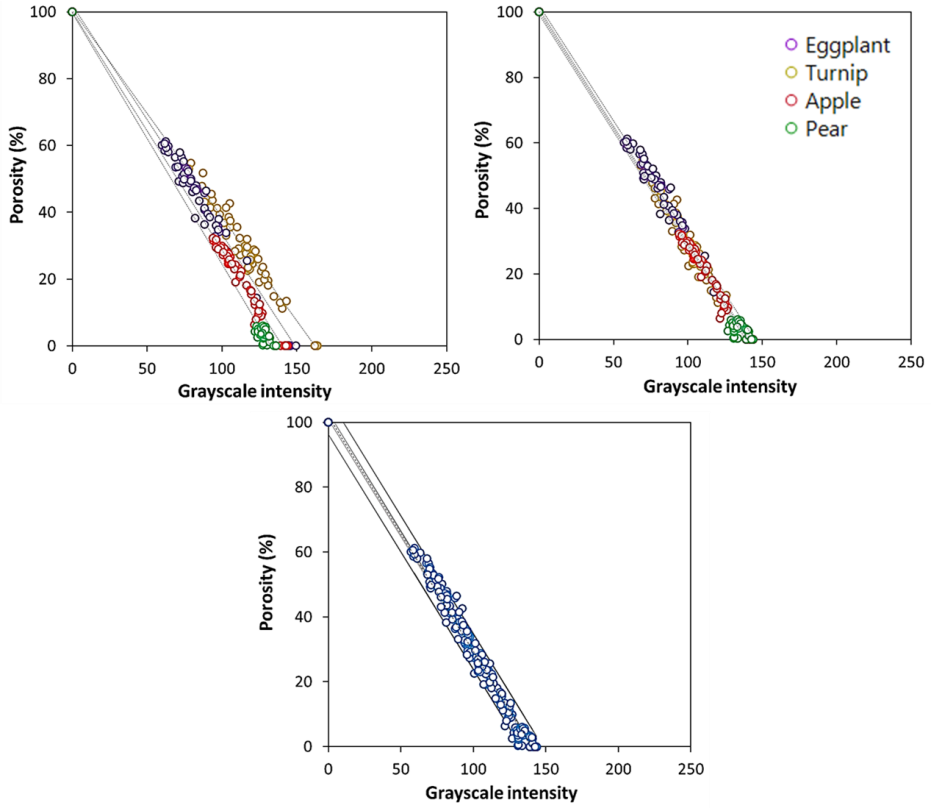

Figure 3.4. Scatter plots of grayscale intensity and actual porosity (%) for eggplant, turnip, apple and pear radial cortex tissues with linear regression lines: (A) before normalization, (B) after normalization and (C) for the normalized values of all individual samples shown along with the 95% confidence interval (inner pair of dashed lines) and 95% prediction interval. The grayscale values were normalized with respect to the grayscale value of the apple juice at 0% porosity.

Table 3.1. Result of the linear regressions of porosity (ε , %) to grayscale (g) for individual products and for all individual products.

	Product	Regression model	R^2	RMSE (%)
Before normalization	Eggplant	$\varepsilon = -0.687g + 102.1$	0.98	2.67
	Turnip	$\varepsilon = -0.621g + 100.7$	0.99	2.64
	Apple	$\varepsilon = -0.714g + 100.0$	0.99	1.76
	Pear	$\varepsilon = -0.752g + 99.62$	0.99	1.88
After normalization	Eggplant	$\varepsilon = -0.704g + 101.9$	0.99	2.60
	Turnip	$\varepsilon = -0.715g + 100.9$	0.98	2.80
	Apple	$\varepsilon = -0.714g + 100.0$	0.99	1.76
	Pear	$\varepsilon = -0.714g + 99.16$	0.99	2.83
	All products	$\varepsilon = -0.727g + 101.9$	0.99	2.78

3.3.3 Radial porosity profile (RPP)

The observed model was tested by comparing the radial porosity profiles (RPP) of the actual and predicted porosities with the six different sizes of VOI (in mm^3). Figure 3.5 shows an example of VOI analysis on the radial cortex sample of eggplant. The smaller the applied VOI sizes, the larger the deviation between predicted and calculated porosity values along the radial cortex tissue. This is due to the increased averaging with increasing volume of the VOI. The second largest VOI size (2.74 mm^3) was used to translate the grayscale CT images of the intact sample to the porosity maps. This size meets the requirement of minimum representative elementary volume (1.3 mm^3) for porosity analysis of apple (Mendoza *et al*., 2007).

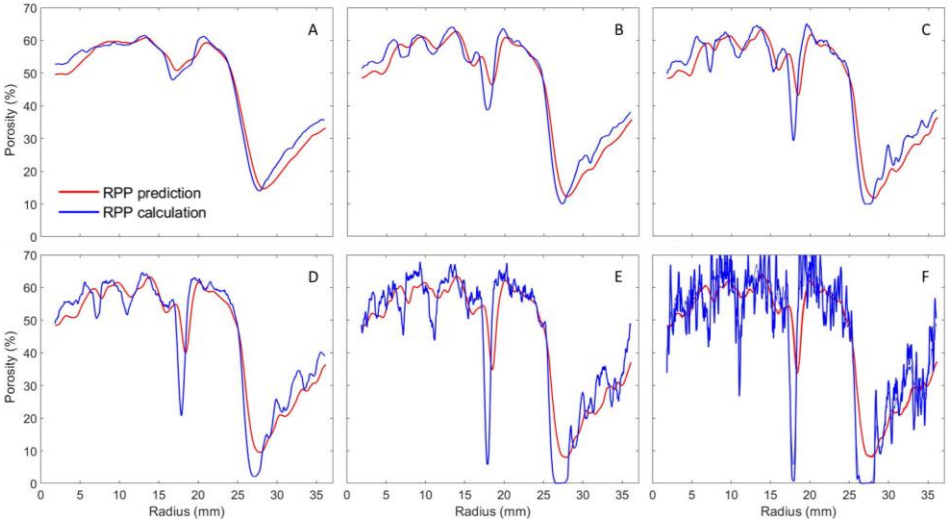

Figure 3.5. VOI analysis between the predicted and observed radial porosity profile (RPP) in eggplant calculated by means of the moving average method with different VOI sizes: (A) 6.73 mm^3, (B) 2.74 mm^3, (C) 1.37 mm^3, (D) 0.53 mm^3, (E) 0.06 mm^3 and (F) 0.01 mm^3. The profiles were plotted between the center of sample cross-section (0 mm radius) and the peel.

The predicted porosity profiles in eggplant, turnip, apple and pear agree well with the calculated profiles with a Root Mean Square Error (RMSE) of 1.5 %, 2.3 %, 2.4 % and 1.5 %, respectively (Figure 3.6). The profiles also indicate that the porosity varied along the radial cortex tissue in apple, turnip and eggplant (Figure 3.6A, B, C), but remained continuously low in pear (Figure 3.6D). The porosity profiles were dependent on the tissue region that was passed throughout the radial direction.

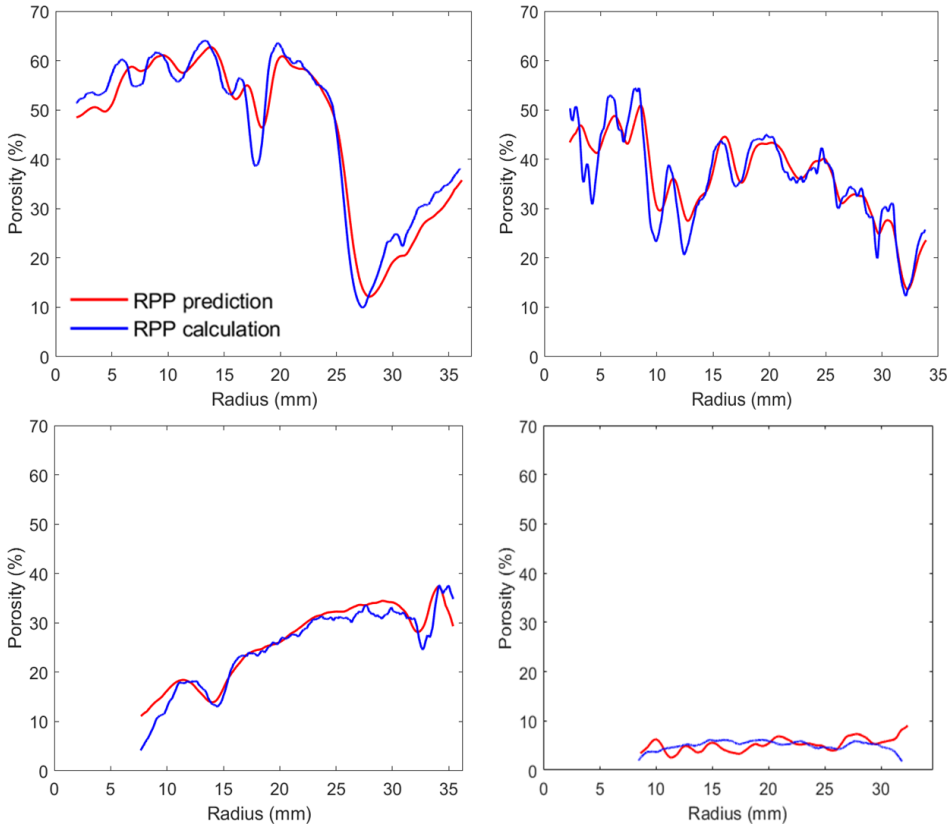

Figure 3.6. Predicted and calculated radial porosity profiles (RPP) of (A) eggplant, (B) turnip, (C) apple and (D) pear plotted between the center of sample cross-section (0 mm radius) and the peel. The predicted porosities were quantified based on the single regression model for all products.

3.3.4 Porosity map of fruit and vegetables

Grayscale CT images of eggplant, turnip, apple and pear (Figure 3.7) were successfully translated into porosity maps (Figure 3.8) based on the single grayscale-porosity regression model. The maps offer 3D information on the distribution of porosity in products in accordance with their anatomy structures. On average, eggplant has the most porous structure (41.8 ± 1.0 %), followed by turnip (23.3 ± 3.4 %), apple (19.7 ± 1.1 %) and pear (4.0 ± 1.6 %).

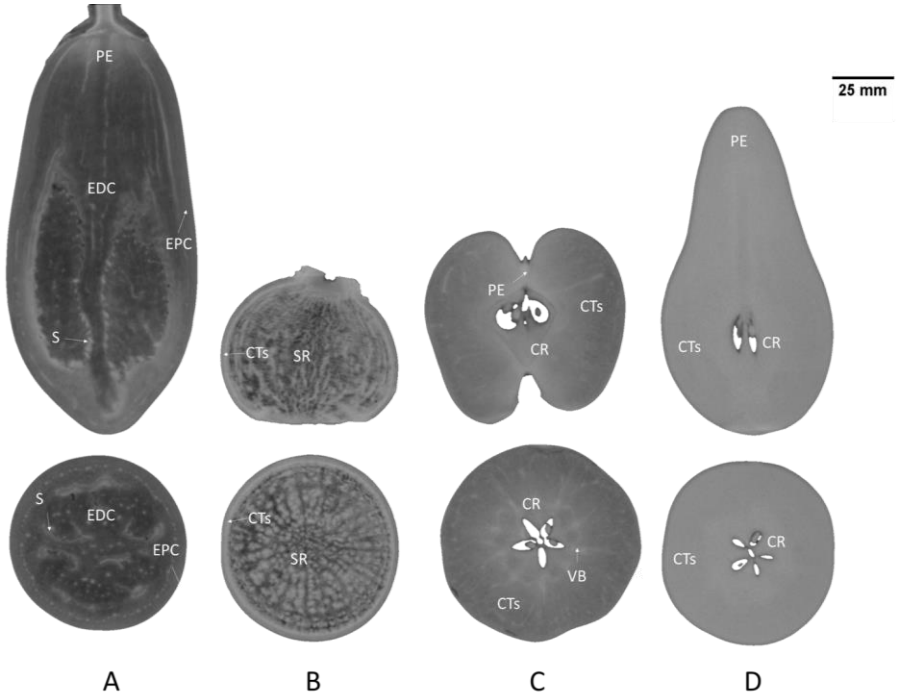

Figure 3.7. Transaxial (X-Y, top) and coronal (X-Z, bottom) slices of grayscale CT images of (A) eggplant, (B) turnip, (C) apple and (D) pear, scanned at low resolution (132 µm. The images show main parts of the products such as endocarp (EDC), epicarp (EPC), pedicel end (PE), group of seeds (S), storage region (SR), core region (CR) vascular bundles, and cortex tissue (CTs).

The heterogeneity in the eggplant porosity is visualized (Figure 3.8A). It can be seen that a large portion of air spaces was concentrated in the inner part (endocarp, EDC) of the eggplant (45 – 65 %) with regional declines in porosity where the groups of seeds are present. Shifting to the outer part of the eggplant flesh (epicarp, EPC), a denser tissue dominated with a porosity of 30 – 45 %. The lowest porosity zones in the eggplant tissue were visualized on the pedicel end (PE) with air spaces of 5 – 20 %.

The turnip structure mainly consists of a storage region (SR) as a central feature, the cambium ring, and the cortex (CTs). The most porous zone (50 – 60 %) in the turnip organ was mainly observed in the storage region (Figure 3.8B) where the vascular systems are typically found. The storage region and cortex were

separated by a thickened tissue layer (cambium ring) with a small air fraction (< 7 %). The cortex tissue located below the epidermis has a porosity of 20 – 30 %.

In the apple, dense tissue structures were primarily centered in the core region (CR) and also in the vascular bundles (VB) with a porosity of 3 – 12 %, while the cortex tissue (CTs) region was considerably more porous (12 – 35 %) (Figure 3.8C). The averaged porosity of the apple mapped from CT images without BHC was 27 % in the core region while the one with BHC (validated) was 16 %, indicating the importance of BHC. In contrast to the other samples, the porosity distribution in the pear organ appeared to be more homogeneous (2 – 10 %) (Figure 3.8D).

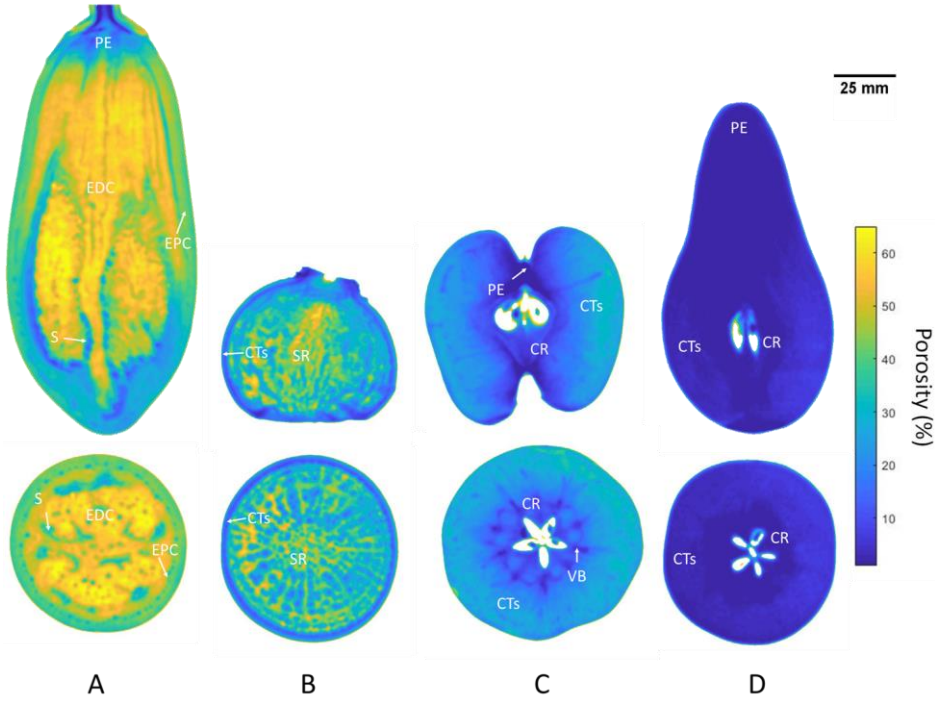

Figure 3.8. Transaxial (X-Y, top) and coronal (X-Z, bottom) slices of porosity maps of (A) eggplant, (B) turnip, (C) apple and (D) pear, translated from the grayscale CT images by means of moving average method with VOI 2.74 mm^3. The porosity maps were predicted by the single regression model for all products. Main parts of the products such as endocarp (EDC), epicarp (EPC), pedicel end (PE), group of seeds (S), storage region (SR), core region (CR) vascular bundles, and cortex tissue (CTs) are shown.

3.4 Discussion

Several methods have been described in the literature to create porosity maps of fruits, either based on X-ray CT (Tanaka *et al*., 2018) or magnetic resonance imaging (MRI) (Musse *et al*., 2010; Winisdorffer *et al*., 2015). X-ray CT is advantageous because it typically produces images with a higher resolution than MRI (Herremans *et al*., 2014b) and provides image intensity that correlates with density. However, it is important to produce reliable grayscale CT images that are free from artifacts. Beam hardening artifacts are the most common error in X-ray CT images that may cause a dim area in the middle of the scanned sample (Davis and Elliott, 2006; Meganck *et al*., 2009), which is easier detectable in a uniform specimen (Hsieh, 2009). The artifact seriously biased the measurement of bone mineral density (Meganck *et al*., 2009), the detection of voids in a porous medium (Kierklo *et al*., 2015) and the construction of 3D geometry (Kruth *et al*., 2011; De Chiffre *et al*., 2014). Here, it was shown that beam hardening may introduce an unrealistic higher porosity in the center area of the products; for example, the apple porosity predicted from CT images without BHC was 9 % higher in the core region than that with BHC. Therefore, there is a clear need for a CT image evaluation step by using appropriate homogeneous phantom materials.

In our study, evaluation on uniformity and consistency of CT images was taken into account to ensure a reliable interpretation of the created porosity map. The uniformity of CT images relates to the occurrences of beam hardening corrected by a homogeneous phantom under identical scanning as described by Hsieh (2009). Reconstruction software-based BHC on the phantom was performed by means of transforming the polychromatic attenuation data into monochromatic data using a BHC coefficient (Ketcham and Hanna, 2014). The consistency is expressed by identical results of grayscale intensities of CT images obtained from different CT measurements. It was corrected by the normalization procedure that is simply adaptable to different scanning times or X-ray devices. Kruth *et al*. (2011) explained that normalization to the grayscale value of water

helps to minimize the X-ray energy dependency, which may induce the variation between CT measurements in medical and industrial CT applications.

For estimating a grayscale-porosity regression equation of different products, grayscale intensities of juice as a proxy for tissue with 0 % porosity and image background (air) reflecting 100 % porosity were required. They define a linear correlation function with an R^2 of 0.99 and an RMSE of less than 3 % for all considered products (Figure 3.4 and Table 3.1). Therefore, this result demonstrates the versatility of the proposed method, only requiring a juice reference scan (to calibrate 0 % porosity) and water phantom (for CT image evaluation) to produce porosity maps of other horticultural products based on the simple linear relation between grayscale and porosity. This presents a significant advantage with respect to previous works (Musse *et al*., 2010a; Tanaka *et al*., 2018). On the other hand, determination of the VOI size used in translating the stack of grayscale CT images into 3D porosity maps by a moving average method was shown to be essential. For too small VOI sizes, the disagreement between predicted and actual porosity profiles was considerable (Figure 3.5).

Porosity maps reported in this study confirm that a biological organ cannot be regarded as a uniform structure (Dražeta *et al*., 2004; Musse *et al*., 2010; Winisdorffer *et al*., 2015; Guelpa *et al*., 2015). Porosity contributes to a large extent to respiratory gas exchanges in fruit (Dražeta *et al*., 2004; Ho *et al*., 2011), water transport during osmotic dehydration process (Lech *et al*., 2018) and ultrasonic drying (Ozuna *et al*., 2014), as well as the oral perception of the flesh texture (Dražeta *et al*., 2004).

Microstructural characteristics play an essential role in the heterogeneity of pore distribution in fruit and vegetables. Large intercellular spaces of eggplant tissue contributes for high porosity values (Fito *et al*., 2001). Puig *et al*. (2012) depicted the two distinct tissues in endocarp (EDC) and epicarp (EPC) sections of eggplant. The former is dominated by tubular and interconnected cells forming high porous structures while the latter is roughly occupied by four to five layers of rounded cells (10 – 25 µm) with a small portion of intercellular spaces. These

characteristics contribute to the high average porosity of eggplant (41.8 ± 1.0 %). This value is lower than that measured by means of the pycnometer method, 59.6 ± 0.5 % (Gras *et al*., 2002). The difference is most likely due to the fact that the sample measured using a pycnometer was only a part of a whole eggplant organ. A similar result was found for the inner part (EPC) of the eggplant (± 60 %) as shown in Figure 3.8A. The high porosity of eggplant determines its spongy texture.

Tuberous root vegetables such as turnip anatomically consist of different regions. They largely contain a storage region (SR) in the middle part where complex xylem tissue mainly exists, including the presence of large pores. The SR is then surrounded by a narrow cortex tissue zone and epidermis at the outer layer (Zaki *et al*., 2012). The porosity map of turnip successfully described the pattern of porosity distribution at each region. The highest proportion of air spaces in turnip is situated at the SR where water and some nutrients are stored and transported. Even though a large portion of air (50 %) was present in the SR, the mean porosity of the turnip was similar to that of apple (23.3 ± 3.4 %). Some dense structures in the SR and the cortex zone affect the mean porosity of turnip. The observed mean porosity was similar to that reported for 'Kulata cerna' or black turnip (20.6 ± 0.3 %) (Lech *et al*., 2018). The turnip porosity map may contribute to a better understanding of the turnip microstructure which has not been widely explored.

The 3D apple porosity map confirmed the distribution pattern of the porosity in apple tissue reported by other researchers (Dražeta *et al*., 2004; Musse *et al*., 2010; Mendoza *et al*., 2010; Winisdorffer *et al*., 2015; Herremans *et al*., 2015b). In general, the porosity in the core region (CR) is smaller than that of the cortex tissues (CTs). Variability in pore distribution is a consequence of differences in tissue organization and cell packing (Dražeta *et al*., 2004). Herremans *et al*. (2015a) observed that the void space network situated in the CR was more complex and narrower than that in CTs. The apparently low porosity of vascular bundles (VB) is likely caused by the relatively thick vessel structures, water-

filled vessels and compact phloem with companion and parenchyma cells (Herremans *et al*., 2015a). In comparison to the other products, pear fruit have a small air fraction with limited heterogeneity. Despite having a low porosity, the pear cortex is arranged by a more complex void network with connected pathways and a larger number of cells compared to the cortex of 'Jonagold' apple (Verboven *et al*., 2008; Herremans *et al*., 2015a). Ho *et al*. (2011) reported that pore connectivity also plays an essential role in providing main routes of respiratory gas exchange. To study respiratory gas transfers more deeply in a whole product, the connectivity parameter should be included in the analysis by considering gas transport properties of the porous tissue such as diffusivity rather than porosity alone.

3.5 Conclusions

X-ray CT was shown to be a powerful technique to non-destructively and accurately map the porosity distribution of entire fruit and vegetable organs based on a simple linear regression between grayscale and porosity. CT image quality assessment with a homogenous phantom material contributes to correcting CT image intensity and producing accurate porosity maps. The advantage of the developed technique is that it is possible to generate porosity maps for other fresh products by a simple juice sample calibration. The porosity maps will be of considerable value to comprehensively understand transport phenomena of metabolic gasses and water during postharvest handling and storage. Furthermore, this may lead to non-destructive online measurement methods for porosity in the framework of internal quality inspection. Still, porosity maps alone will be insufficient to predict respiratory gas profiles inside fruit. Thereto, in the next chapter, a method will be developed to compute effective diffusivity from the porosity.

Chapter 4

Oxygen diffusivity mapping of fruit and vegetables based on X-ray CT

This chapter is adapted from **Nugraha, B.,** Verboven, P., Janssen, S., Hertog, M.L.A.T.M., Boone, M., Josipovic, I., Nicolaï, B. M. 2021. *Oxygen diffusivity mapping of fruit and vegetables based on X-ray CT.* Journal of Food Engineering. doi: https://doi.org/10.1016/j.jfoodeng.2021.110640.

4.1 Introduction

Low oxygen (O_2) storage of fruit and vegetables may enhance their postharvest life. Gas gradients may exist in them as a result of their low porosity that limits gas diffusion. They may cause anoxic or hypoxic conditions inside the products, eventually triggering internal breakdown leading to disorders (Franck *et al*., 2007). Because of the difficulty of measuring internal O_2 levels noninvasively, gas transport models have been developed to compute them (Ho *et al*., 2010a, 2011, 2013b, 2018). These models are typically reaction-diffusion models and are solved numerically. The main material property in these models is the effective O_2 diffusivity which describes at the macroscopic level the overall ability of the tissue to exchange O_2. Ho *et al*. (2010b, 2011) and Herremans *et al*. (2014) found indeed that a low effective O_2 diffusivity affected the internal O_2 concentration, and tissue samples with different microstructures had different O_2 diffusivity values. Along the radial direction of pear tissue, the effective O_2 diffusivity was small under the skin, larger in the cortex region, and lower again in the core region (Schotsmans *et al*., 2003). Its values range over several orders of magnitude depending on the porosity and pore structure. Denser tissue zones may induce a drop in the effective diffusivity due to the lack of pores that are the prime pathways for the transport of O_2 (Ho *et al*., 2006a).

Different models that relate the effective diffusivity to the porosity of porous material have been presented (Neale and Nader, 1973; Tomadakis and Sotirchos, 1993; Mezedur *et al*., 2002). Those that rely on geometrical simplifications of complex porous materials, however, performed poorly at the low porosity range

(< 50 %) (Mu *et al*., 2007). In porous plant tissues, Ho *et al*. (2010b) demonstrated that effective O_2 diffusivity was correlated to tissue porosity for different apple genotypes and 'Conference' pear. They computed the effective O_2 diffusivity based on a numerical experiment with a microscale geometrical model. Other authors have shown that an exponential relation between effective diffusivity and porosity (Archie's law) is more appropriate (Troeh *et al*., 1982; Navarre-Sitchler *et al*., 2009; Peng *et al*., 2012). This model predicted well the effective gas diffusivity of inorganic porous materials with varying exponents for different pore geometries. The shortcoming of the formula is that it only takes into account one particular phase of the material (the pores), causing zero diffusivity at zero porosity. In plant tissues, however, O_2 may also diffuse through the liquid phase of the cells as well. To take this into account, physics based models for the effective O_2 diffusivity are developed in this study by adapting a parallel model for two phase materials (Ho *et al*., 2006b). Microstructural parameters, such as pore tortuosity (expressing the curvature of the porous network) and pore connectivity (expressing the fraction of open pores), were considered.

So far, the O_2 diffusivity has been assumed to be homogeneous across an entire tissue or organ in gas transport models (Ho *et al*., 2010a, 2016, 2018). Given the considerable heterogeneity of the tissues that are involved, this may not be sufficient to predict O_2 gradients properly in highly heterogeneous horticultural product tissues, as shown in Chapter 3 and by Janssen *et al*. (2020a), and the spatial variation should be incorporated in the reaction diffusion models. However, calculation of the effective gas diffusivity in every position of the organ using the method explained above is not feasible as it requires many small tissue samples to be scanned and analyzed.

Recently, non-destructive tomographic imaging has been applied as a method to map the porosity distribution in intact fruit and vegetable organs. Musse *et al*. (2010) and Winisdorffer *et al*. (2015) utilized magnetic resonance imaging (MRI), while Tanaka *et al*. (2018), Nugraha *et al*. (2019) and Chigwaya *et al*.

(2021a) used low resolution X-ray computed tomography (CT) to create three dimensional (3D) tissue porosity maps of fruit and vegetables. In the maps, the porosity variation within and between tissues such as cortex and core, as well as between the products could be clearly differentiated.

The resulting grayscale CT images, depending on local tissue densities, intrinsically exhibit the obvious variability of the tissue microstructure across the organ. X-ray CT was, therefore, applicable to investigate local tissue changes of intact fruit due to internal browning (Herremans *et al*., 2014b; Chigwaya *et al*., 2021b) and mealiness (Muziri *et al*., 2016). Using a validated porosity-grayscale regression model, the grayscale distribution in a CT image of an intact horticultural product organ could be accurately translated into a porosity map (Nugraha *et al*., 2019). However, the tissue porosity distribution alone is insufficient to study gas transport phenomena in fruit and vegetables. The distribution of the effective O_2 diffusivity should be known to comprehensively understand the susceptibility of horticultural crops to the hypoxia-related internal breakdown. Therefore, for bulky organ tissues of fruit and vegetables that commonly have porosities between 0 % and 40 %, dedicated models of the O_2 diffusivity will be needed.

The objective of this study was to develop a technique to map effective O_2 diffusivity in intact organs of horticultural products using X-ray CT images. Since the porosity information in entire fruit or vegetables can now be obtained simply, it may be used to predict the effective O_2 diffusivity that is a function of microstructural parameters. We thereto consider different products with a wide range of porosity values.

4.2 Materials and methods

4.2.1 Approach

The proposed approach for the diffusivity mapping technique is outlined in Figure 4.1. The starting point of this work are low resolution X-ray CT scans of intact organs and high resolution scans of tissue samples that were reported in

Nugraha *et al*. (2019). The intact organ, first scanned at low resolution, is cut to obtain radial tissue images at high resolution used to compute the effective diffusivity of O_2 at multiple tissue positions along the radius of the organ that serve as ground truth, while at low resolution a porosity profile is obtained. Microscale gas diffusion simulations are performed to obtain the effective diffusivity for all tissue samples using the high resolution images. Total porosity, open porosity and tortuosity of the samples are calculated. Then, regression models are developed and tested. The predicted diffusivity profiles from the low resolution radial porosity maps are then compared to the ground truth from high resolution as a means of validation. Finally, diffusivity maps of complete organs are computed and discussed.

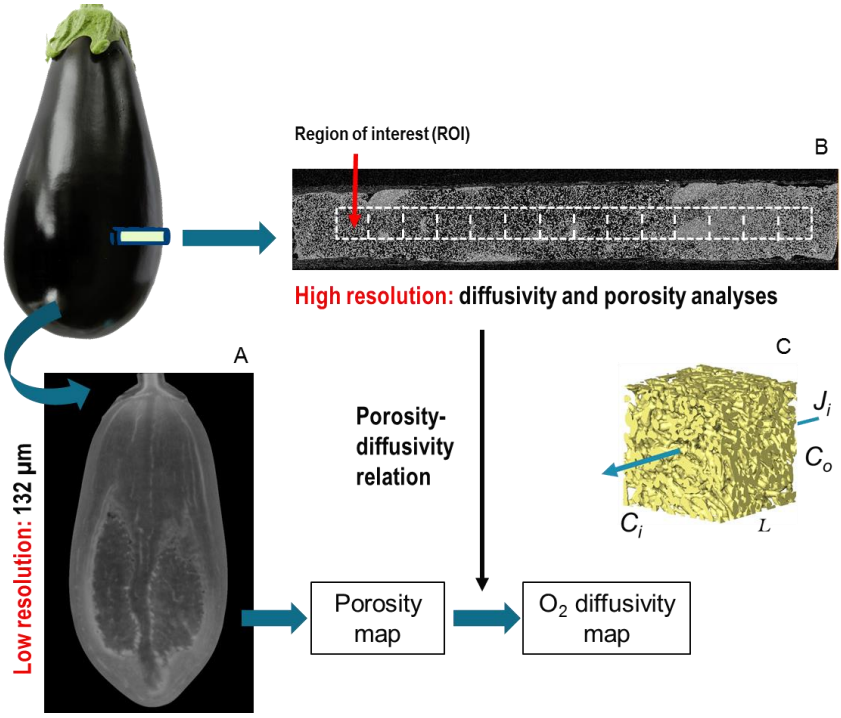

Figure 4.1. Schematic representation of the O_2 diffusivity mapping method. (A) grayscale CT image, (B) CT image of the radial tissue scanned at high resolution and (C) effective O_2 diffusivity calculation on the 3D tissue sample. Two concentrations of oxygen were applied at the left and right sides of the tissue geometry. From the fluxes and length of the sample, the effective tissue O_2 diffusivity was calculated according to the method of Ho *et al*. (2011). Dashed lines on the radial tissue image show the ROIs at multiple positions.

4.2.2 Sample

'Purple-globe' eggplant (*Solanum melongena* L.) fruit, 'Purple-top' turnip (*Brassica rapa* L. subsp. *rapa*), 'Jonagold' apple (*Malus x domestica* Borkh. cv. 'Jonagold') and 'Conference' pear (*Pyrus communis* L. cv. 'Conference') were used for this work. The different species have a considerable variability in tissue porosity as shown in Chapter 3 and characteristics (total porosity, open porosity and tortuosity) of the tissue microstructure. Products at commercial ripening stage and without physical defects were collected from local fresh product markets around Leuven (Belgium) and immediately moved using a plastic box to the laboratory for X-ray CT scanning. As fresh products rapidly deteriorate in ambient temperature, the whole transport process took no longer than an hour, thus minimizing quality degradation. Five individual samples were used for each product.

4.2.3 X-ray CT scans and image processing

The scanning and image processing protocols were already explained in detail in Chapter 3. The intact eggplant, turnip and apple were scanned at 132.2 µm voxel size (Figure 4.1A) using the Microfocus Computer Tomography AEA Tomohawk system (Department of Materials Engineering, KU Leuven, Belgium). Due to insufficient image quality of the pear datasets from the Tomohawk system, pear was scanned at higher resolution (86 µm isotropic voxel size) using the inhouse developed X-ray CT scanner HECTOR of the Ghent University Centre for Tomography (UGCT) (Masschaele *et al*., 2013). Tube settings of 120 kV and 20 W target power (180 µA tube current) were used to image the intact pear. The CT images of the product representing grayscale intensity were translated into porosity values using a porosity mapping technique as explained in Chapter 3.

A radial cortex tissue of the same product was imaged at high resolution using a Phoenix Nanotom-m system (GE Inspection Technology, Wunstorf, Germany) for apple (4.00 µm) and pear (2.60 µm) and using a Skyscan 1172 system (Bruker

micro CT, Kontich, Belgium) for eggplant and turnip (4.87 µm). A 3D microstructural geometry of tissue was generated from the tissue image and used to compute the properties of the tissue structure (Figure 4.1B). A one millimeter slice below the surface and edge of the cylindrical tissue that was damaged due to sampling was excluded from determining the volume of interest (VOI) of the sound tissue. Due to the sufficient contrast between the cell and pore regions**,** **s**egmentation was accomplished by Otsu's thresholding method, which selects the best threshold for grayscale images with respect to the object (cells) and background contrast (pores) (Goh *et al*., 2018). This method has been previously implemented for CT images of different fruit tissues (Cantre *et al*., 2014; Herremans *et al*., 2015a). The threshold values were set to 85, 95, 68 and 80 for eggplant, turnip, apple and pear, respectively. The distinct values can be attributed to the differences in the CT scanner type and resolution used.

The segmentation step produced a stack of binary tissue images where one and zero values represented cells and pores, respectively. The binarized images were then imported into Matlab 18.a (The Mathworks, Inc., Natick, MA) for subsequent analysis. To visualize the physical differences in the intercellular space of the products, the segmented pore fractions were skeletonized in Avizo 9.4 (VSG, Bordeaux, France) (Figure 4.2A, B, C and D). For the purpose of model testing, the same tissue sample was then scanned at an identical resolution as that of the entire sample.

4.2.4 Calculation of tissue structure properties

In Matlab, the binarized tissue images were radially divided into multiple cubical volumes of interest (VOI) at different radial distances from the fruit surface (Figure 4.1B) in order to obtain radial profiles of the tissue microstructural properties and effective diffusivity (see next section). Total porosity, open porosity and pore tortuosity were calculated for each VOI of five radial samples of each species. A representative elementary volume (REV) analysis was conducted to determine the optimal size of the VOI (Supplementary A1). The final REV was 0.8×0.8×0.8 mm^3 that was equal to 162×162×162 voxels for

eggplant and turnip, 198×198×198 voxels for apple and 305×305×305 voxels for pear. The REV was used to calculate all parameters to build the regression models for all species and was also large enough to implement on the low spatial resolution image of the entire organs (equivalent to 6×6×6 voxels).

4.2.4.1 Total and open porosity

The total porosity ε was obtained from the ratio of total pore volume to the total volume of the VOI. Additionally, the open porosity ε_o, defined as the tissue porosity connecting two sides of 3D tissue geometry in the considered direction of O_2 diffusion, was quantified as the ratio of the volume of the connected pores in the radial direction to the total volume that extended from one side of the volume to the other. The average radial profiles of total and open porosity of the organs of the four investigated species are illustrated in Figure 4.2E, F, G and H.

4.2.4.2 Pore tortuosity

Different measures of tortuosity have been defined in different scientific fields. The tortuosity term used here is the diffusive tortuosity, defined as the ratio of the gas diffusivity in free space to the effective diffusivity in the porous material (Clennell, 1997; Shen and Chen, 2007), as expressed in Equation 2.11. It was computed using a Matlab script developed by Al-Raoush and Madhoun (2017) in order to represent the effect of pore space curvature in the calculated O_2 diffusivity. It is based on the average length of all connected pores and normal distance between the two radial sides of the tissue geometry. The more tortuous the pore, the longer it takes for the respiratory gasses to diffuse across the tissue. The average radial profiles of tortuosity from five samples of each studied organ are given in Figure 4.2 I, J, K, and L.

4.2.5 Effective O_2 diffusivity

The effective O_2 diffusivity of the tissue was estimated by applying a validated microscale reaction diffusion model (Ho *et al*., 2011) to the voxelized 3D tissue geometry of each VOI, obtained from a high resolution scan of X-ray CT:

$$\frac{\partial C_{O_2}}{\partial t} = \nabla \cdot D_{O_2} \nabla C_{O_2} + R_{O_2} \tag{4.1}$$

with C_{O_2} (mol m^{-3}) the O_2 concentration in either air (pores) or liquid (cells), ∇ gradient operator (m^{-1}), D_{O_2} (m^2 s^{-1}) the O_2 diffusivity and R_{O_2} (mol m^{-3} s^{-1}) the respiration rate, which is zero in the pores. Steady state was assumed and the respiration term (R_{O_2}) was ignored due to the small size of the tissue sample. The microscale model was thus written as

$$0 = \nabla \cdot D_{O_2} \nabla C_{O_2} \tag{4.2}$$

This equation was discretized over a voxel based mesh representing the 3D tissue geometry using the finite volume method to produce a linear set of equations for unknown O_2 concentration at each node. At the interface between pores and cells, O_2 diffuses through the cell wall and membrane that are both assumed to be in the liquid phase (Ho *et al.*, 2011). At that contact area, the gas and liquid concentrations of O_2 are equivalent according to Henry's law:

$$C_{O_2,l} = RTH_{O_2} C_{O_2,g} \tag{4.3}$$

with R (8.314 J mol^{-1} K^{-1}) the universal gas constant, T (K) the temperature and H_{O_2} (mol m^{-3} kPa^{-1}) Henry's constant for O_2. The indices l and g represent the liquid (cells) and gas (pores) phase. The interface flux, J_{O_2} (mol m^{-2} s^{-1}), was described as

$$J_{O_2} = P_{O_2,eff} \left(RTH_{O_2} C_{O_2,g} - C_{O_2,l} \right) \tag{4.4}$$

where $P_{O_2,eff}$ (m s^{-1}) is the effective permeability of membrane and cell wall that can be written as

$$P_{O_2,eff} = \frac{1}{\frac{L_w}{D_{O_2,w}} + \frac{L_m}{D_{O_2,m}}} \tag{4.5}$$

where $D_{O_2,w}$ and $D_{O_2,m}$ (m^2 s^{-1}) are the O_2 diffusivity of cell wall and cell membrane, respectively, while L_w and L_m are the thickness of those compartments. All model parameters are listed in Table 4.1.

Table 4.1. Physical parameters of the microscale gas transport model.

Constants	Value	Description
L_w	1.67×10^{-6} m (1)	Thickness of the cell wall
L_m	8.00×10^{-9} m (2)	Thickness of the cell membrane
$D_{O_2,w}$	9.90×10^{-10} m² s^{-1}	O_2 diffusivity of the cell wall
$D_{O_2,m}$	1.80×10^{-10} m² s^{-1} (3)	O_2 diffusivity of the cell membrane
R	8.3144 Pa m³ mol^{-1} K^{-1}	Universal gas constant
H_{O_2}	2.09×10^{-5} mol m^{-3} Pa^{-1} (4)	Henry constant for O_2
$D_{O_2,g}$	1.79×10^{-5} m² s^{-1} (5)	O_2 diffusivity in the gas phase (pore matrix)
$D_{O_2,l}$	9.90×10^{-10} m² s^{-1} (6)	O_2 diffusivity in the liquid phase (cell matrix)

(1) Mebatsion *et al*. (2009), (2) Gunning and Steer. (1996), (3) Uchida *et al*. (1992), (4) Sander. (2015), (5) Marrero and Mason. (1972), (6) Armstrong. (1979).

Two different O_2 concentrations of 30 % and 5 % were applied over the two opposite sides of the tissue geometry at the determined radial direction. The computation used the generalized minimum residual method in Matlab R2018b (The Mathworks, Natick, MA, USA) to produce a map of the O_2 distribution throughout the samples. The corresponding O_2 fluxes were then calculated in the direction of the applied concentrations. The effective O_2 diffusivity of the tissue was determined by Fick's law of diffusion in the determined direction of the 3D tissue geometry.

$$D_{O_2,eff} = -\frac{n_{O_2} L}{A \Delta C_{O_2,g}} \tag{4.6}$$

where n_{O_2} (mol s^{-1}) is the mass flow rate of O_2 in the flux direction, L (m) is the thickness of the tissue sample in the radial direction, A (m^2) is the tissue area perpendicular to the flux direction, and $\Delta C_{O_2,g}$ (mol m^{-3}) is the applied equilibrium gas concentration gradient in the radial direction.

4.2.6 Model of effective O_2 diffusivity

Different models were explored for the relation between the effective O_2 diffusivity and the tissue porosity and tortuosity. In order to generate a representative model for the effective O_2 diffusivity, the two main phases of plant tissue material, the liquid in cells and cell walls and gas in the intercellular spaces, were considered in the model. The cellular diffusivity of O_2 was approximated by the diffusivity of O_2 in water $D_{O_2,l}$ (m^2 s^{-1}) multiplied by its solubility $D_{O_2,l}RTH_{O_2}$, with R (J mol^{-1} K^{-1}) the universal gas constant, T (K) temperature and H_{O_2} (mol m^{-3} kPa^{-1}) Henry's constant for O_2 equilibrium between water and air.

First, a simple parallel model of effective O_2 diffusivity to total porosity, $D_{O_2,eff}$ (m^2 s^{-1}), was proposed based on Equation 2.8 and 2.9, assuming pore spaces running along the cells in the radial direction:

$$D_{O_2,eff} = \varepsilon^n D_{O_2,g} + (1-\varepsilon) D_{O_2,l} RTH_{O_2} \tag{4.7}$$

The first and second terms on the right side are the O_2 diffusivity in intercellular spaces and in the cells, respectively. ε is total tissue porosity and $D_{O_2,g}$ (m^2 s^{-1}) is the O_2 diffusivity in air; n is a model fitting parameter to account for pore geometry effects.

Second, a similar model for effective O_2 diffusivity was also explored with respect to open porosity only (ε_o):

$$D_{O_2,eff} = \varepsilon_o{}^n D_{O_2,g} + (1-\varepsilon_o) D_{O_2,l,eff} \tag{4.8}$$

where the effect of closed pores is incorporated in the value of $D_{O_2,l,eff}$ (m^2 s^{-1}). The effect of trapped pores (inclusions) on the mass diffusivity in materials

has been extensively studied and modeled. Here, the model of Maxwell-Garnett for 3D media that was reproduced by Kalnin *et al*. (2002) is used. It has been developed for a spherical inclusion inserted into a spherical shell of a host material (matrix), in which the inclusion concentration is assumed not to affect the concentration of the matrix. The model is valid for any space dimension and written as:

$$D_{O_2,l,eff} = D_{O_2,l} RTH_{O_2} \left(1 + \frac{3\left(D_{O_2,g} - D_{O_2,l} RTH_{O_2}\right)\varepsilon_{c,l}}{D_{O_2,g} + 2D_{O_2,l} RTH_{O_2} - \left(D_{O_2,g} - D_{O_2,l} RTH_{O_2}\right)\varepsilon_{c,l}} \right) \quad (4.9)$$

where $\varepsilon_{c,l}$ is the porosity of the tissue without the open pores, written as

$$\varepsilon_{c,l} = \frac{\varepsilon_c}{1-\varepsilon_o} \quad (4.10)$$

with ε_c is closed porosity. Third, the effect of tortuosity was investigated. Thereto, the following well-known relation of effective gas diffusivity in porous media, as described in Equation 2.10, was taken into account, thus omitting the fitting exponent$\left(n\right)$:

$$D_{O_2,eff} = \frac{\varepsilon}{\tau} D_{O_2,g} + (1-\varepsilon) D_{O_2,l} RTH_{O_2} \quad (4.11)$$

Again, a similar model was implemented for the correlation with open porosity:

$$D_{O_2,eff} = \frac{\varepsilon_o}{\tau} D_{O_2,g} + (1-\varepsilon_o) D_{O_2,l,eff} \quad (4.12)$$

The models in Equation 4.7-4.8 were statistically identified by fitting the model prediction to the simulated data for effective O_2 diffusivity in JMP Pro 14 (SAS Institute Inc., USA) to estimate the model fitting parameter n. For all models, the goodness of fit was analyzed at a 95 % confidence level. Confidence intervals were plotted around the model predictions.

In addition, a model of effective O_2 diffusivity directly based on grayscale value of the low resolution CT image of the tissue was analyzed (Supplementary A3). However, as the model parameters depend on the grayscale intensity affected by

different X-ray CT settings and systems, the model is not generally applicable. Hence, models incorporating physical parameters such as tissue porosity were more reliable.

4.2.7 Relation between open and total porosity

The CT-based porosity maps of Chapter 3 only provide estimates for the total porosity. As the effective O_2 diffusivity was assumed to also relate to open porosity, the relation between open and total porosity was explored to map open porosity. Such a relation might provide a means to enrich the data to implement Equations 4.8-4.12 for effective diffusivity mapping. The following relation was considered:

$$\varepsilon_o = a\varepsilon^b \tag{4.13}$$

where a and b are the model fitting parameters. The fitting was done on all the samples of the five apples or pear fruit using JMP Pro 14 software. The developed model was then tested by comparing the actual open porosity profile extracted from the high resolution CT images and the one predicted by the model.

4.2.8 Model Testing

The models were then tested on an individual sample of each species by comparing the predicted O_2 diffusivity profile calculated from the models, and the simulated O_2 diffusivity profile computed from consecutive high resolution micro CT scans for the radial tissue sample. The O_2 diffusivity profile was predicted from the low resolution image of the radial tissue initially translated into the total porosity profile, as described in Chapter 3 and further to the open porosity profile using Equation 4.13. The estimated total and open porosity profiles were then transformed into effective diffusivity profiles using Equation 4.7 and 4.8, respectively, which were compared to the reference values calculated from the high resolution CT scans for the same tissue. Additional analyses were performed by comparing O_2 concentration profiles computed

using the calculated and predicted O_2 diffusivity profiles for apple and pear samples.

4.2.9 Mapping effective O_2 diffusivity

The total porosity maps obtained in Chapter 3 were created using a moving VOI ($1.3\times1.3\times1.3$ mm^3) across the volume of the organ. The estimated porosity values were subsequently translated into estimates for the effective O_2 diffusivity using the developed formulas (4.1-4.4) in Matlab. Coronal (X-Z) slices of the 3D diffusivity map were visualized to exhibit the spatial O_2 diffusivity distribution in the entire organ. The image background (air) was set to be transparent.

4.3 Results

4.3.1 Profiles of to tal and open porosity, tortuosity and effective O_2 diffusivity

Representative 3D skeletonized pore networks captured from the middle part of the radial tissue showed considerable differences in the structure of the pore channel network among the species (Figure 4.2). Eggplant and turnip tissues consisted of small and convoluted pore networks (Figure 4.2A and B), while apple tissue was filled by bigger and less connected pore structures (Figure 4.2C). Compared to the other species, the pores of pear tissue were the smallest with locally unconnected pores, most likely caused by the stone cells (blank areas) that were surrounded by denser cell clusters (Figure 4.2D). This confirmed previous finding published by Verboven *et al*. (2008).

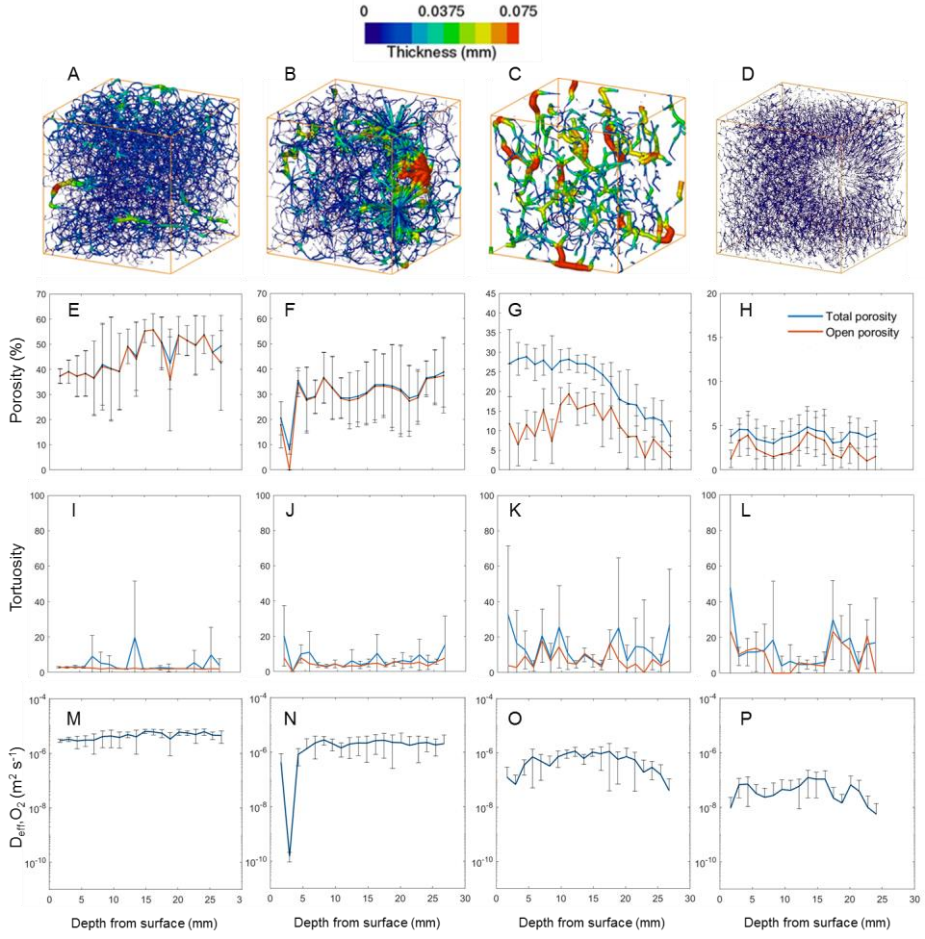

Figure 4.2. Representative skeletonized 3D pore networks, total- and open porosity, tortuosity and effective O_2 diffusivity profiles for (A, E, I, M) eggplant, (B, F, J, N) turnip, (C, G, K, O) apple and (D, H, L, P) pear. The color of the 3D pore network represents the local pore thickness in the tissues. The profiles were calculated from high resolution tissue images of five replicates. The vertical bars indicate standard deviations. Red line in the tortuosity graphs is the median value. The *x*-axis of the graphs represents the radial tissue depth (mm) from surface to center.

Differences in the pore structure along the radial axis of each considered species were also observed. Small differences between total and open porosity described well-connected or open pore structures. Open pore structures were evidenced for eggplant and turnip radial profiles, associated with high porosity (Figure 4.2E and F), with the ratio of total to open porosity nearly equal to 1. In the radial

profile of apple, the open porosity was considerably lower than the total porosity, and this was more pronounced for the first 10 mm below the fruit surface (Figure 4.2G). A mean total-open porosity difference in pear was also found. The porosity range was much smaller than for apple, with considerable overlap of the error bars of the two parameters (Figure 4.2H). Therefore, the ratio of total to open porosity was considerably greater than 1 for apple, while it was slightly larger than 1.

The tortuosity of the pore space varied largely with position and among the species. Large variability was also found across repetitions. Eggplant and turnip tissues showed less tortuous pore structures (Figure 4.2I and J). Apple and pear fruit had a higher tortuosity that fluctuated from outer to inner tissue positions, without clear profiles (Figure 4.2K and L).

The radial effective O_2 diffusivity in and among the four species is shown in Figure 4.2M, N, O and P. It was larger for eggplant and turnip compared to apple and pear. Lower effective O_2 diffusivities were concomitant with low tissue porosity at the same position (Figure 4.2M and N). High variation in the diffusivity profile among the same species was found in apple and pear fruit (Figure 4.2O and P). The diffusivity values were not only correlated to the total porosity, but appeared to be also affected by the open porosity and pore tortuosity. The dependence of the effective O_2 diffusivity on the total porosity, open porosity, and tortuosity was thus explored to identify the best formula for effective O_2 diffusivity mapping.

4.3.2 Effective O_2 diffusivity versus total porosity

The effective O_2 diffusivity ($m^2\ s^{-1}$) generally increased with the total porosity for the different plant species (Figure 4.3A). The lowest O_2 diffusivity value was the O_2 diffusivity of water at 0 % porosity ($4.69\times10^{-11}\ m^2\ s^{-1}$). The diffusivity exponentially increased with porosity to a maximum value equal to the O_2 diffusivity in air ($1.79\times10^{-5}\ m^2\ s^{-1}$), i.e., at 100 % porosity.

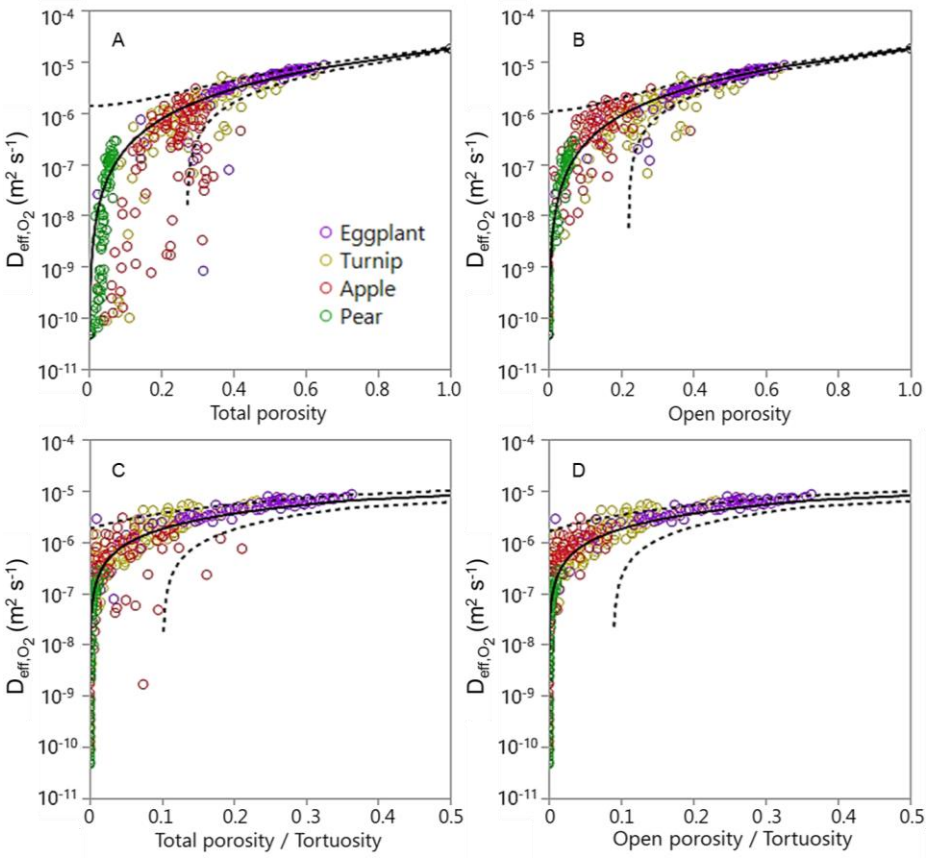

Figure 4.3. Scatter plots of effective O_2 diffusivity (m^2/s) versus (A) total porosity, (B) open porosity, (C) total porosity/tortuosity and (D) open porosity/tortuosity. The solid line indicates the model prediction for effective O_2 diffusivity. The dashed lines show the 95% confidence intervals. The *y*-axis is plotted on a logarithmic scale.

The effective O_2 diffusivity values for eggplant and turnip were mainly distributed in a similar range from 10^{-7} to 10^{-6} m^2 s^{-1}, with a total porosity ranging from 5 to 65 %. The effective diffusivity of apple fruit varied over a wider range, from 10^{-10} to 10^{-6} m^2 s^{-1}; the corresponding porosity range was 5 to 40 %. Pear fruit, with a porosity range of 0 to 10 %, had O_2 diffusivity values over a wide range of magnitudes (10^{-11}-10^{-7} m^2 s^{-1}). A considerable number of data points were scattered around the general exponential trend in Figure 4.3A. Small values for effective O_2 diffusivity were found for samples with relatively high total porosity values up to 40 % for all products except for pear fruit.

The simple serial model with respect to total porosity (Equation 4.7) was fitted to the data (Figure 4.3A), with an exponent n = 1.97±0.017, describing the majority of the data at the high end of diffusivity values for each porosity (R^2 = 0.92; RMSE = 6.90×10^{-7} m^2 s^{-1}) quite well. However, the magnitude of the errors for samples at the low porosity end of the range was considerable, with predictions that were generally higher than the measurements. The model was also not able to predict the low diffusivity values of some samples with high total porosity, particularly in the case of apple fruit.

4.3.3 Effective O_2 diffusivity versus open porosity

Fitting equation (4.8-4.10) to the effective O_2 diffusivity versus the open rather than the total porosity data improved the fit (R^2 = 0.95; RMSE = 5.41×10^{-7} m^2 s^{-1}; n = 1.87±0.013 (Figure 4.3B). The majority of the samples with low effective diffusivity at high total porosity now moved closer to the model prediction because their open porosity was much smaller than the total porosity. Also, for the lower end of the porosity and diffusivity range, the predicted values matched the measurements better. This improved fit indicates the importance of pore connectivity as a determinant for effective O_2 diffusivity in plant tissues. Once the pore channels are mostly closed in the direction of diffusion, the capability of the tissue to diffuse O_2 drops several orders of magnitude. The outliers that were still observed were most likely affected by other microstructural parameters, such as pore tortuosity, that were insufficiently described by the exponent n.

4.3.4 Effect of pore tortuosity on effective O_2 diffusivity

The effect of pore tortuosity on the effective O_2 diffusivity is shown in Figures 4.3C and D. On the x-axis of these graphs, the porosity to tortuosity ratio is now plotted. This resulted in a linear relation with the effective O_2 diffusivity distribution and helped to remove extreme outliers from the general trend. The model predictions with respect to total porosity (Equation 4.11) and open porosity (Equation 4.12) also fitted well to the data with R^2 = 0.89; RMSE =

9.21×10^{-7} m^2 s^{-1} and $R^2 = 0.93$; RMSE = 8.74×10^{-7} m^2 s^{-1}, respectively. However, the incorporation of pore tortuosity did not improve the fit of the model to the data compared to the model based on total porosity or open porosity alone.

4.3.5 Radial profile of the diffusivity based on total porosity

The observed O_2 diffusivity profile computed using high resolution images of radial tissue was compared to the diffusivity obtained from low resolution image of the same tissue (Figure 4.4). The low resolution tissue image was translated to total porosity using the fitted equation. The profiles revealed a considerable radial heterogeneity in effective O_2 diffusivity along the radial tissue and among the species.

The profiles predicted from total porosity (Equation 4.7) are discussed (Figure 4.4). A close agreement between the predicted and observed diffusivity profile was exhibited for eggplant; the average diffusivity was 4.44×10^{-6} m^2 s^{-1} and the RMSE of the predicted profile was equal to 1.15×10^{-6} m^2 s^{-1} (Figure 4.4A). Similar to eggplant, the predicted O_2 diffusivity profile of turnip agreed with the calculated O_2 diffusivity throughout the radial distance, with RMSE equal to 8.53×10^{-7} m^2 s^{-1} for an average diffusivity of 1.84×10^{-6} m^2 s^{-1}, except close to the surface (Figure 4.4B).

In apple, the predicted effective O_2 diffusivity diverged from the calculated value with RMSE = 7.50×10^{-7} m^2 s^{-1} for an average diffusivity of 5.60×10^{-7} m^2 s^{-1} (Figure 4.4C). Figure 4.4D shows the predicted versus measured diffusivity profile of pear with lower values than for the other species (RMSE = 7.52×10^{-8} m^2 s^{-1} for an average of 4.82×10^{-8} m^2 s^{-1}). The results showed that the total porosity-based model was reasonably accurate for eggplant and turnip, although not considering pore connectivity effects, but not for apple and pear.

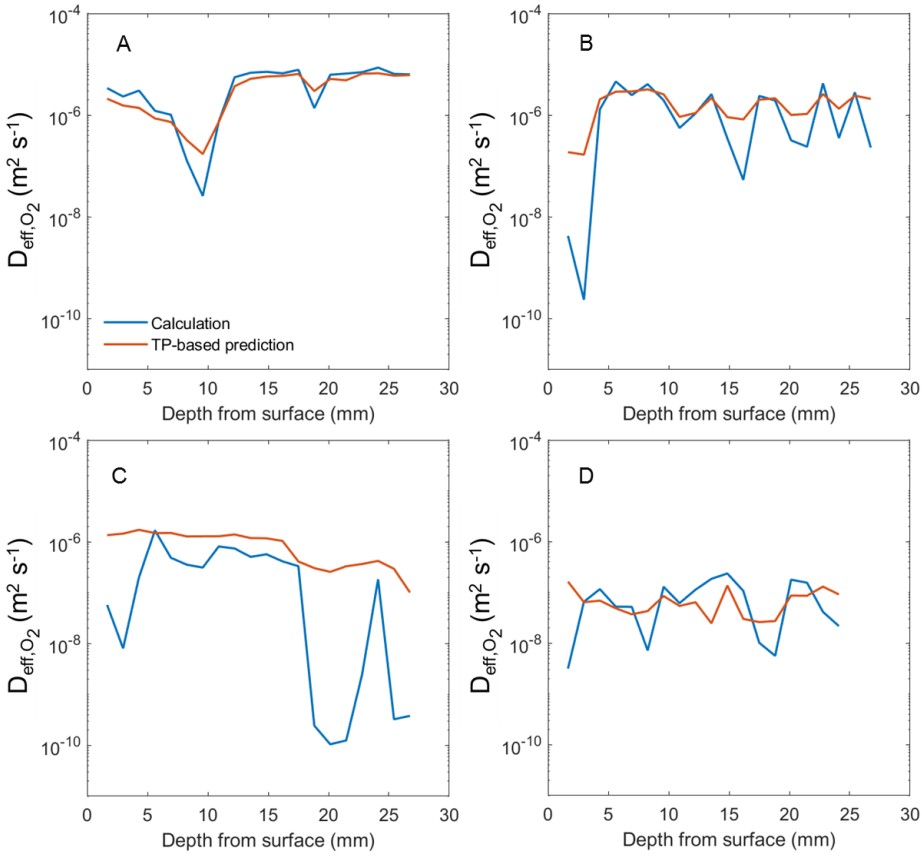

Figure 4.4. Effective O_2 diffusivity profiles of (A) eggplant, (B) turnip, (C) apple and (D) pear as a function of radial position in one of the samples. Predicted O_2 diffusivity (red line) was estimated based on the total porosity (TP) estimated from the greyscale levels in the low resolution radial sample image. Calculation of O_2 diffusivity (blue line) was based on the microscale model. The *x*-axis represents radial tissue depth (mm) from surface to center.

4.3.6 Open porosity prediction

As the predicted profiles using the total porosity-based model (Equation 4.7) did not agree well with the measured profiles for apple (Figure 4.4C) and pear (Figure 4.4D), we also evaluated the open porosity-based model (Equation 4.8-4.10) that predicted the O_2 diffusivity more accurately. However, the open porosity could not be calculated from low resolution CT scans. We, therefore, fitted an exponential model to relate open to total porosity for apple and pear

(Figure 4.5A and B); $\varepsilon_o = 0.03\varepsilon^{1.86}$ (RMSE = 5.76 %) for apple; $\varepsilon_o = 0.25\varepsilon^{1.66}$ (RMSE = 0.93 %) for pear. The predicted values for open porosity (previously translated from grayscale to total porosity) matched the actual open porosity along the radial direction quite well (Figure 4.5C and D). Since the actual total porosity and open porosity did not differ much for eggplant and turnip (Figure 4.2A, B, and Supplementary A2), we did not do this analysis for eggplant and turnip.

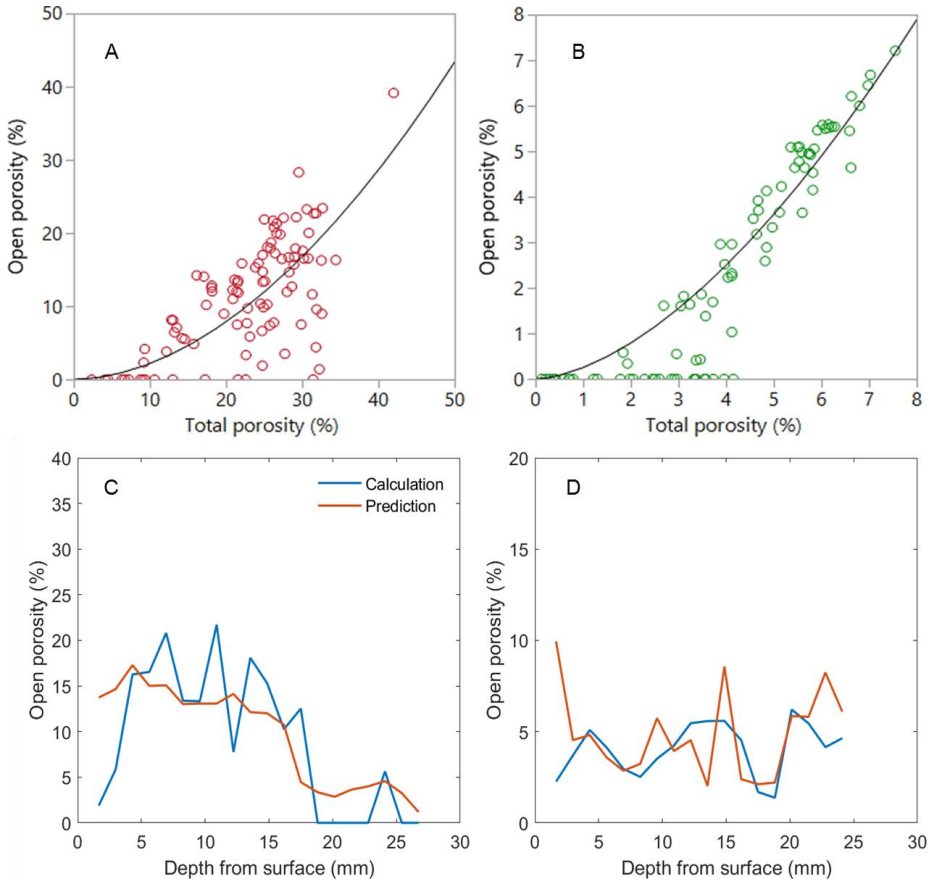

Figure 4.5. Procedure to estimate open porosity from total porosity. (A) and (B) regression plots between total and open porosity for apple and pear, respectively. (C) and (D) testing of the regression model as a function of radial position for an apple and pear sample, respectively. The prediction of the open porosity (red line) is based on a low resolution CT image of radial tissue while the calculation (blue line) is based on a high resolution CT image of the same tissue.

4.3.7 Radial profile of the diffusivity based on open porosity

The open porosity-based model of O_2 diffusivity was tested for apple and pear by employing Equation 4.8-4.10 (Figure 4.6). The effective O_2 diffusivity prediction with respect to the estimated open porosity improved considerably with an RMSE of 3.47×10^{-7} m^2 s^{-1} for apple (Figure 4.6A). For pear, the improvements were not so clear, most likely due to the use of a single general model for all products (RMSE = 8.85×10^{-7} m^2/s) (Figure 4.6B), compared to the diffusivity prediction calculated from total porosity (Figure 4.4D). The improvement was already expected from comparing Figure 4.3B to Figure 4.3A. This result indicates that a more advanced technique is required to estimate the diffusivity of plant products with a small porosity and a less open pore structure. The open porosity-based model did also not predict very low effective O_2 diffusivity values well.

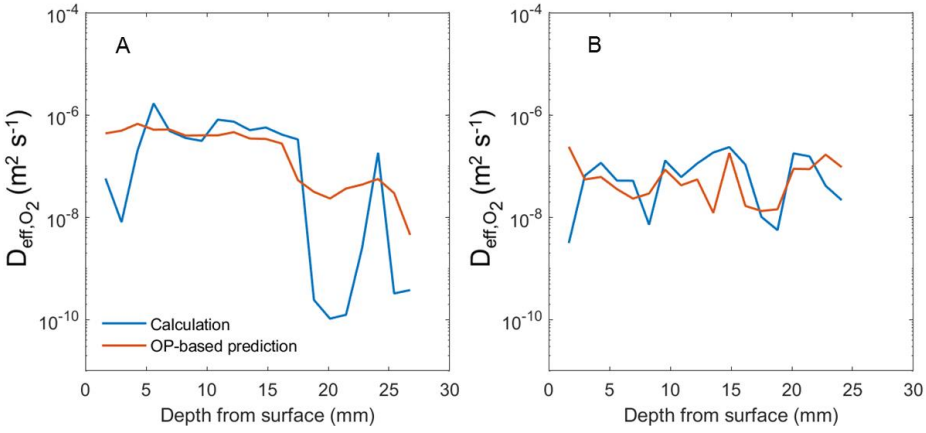

Figure 4.6. Effective O_2 diffusivity profiles of (A) apple and (B) pear as a function of radial position for one sample. Predicted O_2 diffusivity (red line) was computed with respect to estimated open porosity (OP) calculated from the total porosity map. The O_2 diffusivity (blue line) was calculated based on the microscale model. The *x*-axis represents radial tissue depth (mm) from surface to center.

The simulation result showed that for pear the O_2 concentration profile predicted using the open porosity-based diffusivity was in close agreement with the profile

predicted using the microscale model-based diffusivity (Supplementary A4). For apple, a large difference was found between the O_2 concentration profile based on the calculated diffusivity and the predicted diffusivities based on the open or total porosity.

4.3.8 Map of effective O_2 diffusivity

The O_2 diffusivity maps for the four products revealed a considerable variation within and in-between products (Figure 4.7). The O_2 diffusivity values for eggplant and turnip ranged from 10^{-7} to 10^{-6} m^2 s^{-1} (Figure 4.7A and B) with an average of $(3.61\pm0.06)\times10^{-6}$ m^2 s^{-1} and $(1.24\pm0.32)\times10^{-6}$ m^2 s^{-1}, respectively. The O_2 diffusivity range ($5\text{-}8\times10^{-6}$ m^2 s^{-1}) was particularly high in the endocarp (EDC) tissue of eggplant, while lower values ($2\text{-}4\times10^{-6}$ m^2 s^{-1}) were observed in the outer tissue (epicarp, EPC) (Figure 4.7A). The seeds clearly showed a lower O_2 diffusivity than the surrounding endocarp tissue. Another low diffusivity region was observed in the pedicel end (PE) tissue. In turnip, higher O_2 diffusivity values were observed in the storage region (SR) ($6\text{-}8\times10^{-6}$ m^2 s^{-1}) (Figure 4.7B). The denser cortex tissue (CTs) that was positioned in the outer tissue area had a low effective O_2 diffusivity.

The calculated effective O_2 diffusivities for apple fruit were very variable across a range from 10^{-10} to 10^{-6} m^2 s^{-1} with an average of $(4.37\pm0.72)\times10^{-7}$ m^2 s^{-1} (Figure 4.7C). O_2 diffusivity variation was observed across the cortex (CTs) and core regions (CR) of the apple fruit (Figure 4.7C). The O_2 diffusion coefficient calculated for the cortex was larger than that for the core region. Vascular bundles, that visibly spread out in the cortex tissue, and the stem end showed a lower O_2 diffusivity. Dense tissue in pear fruit corresponded to low O_2 diffusivity values (Figure 4.7D). The average effective O_2 diffusivity of pear was $(2.80\pm0.5)\times10^{-8}$ m^2 s^{-1}, across a larger range between 10^{-11} and 10^{-7} m^2 s^{-1}. Only slight O_2 diffusivity differences were exhibited between cortex (CTs) and core regions (CR). The maps of effective O_2 diffusivity confirmed that the apparent gas diffusivity could not be regarded as a homogeneous gas exchange parameter

in plant tissues. Different structural features of the tissue in each position inside the product resulted in different effective O_2 diffusivities.

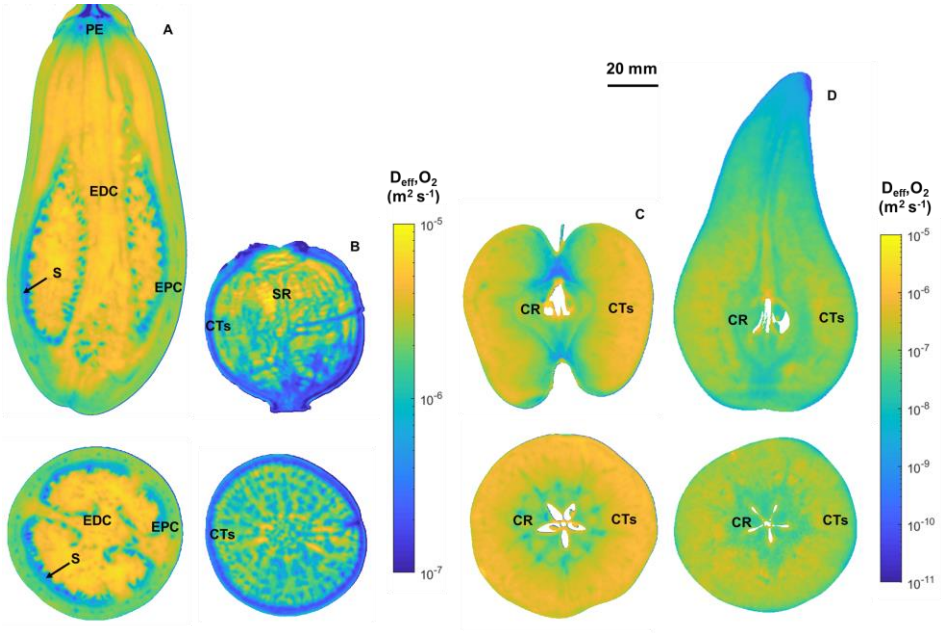

Figure 4.7. Coronal (X-Z) slice of 3D effective O_2 diffusivity map of (A) eggplant, (B) turnip, (C) apple and (D) pear. The map of eggplant and turnip were plotted using the same color scale and were computed based on the total porosity; the apple and pear maps both used the color scale at the right and were computed based on the open porosity map. Different tissue regions are indicated: endocarp (EDC), epicarp (EPC), pedicel end (PE), group of seeds (S), storage region (SR), core region (CR), and cortex tissue (CTs).

4.4 Discussion

The 3D pore networks in general show a considerable difference of the pore structure among the products at microscale (Figure 4.2). The network largely determines the effective diffusivity which is a function of tissue porosity, pore connectivity, and tortuosity, in addition to the diffusivity of oxygen in the gas and liquid phases of the materials. The mean porosity of the products is generally in agreement with the literature: 59.6±0.5 % for eggplant (Gras *et al*., 2002), 20.6±0.3 % for turnip (Lech *et al*., 2018), 25.4±2.6 % for apple and 5.7±1.4 % for pear (Herremans *et al*., 2015a). An exponential relationship between the O_2

diffusivity and the tissue porosity was found for a large range of porosity values (0 to 65 %) across different species (Figure 4.3). The fact that O_2 dominantly diffuses through the pore channels causes tissues with larger porosity to have higher effective O_2 diffusivity, as also described by Ho *et al*. (2010b) and Herremans *et al*. (2015a). However, the pore connectivity and tortuosity of the four products also contributed in different ways to the effective O_2 diffusivity (Figure 4.3). These physical features of the porous tissue microstructure affect gas transport. While this has been suggested earlier (Verboven *et al*., 2008; Herremans *et al*., 2014a), their effect has been quantified for the first time in this work.

We found that the effect of pore connectivity of bulky plant tissues is incorporated into the feature of open porosity (Figure 4.2E, F, G and H), which is a measure for the number of continuous routes that are available for O_2 to diffuse across the radius of the product. A large total porosity to open porosity ratio indicates a low connectivity of the pores in the tissue. For eggplant and turnip the ratio was nearly 1, indicating a well-connected pore space in these products. This was concomitant to the low pore connectivity of 'Jonagold' apple tissue found in earlier studies (Verboven *et al*., 2008; Herremans *et al*., 2015a,b). In 'Conference' pear, that in general has a well-connected pore space, the fraction of unconnected pores is most likely due to brachysclereids (stone cells) that are present in the pear cortex tissue and cause highly deformed cells and pore spaces (Verboven *et al*., 2008).

The lesser connected pore network of apple most likely contributed to a large extent to the outliers for the model that described the O_2 diffusivity as a function of the total porosity (Figure 4.3A). Ho *et al*. (2011) hypothesized that the high diffusivity of O_2 in gaseous pore space combined with the low solubility of O_2 in the liquid phase (cells) makes the pore space the main route for O_2 diffusion. Therefore, unconnected pore structures of tissue may hinder the passage of O_2 and result in a decrease of the O_2 diffusivities, even when the total porosity is

large. Consequently, the effective O_2 diffusivity can vary between samples with identical total porosity, depending on the pore connectivity.

The connectivity of the pore structure may be more critical than the size and number of pores in the mechanism of gas transport (Vogel, 2002). Here, the effective O_2 diffusivity correlated better with the open porosity (Figure 4.3B), emphasizing the critical role of the pore connectivity of tissue. The rather wide range of O_2 diffusivity values observed at identical open porosity values is most likely caused by differences in the tortuous structure of the pores (Figure 4.3B).

The spatial arrangement of the cell matrix in parenchyma tissue contributes in different ways to the tortuosity of the O_2 diffusion path. As a result, gas transport rates through a more tortuous tissue are lower than the rates through tissue with less tortuous pores at similar porosities. The tortuosity parameter describes the complexity of the pore micro-architecture of porous media (Al-raoush and Madhoun, 2017; Li *et al*., 2018).

In this study, the effective O_2 diffusivity correlated well with the ratio of porosity and tortuosity over the whole scale of magnitudes (Figure 4.3C). Again, in combination with the tortuosity, the open porosity predicted the effective O_2 diffusivity better than the total porosity (Figure 4.3D), demonstrating the importance of the open porosity. However, incorporating the tortuosity in the models did not improve the correspondence between the O_2 diffusivity values estimated from the low resolution CT images and those calculated from the high resolution CT images appreciably. There was still some scattering on the diffusivity as a function of the ratio of total- or open porosity to tortuosity, in the regular scale of the *y*-axis. As the actual pore length used to compute the tortuosity is an average of many pore channels, the gas diffusion traveling into porous tissues may vary, depending on complexity of individual pore channels, even though the pore tortuosity of the tissues is similar.

Other models that express diffusivity as a function of tortuosity were reported by Currie (1960), who theoretically developed a physics-based model for a simple

porous geometry where the tortuosity was raised to an exponent of 2: $D_{eff} = D_g \, \varepsilon / \tau^2$. However, this formula model did not result in a better prediction of the diffusivity from the porosity and tortuosity (data not shown). Troeh and Jabro (1982) suggested that it is necessary to empirically adapt the ratio D_{eff} / D_g to structural parameters of the material for complex porous materials. Moreover, a method to quantify the variability in pore tortuosity in an intact fruit or vegetable is not available yet.

The models for effective O_2 diffusivity calculation from the high resolution CT images used in this study are based on the properties of the two main phases of the fruit or vegetable tissue: the intracellular liquid phase (consisting of cells, membranes and cell walls) and intercellular gas phase (pore spaces) making no distinction between cell wall and cell diffusivity (Ho *et al*., 2006b). Such differences can be incorporated by extending the model to a multi-phase model for effective diffusivity. Silva *et al*. (2000) suggested that structural and physical properties of each component need to be well known to build a proper model.

Profiles of effective O_2 diffusivity in radial samples of the different organs were predicted with the different models and compared to reference data obtained from the high resolution CT images (Figure 4.4. and 4.6). The total porosity-based model generally produced a weak agreement between the predicted and calculated diffusivity profiles for apple and pear fruit, while the open pore structures of eggplant and turnip resulted in a better fit. Mapping of O_2 diffusivity based on total porosity is, therefore, sufficient for samples with high pore connectivity, but not for samples with lower pore connectivity.

As an alternative, the effective O_2 diffusivity was mapped using the open porosity-based model for apple and pear tissues with less connected pores (Figure 4.2G and H). As a direct computation from low resolution is not possible, an open porosity map was created using the exponential model (Equation 4.13). From the radial profile, a better fit between the predicted and calculated diffusivities was observed even though very low diffusivities at certain positions were not predicted accurately (Figure 4.6). We found that the total porosity is

not a good predictor of open porosity for samples with many unconnected pore structures such as 'Jonagold' apple. It resulted in a poor open-total porosity regression model, leading to wrong predictions of diffusivity in some regions. Hence, pear sample that showed a close agreement between O_2 concentration predicted using the microscale model-based diffusivity and open porosity-based diffusivity (Supplementary A4) was further used for the gas exchange study in Chapter 5. For eggplant and turnip, the open porosity-based model was not needed as the total porosity closely matched the open porosity (see Supplementary A4).

The 3D maps revealed a large heterogeneity in the effective O_2 diffusivity among and within the considered products (Figure 4.7). The different spatial arrangement of cells in each plant tissue introduced complex diffusion channels for oxygen, resulting in a heterogeneous effective diffusivity. A large distribution of the O_2 diffusivity of eggplant and turnip was mainly due to their large porosity, and to a lesser extent also the smaller tortuosity and open pore structure along the radial eggplant and turnip tissues that facilitated O_2 diffusion through the intercellular space. Therefore, the O_2 diffusivity at each tissue position inside the eggplant and turnip samples corresponded to that of the porosity. Two tissue layers of eggplant, the epicarp (EPC) in the outer zone and the endocarp (EDC) in the inner area, are composed of interconnected and tubular cells forming high porous tissue in the inner part and round cells with a small fraction of pores in the outer part, respectively (Puig *et al*., 2012). In turnip, the high diffusivity area was centered in the storage region (SR) that consists of a root vascular system with a high void fraction. The low diffusivity region in the outer region was caused by the denser tissue area. Liu *et al*. (2019) explained that the fast secondary growth of turnip hypocotyl-tubers forms its heterogeneous structure.

In 'Jonagold' apple, a heterogeneous O_2 diffusion coefficient was also observed. The diffusivity radially decreased from the cortex tissue (CTs) to the core region (CR), confirming the variation of effective O_2 diffusivity observed in the radial

direction of apple tissues (Ho *et al*., 2010b). The vascular bundles appeared as low O_2 diffusivity zones because of the relatively thick water-filled vessels of the vascular system and the surrounding dense parenchyma tissue (Herremans *et al*., 2015b). The smaller void volume fraction and the less connected pore channel resulted in a smaller O_2 diffusivity compared to eggplant and turnip. Finally, because of their low porosity, the effective O_2 diffusivity in pear was the lowest of all products. The O_2 diffusivity variation along the radial tissue was previously observed by Schotsmans *et al.* (2003).

The map of effective O_2 diffusivity in an intact fruit or vegetable is now ready to be applied as a gas transport parameter to predict O_2 concentration inside the product and reveal the effect of the variability on gas concentration profiles, as further discussed in Chapter 5. For future research, the mapping method of diffusivity will need to be extended to map the effective diffusivity of other relevant gaseous metabolites that are involved in respiration or fermentation processes such as ethanol, acetaldehyde and ethyl acetate.

4.5 Conclusions

The spatial distribution of the effective O_2 diffusivity distribution contributes to understanding O_2 transport since calculations of gas concentration inside fruit or vegetables have been so far accomplished assuming a homogeneous O_2 diffusivity throughout the product (Ho *et al*., 2011; Herremans *et al*., 2014a). In this chapter, we have shown that X-ray computed tomography (CT) can be used to map the effective O_2 diffusivity in entire bulky plant organs. The consists of the following steps: (1) grayscale CT images of an intact product are converted into total porosity maps as outlined in Chapter 3; (2) the total porosity map is then converted into an effective O_2 diffusivity map using the total porosity-based model. These steps are sufficient for products with high pore connectivity such as eggplant and turnip. For products with low pore connectivity, extra steps such as mapping of the open porosity need to be performed. This can be achieved by

modeling the open porosity based on total porosity, although such relationship may not be very accurate for some products.

In Chapter 5, the effective O_2 diffusivity maps will be used as an input for respiratory gas transport simulations to compute the O_2 concentration profiles inside the product. The proposed approach could also be extended to map the effective diffusivity of CO_2 and other respiratory metabolites for studying respiratory gas transport in fruit and vegetables during controlled or modified atmosphere storage.

Chapter 5

Gas exchange model using effective diffusivity map to study internal browning in 'Conference' pear

5.1 Introduction

Under (D)CA, reduced O_2 and slightly elevated CO_2 partial pressures, in combination with a low temperature, slow down respiration process of pear and prolong its storage life (Brady and Romani, 1988). At very low O_2 partial pressure, the diffusion resistance of fruit skin and tissue increases the possibility of hypoxic or even anoxic conditions inside the pear, which gradually shifts the central metabolism to a fermentation-dominated process and leads to the symptoms of internal browning and cavity formation in the pear tissue (Lammertyn *et al*., 2003c,d; Franck *et al*., 2007). Gas partial pressures of the regular CA are, therefore, modified to be above the critical O_2 level or anaerobic compensation point (ACP) to avoid fermentation. Dynamic CA allows the modified gas levels to be closer to the ACP as it is naturally controlled by a biological signal of the fruit, indicating relatively high fermentation rates. Bessemans *et al*. (2016) used the respiratory quotient (RQ) as the indicator, which is calculated as the ratio of CO_2 production to O_2 consumption rates, dynamically measured at the storage atmosphere. In fermentation, this ratio drastically increases to a value much larger than 1.

Since invasive measurement of internal gas concentrations and rates in tissues is practically difficult, models that predict the internal gas concentration gradients inside pear fruit are helpful to unravel the process and improve our understanding of the influential parameters. Bessemans *et al*. (2020) developed a lumped three-compartment model to describe the rate of O_2 consumption and CO_2 production and RQ in the cellular level, which basically assumed permeability of pear skin, on the one side, and that of the cell, on the other, as the primary resistances of respiratory gas exchange, ignoring the resistance caused by the porous network

of intercellular gas spaces. Still, they found a difference between the actual RQ levels of cells in the pear fruit and the one calculated from the gas concentration changes in the storage atmosphere. This implies that the external RQ measurement that is used as a biological safety signal for the DCA algorithm may underestimate the actual RQ inside the fruit, which may have increased drastically as a consequence of its diffusion resistance.

A comprehensive multiscale gas exchange model was developed by Ho *et al*. (2011; 2013b) to predict O_2 and CO_2 concentration gradients in intact apple. The multiscale approach computes tissue gas-transport properties, such as the effective O_2 and CO_2 diffusivities, with a microscale gas transport model that incorporates the detailed microscale geometry of the tissue and integrates the corresponding processes to predict the internal gas profiles using a gas exchange model operated at the macroscale level of a whole fruit. However, a comprehensive computation of the gas exchange incorporating space-dependent properties has not been achieved to date. However, significant efforts have been conducted to predict and map the spatial distribution of tissue porosity across a fruit using non-destructive imaging methods such as X-ray computed tomography (CT) (Chapter 3) or magnetic resonance imaging (Musse *et al*., 2010; Winisdorffer *et al*., 2015). In a further step, the X-ray CT-based method of porosity mapping developed in Chapter 3 was successfully extended to predict effective O_2 diffusivity distribution as reported in Chapter 4.

This chapter aims to implement a heterogeneous model for respiratory gas exchange in pear fruit (*Pyrus Communis* L. cv. Conference) using 3D effective diffusivity maps. Simulation will be compared with predictions obtained with the gas exchange model using a uniform diffusivity to evaluate the effect of the diffusivity map-based model on local respiration and fermentation rates. The prediction results for O_2 and CO_2 concentrations and the corresponding RQ values inside the pear will be linked to the incidence of internal browning in pears after browning-inducing CA storage.

5.2 Materials and methods

5.2.1 Pear fruit

Late harvested 'Conference' pears (*Pyrus communis* L. cv. Conference) were picked on 9th of September 2019, in a commercial orchard in Kortenaken, Belgium (50°53'07.0"N 5°01'34.0"E). Late picked pears were used to increase the susceptibility to browning development, as reported by Lammertyn *et al*. (2000) and Ho *et al*. (2016). Four fruit were immediately scanned using X-ray CT to obtain a shape and porosity map of the intact fruit. The scanned fruit were then stored in a browning-inducing condition (1 kPa O_2; 0.7 kPa CO_2 at 1 °C) without a pre-cooling period in the pilot facility of the Flanders Centre of Postharvest Technology (Leuven, Belgium). The other 30 fruit were directly stored under the same conditions for intermediate internal browning checks every two months. After 4 months of storage, the O_2 concentration was lowered to 0.5 kPa, because no browning incidence was yet observed. Internal browning eventually was observed after 8 months of storage. The 4 test pears were scanned again using the same setting of the X-ray CT to obtain the porosity maps of browning-affected pears. The scanned pears were cut into 5 mm thick cross-sectional slices and photographed to visualize the incidence of internal browning.

5.2.2 X-ray CT scans and 3D pear geometry construction

The pear samples were scanned at low resolution (86 µm isotropic voxel size) using the in-house developed X-ray CT scanner HECTOR of the Ghent University Centre for Tomography (UGCT) (Masschaele *et al*., 2013). As this resolution was coarser than the size of cells and pores, the CT image of intact pear tissue would consist of grayscale intensities that corresponded to the heterogeneity of the internal tissue density, dependent on tissue porosity, due to the partial volume effect. Using the tube settings of 120 kV and 20 W target power (180 µA tube current), the effect of the focal spot on the spatial resolution was negligible. Covering a rotation of 360°, 1800 projection images at an exposure time of 666 ms each were acquired. The projection data were

reconstructed into 3D volumes using the Octopus reconstruction software (Octopus Imaging Software. Ghent, Belgium). Filtered pear juice in a small tube was scanned along with an entire pear as a zero porosity reference for tissue porosity mapping as described in Chapter 3.

For image processing, the reconstructed CT images were then imported in Avizo Fire Edition 2019.3 (VSG, Bordeaux, France). The CT images of the same pear fruit were aligned to one another using the image registration module in Avizo. The pear volume and its background (air) were then segmented using Otsu's thresholding to produce binary mask images. Small water phantoms scanned along with the sample and tape were then removed manually. Some tiny spots not recognized as tissue during mask binarization were closed by a filling operation to include them in the pear volume. For the affected pears, the cavities were sufficiently segmented by means of Otsu's thresholding as they had similar intensities to the background. Masking of the original grayscale CT image was performed to clean away materials such as tape and Styrofoam in the background. The stacks of the cleaned CT images were then imported in Matlab 19.a (The Mathworks, Inc., Natick, MA) for mapping of porosity and effective diffusivity.

The real 3D shape of pear was created from the binary image using a 'generate surface' module in Avizo and exported as an STL-file. Detailed air fractions in the middle of the pear (core) were removed to simplify pear geometry, as these features will be represented by the porosity map. In the next step, a surface mesh was created in ICEM CFD 19.2 (ANSYS Inc., Canonsburg, PA, USA) and then imported in COMSOL Multiphysics 5.5 (COMSOL Inc., Stockholm, Sweden). The surface meshes were then transformed into a volume finite element mesh for the respiratory gas transport simulations.

5.2.3 Regression model linking the effective O_2 and CO_2 diffusivities

Mapping of the effective O_2 diffusivity was performed using the procedures outlined in Chapter 4. The effective CO_2 diffusivity is also a model parameter. It

was mapped using a regression model describing the effective CO_2 diffusivity as a function of the O_2 diffusivity (Figure 5.1) computed previously using a microscale model (Ho *et al.*, 2016). The regression model was, for the first time, built and shown in this study. They found that the CO_2 diffusivity increased linearly with increasing O_2 diffusivity, with generally higher values because of higher solubility of CO_2 in the liquid phase. The resulting linear regression model was expressed as:

$$D_{CO_2,eff} = aD_{O_2,eff} + b \tag{5.1}$$

where $D_{CO_2,eff}$ and $D_{O_2,eff}$ ($m^2\ s^{-1}$) are the effective diffusivities of CO_2 and O_2, respectively, and a (0.87) and b ($9.61\times10^{-9}\ m^2\ s^{-1}$) are respectively the slope and intercept values. This equation fitted the data very well with an R^2 = 0.97 and RMSE = $5.51\times10^{-10}\ m^2\ s^{-1}$.

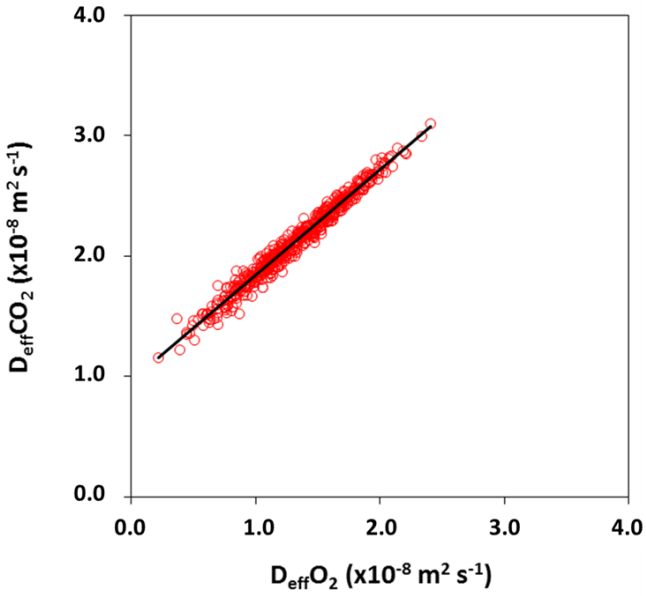

Figure 5.1. Linear correlation between effective O_2 diffusivity and effective CO_2 diffusivity computed by Ho *et al*. (2016).

5.2.4 Mapping of effective O_2 and CO_2 diffusivities

In Matlab, the grayscale values of the CT images were initially translated into a total porosity map using the mapping technique developed in Chapter 3. Subsequently, the (total) porosity maps were translated into effective O_2 diffusivity maps using the regression model between open and total porosity and that between open porosity and O_2 diffusivity (Equation 4.8-4.10) elaborated in Chapter 4. The affected pears consisted of damaged and sound tissue. Not unexpectedly, the total porosity of the damaged tissue was higher than that of the sound tissue (> 8%). In this case, the effective O_2 diffusivity was predicted using the total porosity-based model (Equation 4.8). Finally, the map of the effective CO_2 diffusivity was constructed using Equation 5.1. Transaxial (X-Y) and coronal (Y-Z) slices of the maps were visualized to exhibit the spatial distribution in the entire fruit; the O_2 and CO_2 diffusivity of the image background (air) was set equal to that of O_2 and CO_2 in air. Radial profiles of porosity, O_2 and CO_2 diffusivity were plotted for each sample and condition.

5.2.5 Internal browning segmentation

The tissue areas in the pears subjected to physiological disorder inducing conditions were classified into three types: sound tissue, brown tissue and cavity. The brown tissue and cavity together form the total affected tissue. The cavity, the air fraction, could be simply segmented from the original CT images as its contrast was excellent. However, due to insufficient contrast between the browning and sound tissue area, segmentation of the browning tissue volume was performed by mapping the relative difference between the calculated porosity of the affected pear and the calculated porosity for the healthy pear.

From the map, a high value of the relative difference indicates large tissue changes, which can be segmented as the total affected tissue. The threshold value was selected such that the percentage of the brown area obtained after segmentation corresponded most to that of the affected tissue area in the photograph. Both areas were statistically compared by means of a t-test at a

significance level of 5 %. The brown tissue was then the difference between the total affected tissue and cavity. The volume of the intact pear and its tissue area was calculated and visualized.

5.2.6 Respiratory gas exchange model for intact fruit

A reaction-diffusion model (Equation 2.1) was used to solve the overall gas exchange in intact fruit for the applied external gas conditions. The influence of permeation was initially tested using the regular gas exchange model (Ho *et al*., 2011) and was found insignificant to the predicted O_2 concentration in the specific low temperature and low O_2 concentrations of this study (Supplementary material B1). Furthermore, a mapping method for the permeation coefficient and nitrogen (N_2) diffusivity is not yet available to be integrated to the gas exchange model, along with O_2 and CO_2 diffusivity maps. Therefore, the model was written as:

$$\alpha_i \frac{\partial C_i}{\partial t} = \nabla \cdot D_{i,eff} \nabla C_i + R_i \tag{5.2}$$

with α_i the tissue gas capacity of O_2 or CO_2, C_i (µmol m^{-3}) concentration of O_2 or CO_2, t (s) time, $D_{i,eff}$ (m^2 s^{-1}) apparent diffusivity, R_i (mol m^{-3} s^{-1}) consumption and production terms of O_2 and CO_2, respectively, and ∇ (m^{-1}) the gradient operator. The gas capacity α_i is described as (Ho *et al*., 2006b; 2011):

$$\alpha_i = \varepsilon + (1-\varepsilon) RTH_i = \frac{C_{i,tissue}}{C_{i,g}} \tag{5.3}$$

where ε is the fractional porosity of tissue and $C_{i,g}$ (µmol m^{-3}) and $C_{i,tissue}$ (µmol m^{-3}) are the gas concentration of i in the gas phase and tissue, respectively. The concentration of gas molecule in the liquid phase of the tissue follows Henry's law represented by the constant H_i (mol m^{-3} Pa^{-1}) with R (J mol^{-1} K^{-1}) and T (K) as the universal gas constant and temperature, respectively.

A non-competitive inhibition model (Peppelenbos and Leven, 1996a; Hertog *et al*., 1998; Lammertyn *et al*., 2001; Ho *et al*., 2011) was used to calculate the O_2 consumption by respiration:

$$R_{O_2} = -\frac{V_{m,O_2} C_{O_2}}{\left(K_{m,O_2} + C_{O_2}\right)\left(1 + \frac{C_{CO_2}}{K_{mn,CO_2}}\right)} \tag{5.4}$$

with V_{m,O_2} (mol m^{-3} s^{-1}) the maximum oxygen consumption rate, C_{O_2} (mol m^{-3}) the O_2 concentration, K_{m,O_2} (mol m^{-3}) the Michaelis-Menten constant for O_2 consumption, K_{mn,CO_2} (mol m^{-3}) the Michaelis-Menten constant for non-competitive CO_2 inhibition, and R_{O_2} (mol m^{-3} s^{-1}) the O_2 consumption rate of the sample.

The production rate of CO_2 that consists of an oxidative respiration part and a fermentative part can be described as follow (Peppelenbos *et al*., 1996b):

$$R_{CO_2} = -r_{q,ox} R_{O_2} + \frac{V_{m,f,CO_2}}{\left(1 + \frac{C_{O_2}}{K_{m,f,O_2}}\right)} \tag{5.5}$$

with V_{m,f,CO_2} (mol m^{-3} s^{-1}) the maximal fermentative CO_2 production rate of the tissue, (mol m^{-3}), K_{m,f,O_2} (mol m^{-3}) the Michaelis-Menten constant for the inhibition of O_2 on fermentative CO_2 production, $r_{q,ox}$ the respiration quotient at high O_2 concentrations and R_{CO_2} (mol m^{-3} s^{-1}) the O_2 production rate of the sample.

The following boundary condition is implemented at the surface of the fruit:

$$-D_i \frac{\partial C_i}{\partial n} = h_i (C_i - C_{i,\infty}) \tag{5.6}$$

with n the outward normal to the surface; the index ∞ referring to the gas concentration of the ambient atmosphere; and h_i (m s^{-1}) the skin permeability for gas i (m s^{-1}). The permeability of the pear skin was calculated by Ho *et al.* (2018). The model parameters are listed in Table 5.1.

Table 5.1. Parameters of the respiration diffusion model for 'Conference' pears

Constants	O_2	CO_2	Description
$D_{i,eff}$	O_2 diffusivity map (1)	CO_2 diffusivity map (1)	Effective diffusivity
h_i	6.74×10^{-6} m s^{-1} (2)	10.2×10^{-7} m s^{-1} (2)	Skin permeability
K_{m,O_2}	0.17 kPa (3)		Michaelis-Menten constant for O_2 consumption
K_{mn,CO_2}		66.4 kPa (4)	Michaelis-Menten constant for non-competitive CO_2 inhibition
K_{m,f,O_2}		0.024 kPa (3)	Michaelis-Menten constant of O_2 inhibition on fermentative CO_2 production
V_{m,O_2}	2.23×10^{-5} mol m^{-3} s^{-1} (2)		Maximum O_2 consumption of late picked pear at 0 °C
V_{m,f,CO_2}		1.90×10^{-5} mol m^{-3} s^{-1} (2)	Maximum CO_2 fermentative production rate of late picked pear at 0 °C
rq_{ox}		0.77 (2)	Respiratory quotient at high O_2 partial pressure
$E_{a,V_{m,O_2}}$	73 kJ mol^{-1} (4)		Activation energy of O_2 consumption
$E_{a,V_{m,f,CO_2}}$		58.5 kJ mol^{-1} (4)	Activation energy of CO_2 consumption

(1) obtained from the diffusivity map procedure of four pears; (2) Ho *et al*. (2018); (3) Ho *et al*. (2013b); (4) Ho *et al*. (2008).

The maximal respiration rate of O_2 consumption, V_{m,O_2}, and CO_2 production, V_{m,f,CO_2} are known to be influenced by harvest date: late-harvested pear fruit typically have a higher maximal respiration rate than early- or optimal-harvested pear (Ho *et al*., 2016). The respiration kinetics of late-picked pears estimated by Ho *et al*. (2016) are, therefore, considered appropriate for the late-picked pears used in this study.

5.2.7 Gas exchange simulation using effective diffusivity maps

The diffusivity maps were firstly resized to increase computational efficiency by binning 10 voxels by means of a linear interpolation procedure in Matlab. This allowed to speed up the simulation process without affecting the results significantly (Supplementary materials B2). The binned map of the diffusivity was then uploaded to Comsol multiphysics 5.5. The lower and upper limits of the physical x-y-z coordinates of the map were set as input arguments. The diffusivity maps were then integrated into STL loaded geometry in which the macroscale gas exchange model was solved using the finite element method. The equations that were discretized over the mesh automatically computed the corresponding effective diffusivity values at every tissue position in the pear using a built-in interpolation function. As a comparison, gas exchange simulations using a single compartment uniform diffusivity for O_2 and CO_2 were performed. The uniform diffusivity was an average of the values in the entire map. Since the simulation was performed at 1 ^oC (the storage condition), the effect of temperature on the maximal respiration rate (V_{m,O_2} and V_{m,f,CO_2}) was estimated using Arrhenius' equation as proposed by Ho *et al*. (2010; 2018).

5.2.8 Critical oxygen level

The incidence of internal browning after storage was assumed to be associated with hypoxic conditions that could be predicted by the gas transport model and corresponding RQ values inside the pear. When the internal O_2 concentration drops below a threshold, fermentation is more prominent than aerobic respiration (Gran and Beaudry, 1993; Ho *et al*., 2013b; 2016). This condition has been

suggested as a trigger of internal browning (Ho *et al.*, 2016). Different approaches to estimate the low O_2 limit have been proposed. Ho et al. (2013b) estimated the critical limit based on energy supply criteria where the ATP production rate by aerobic respiration is equal to the maximum ATP production by fermentation. The critical O_2 level $C^*_{O_2}$ (kPa) is then described as follows:

$$C^*_{O_2} = \frac{f_f V_{m,f,CO_2} K_{m,O_2}}{f_o V_{m,O_2} r_{q,ox} - f_f V_{m,f,CO_2}} \tag{5.7}$$

where f_o and f_f are the stoichiometric coefficients of the ATP production due to oxidative respiration and fermentation, respectively. In aerobic respiration, one glucose molecule generally produces 38 ATP molecules and 6 CO_2 molecules, so that f_o is 38/6 = 6.33. In fermentation, one glucose molecule produces 2 ATP molecules and 2 molecules of CO_2, so that f_f is 2/2 = 1. The lowest predicted O_2 level inside the fruit was then compared to the $C^*_{O_2}$ (kPa).

Another method is based on the increase in the respiratory quotient (*RQ*) resulting from a drop in the O_2 concentration (Beaudry, 1993; Gran and Beaudry, 1993; Saenmuang et al., 2012). In this study, internal RQ was calculated and mapped by using the respiration models (Equation 5.4 and 5.5) with the predicted O_2 and CO_2 concentrations inside the pear as input, *i.e.*:

$$RQ = \frac{R_{CO_2}}{R_{O_2}} \tag{5.8}$$

where RQ represents the respiratory quotient of the tissue.

RQ exponentially increases below the lower O_2 limit. In this study, the RQ limit RQ^* was calculated by substituting $C^*_{O_2}$ (kPa) into the respiration rate model for O_2 and CO_2 (Equation 5.4 and 5.5), so that RQ^* was calculated. In this way, the relatively small inhibition effect of the CO_2 concentration (Equation 5.4) was ignored.

From the internal RQ and O_2 concentration predictions, RQ values along the radial axis of the pear were plotted against O_2 concentrations at the same location to visualize the change of internal RQ as a function of the internal O_2 level.

5.3 Results

5.3.1 Incidence of internal breakdown after storage

Development of internal browning was observed after 8 months of storage as described in the 3D visualization of the pear fruit after segmentation (Figure 5.2A, B, C and D). The distribution and shape of the affected tissue varied spatially within and among pear fruit; the symptoms even extended to the neck part for pear 2. The cavities that developed after browning occurred locally with varying volumes throughout the pear. Only tissue close to the skin remained unaffected.

Figure 5.2E, F, G and H represent vertical and horizontal slices from grayscale CT image of the pears. The horizontal slices were approximately taken from the largest cross-sectional area of the pear. The darker areas in the cortex tissue are assigned as browning-affected tissues (i.e., zones with lower porosity), while the black pixels specifically indicate cavities (the highest porosity). Compared to the CT images, the corresponding slices of the pear photographs exhibited the affected tissue region which also occupied the core region (Figure 5.2I, K and L), except for pear 2 (Figure 5.2J). Furthermore, the cavities were less visible in the pear photographs. The difference between both images was most likely due to the slight density change in the affected tissue, due to liquid-filled pores, at the core region which was initially already dense. While the core tissue actually became brown after storage, this change could not be distinguished from the CT image intensity based on tissue density alone. Therefore, segmentation only relying on the CT image of the affected pear may underestimate the browning in low porosity zones where the porosity increase is not significant.

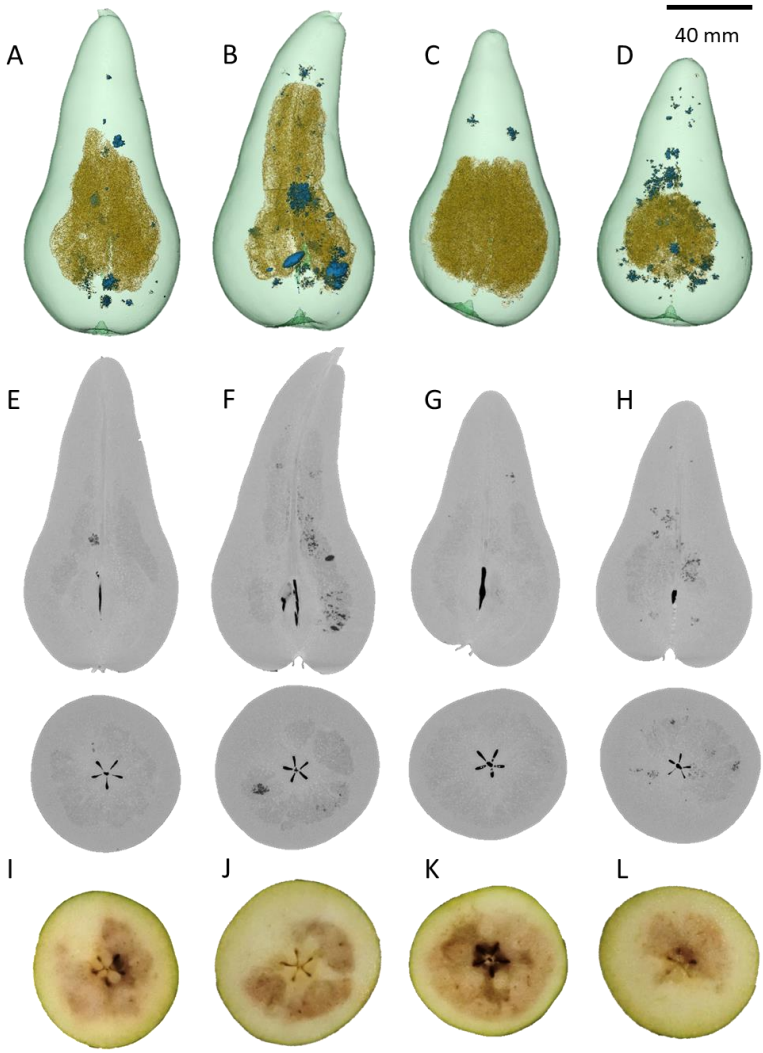

Figure 5.2. (A, B, C and D) 3D geometry of affected pears (numbered 1 to 4) in which the brown volume represents the browning symptoms and the small blue spots are the cavities. (E, F, G and H) grayscale CT image of vertical (top) and horizontal (bottom) slices, (I, J, K and L) photographs of corresponding horizontal pear slices.

A volumetric analysis of the volume and percentage of the affected tissue, brown tissue, and cavities is summarized in Table 5.2. The volume of the affected tissue was defined as the sum of the volumes of the brown tissue and cavities in the slices. The percentages of the affected tissue based on either the relative change in porosity map or photograph were statistically comparable.

Table 5.2. Volumetric analysis of browning disorder in pear, with V the volume of the pear sample, and P their percentage relative to the volume of the entire pear.

Sample	$V_p\,(cm^3)$	$V_{at}\,(cm^3)$	$V_b\,(cm^3)$	$V_c\,(cm^3)$	$P_{at}\,(\%)$	$P_b\,(\%)$	$P_c\,(\%)$	$P_{at}^*\,(\%)$
1	294.2	64.00	63.78	0.21	21.75	21.68	0.07	21.34
2	333.4	80.55	79.50	1.05	24.16	23.85	0.31	20.67
3	272.2	92.42	92.39	0.03	33.95	33.94	0.01	36.01
4	260.3	46.92	46.55	0.37	18.03	17.89	0.14	16.66

subscripts: *p* = pear; *at* = affected tissue; *b* = brown tissue; *c* = cavities; superscript: * = area fraction from the photograph. No statistical difference between P_{at} and P_{at}^* ($p > 0.05$).

There was no relation between the total volume of the pear and percentage of the affected tissue. Pear 4 and 3 were the smallest, but they had the smallest (18 %) and largest (34 %) volume percentage of affected tissue, respectively. The volume of affected tissue was also not related to the total volume of the pear in case of cavity formation. The largest cavity was found in pear 2, corresponding to 0.31 % of the total sample volume.

5.3.2 Map of effective O_2 and CO_2 diffusivity

The effective O_2 diffusivity in an intact pear was lower than the effective CO_2 diffusivity, but the spatial distribution of the O_2 and CO_2 diffusivity was similar due to their linear correlation (Figure 5.3). The porosity maps can be found in Supplementary Materials B3. In sound pears, larger values of effective O_2 and CO_2 diffusivity were mostly positioned in the cortex tissue, while the smaller values were located near the skin, and in the core and neck region (Figure 5.3). Pear 4 (Figure 5.3D and H) generally showed the highest effective O_2 and CO_2 diffusivity, while the other samples appeared very similar. The maps were then integrated into Equation 5.2 to compute the internal gas gradients and link the result with the incidence of internal browning.

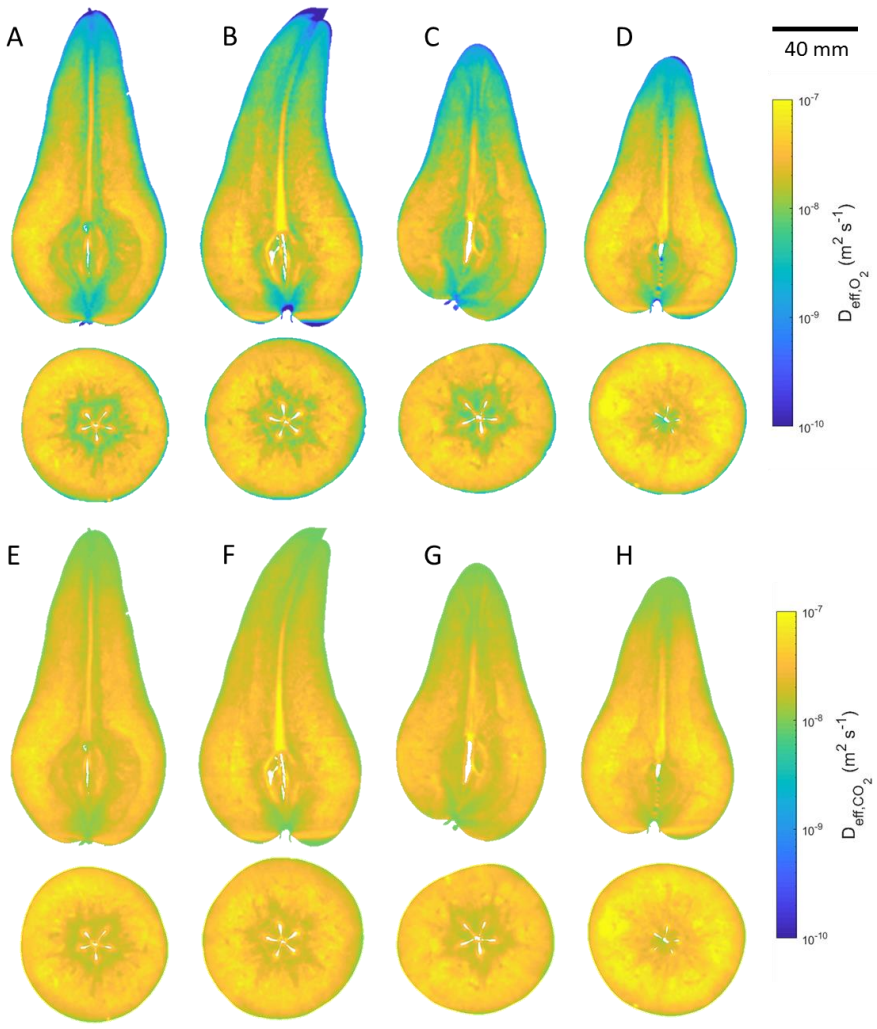

Figure 5.3. Effective diffusivity maps for (A, B, C and D) oxygen and (E, F, G and H) carbon dioxide in sound pears created using the developed models in Chapter 4 and Equation 5.1, respectively. The porosity maps can be found in Supplementary Material B3.

After 8-months storage, the severe development of browning and cavities considerably altered the effective diffusivity of O_2 and CO_2 (Figure 5.4) to be higher and lower in certain areas relative to that of sound pear. The maximum diffusivity was identical to that of O_2 and CO_2 in the air inside the cavities.

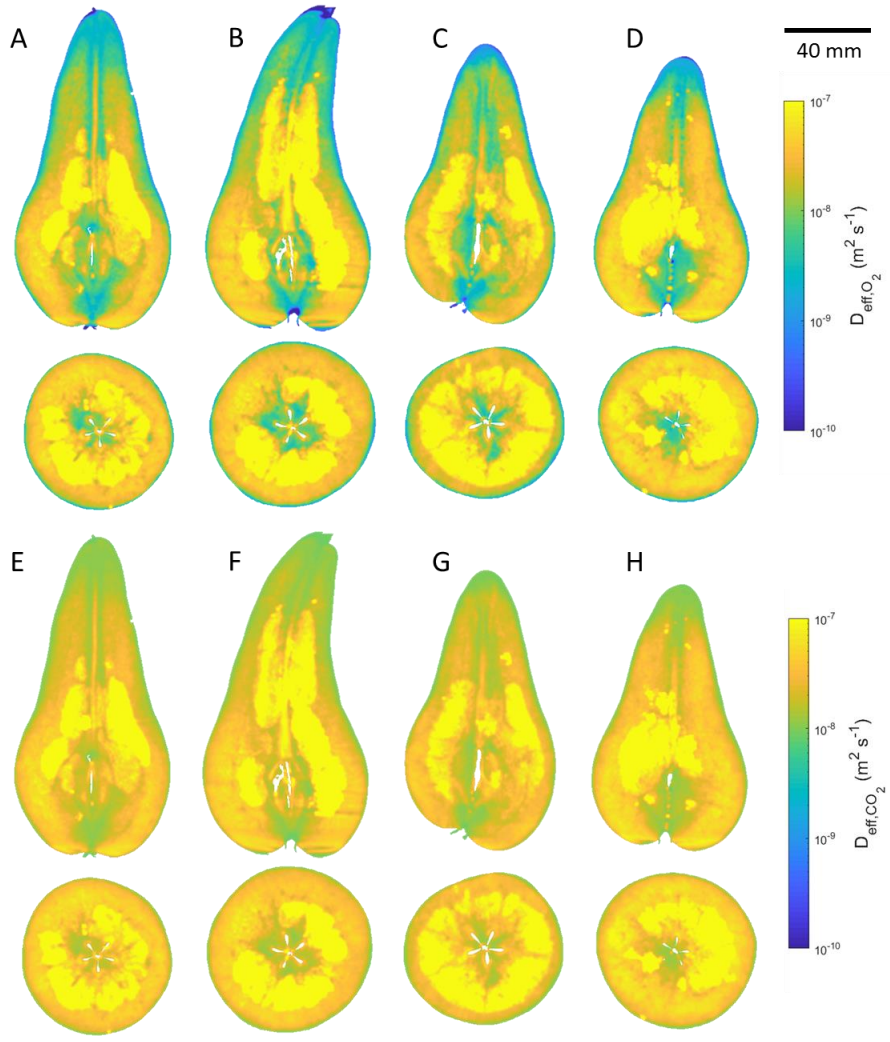

Figure 5.4. Effective diffusivity maps for (A, B, C and D) oxygen and (E, F, G and H) carbon dioxide in affected pears created using the developed models in Chapter 4 and Equation 5.1, respectively.

The mean porosity, effective O_2 and CO_2 diffusivities in each pear and condition are presented in Table 5.3. There is a considerable difference between the values for these properties in healthy and affected tissue. The development of browning and cavities after 8-months storage causes changes in the porosity of the fruit.

This is especially clear in pear 2, which had the largest volume of brown tissue and cavities of all affected pear fruit (Table 5.2).

Table 5.3. Mean values (± standard deviation) of porosity, O_2 and CO_2 diffusivity.

Sample	Condition	ε_{mean} (%)	$D_{O_2,eff,mean}$ ($\times 10^{-8}$ m^2 s^{-1})	$D_{CO_2,eff,mean}$ ($\times 10^{-8}$ m^2 s^{-1})
1	Sound	4.27 ± 1.10	2.65 ± 1.70	3.29 ± 1.49
	Affected	4.95 ± 2.47	5.04 ± 15.7	5.38 ± 13.7
2	Sound	4.20 ± 1.09	2.54 ± 1.64	3.19 ± 1.44
	Affected	5.41 ± 5.00	9.24 ± 63.9	9.07 ± 56.1
3	Sound	4.09 ± 1.07	2.33 ± 1.47	3.01 ± 1.29
	Affected	4.87 ± 1.98	4.65 ± 6.50	5.04 ± 5.70
4	Sound	4.75 ± 1.22	3.68 ± 2.25	4.19 ± 1.97
	Affected	5.53 ± 3.07	6.78 ± 16.1	6.91 ± 1.41

5.3.3 Gas exchange simulations

The exchange of respiratory gasses was simulated by taking into account the spatial distribution of diffusivity in the sound pears. The model predicted the internal O_2 and CO_2, concentration and RQ profiles for the storage condition of 1.0 kPa O_2, 0.7 kPa CO_2 at 1 ºC and 0.5 kPa O_2, 0.7 kPa CO_2 at 1 ºC. As a comparison, reference O_2 and CO_2 concentration and RQ profiles were computed using a uniform (average) O_2 and CO_2 diffusivity. The prediction results were then interpreted with respect to the incidence of internal browning found after storage.

The internal O_2 (Figure 5.5A, B, C and D) and CO_2 (Figure 5.5E, F, G and H) concentrations decreased and increased towards the pear center, respectively. Minimal O_2 concentrations were around 0.10 kPa for pear 1, 2 and 3. For pear 4, the minimal O_2 level was higher (0.17 kPa) than the levels in the other pear samples (Figure 5.5D). No obvious gradient in RQ level was observed inside

the pears (Figure 5.5I, J, K and L). The RQ levels were slightly higher in the core region with a maximal value of 1.0-1.7.

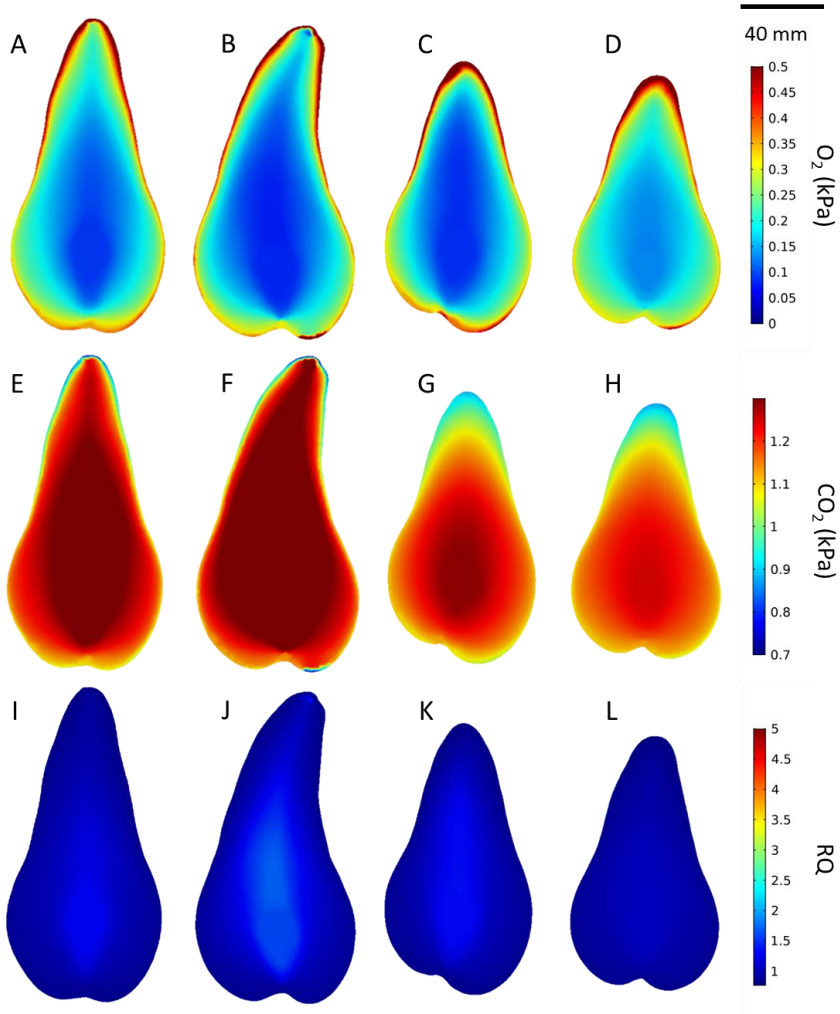

Figure 5.5. Internal O_2 (top) and CO_2 (middle) concentration, and RQ (bottom) profiles of (A, E, I) pear 1, (B, F, J) pear 2, (C, G, K) pear 3 and (D, H, L) pear 4 predicted using the diffusivity map at 1.0 kPa O_2, 0.7 kPa CO_2 and 1.0 ^oC.

Since there was no internal browning found at 1.0 kPa O_2 after the first 4-month storage, the oxygen level in the storage headspace was decreased to 0.50 kPa O_2. Given that the other parameters are the same, the simulation results are shown in Figure 5.6.

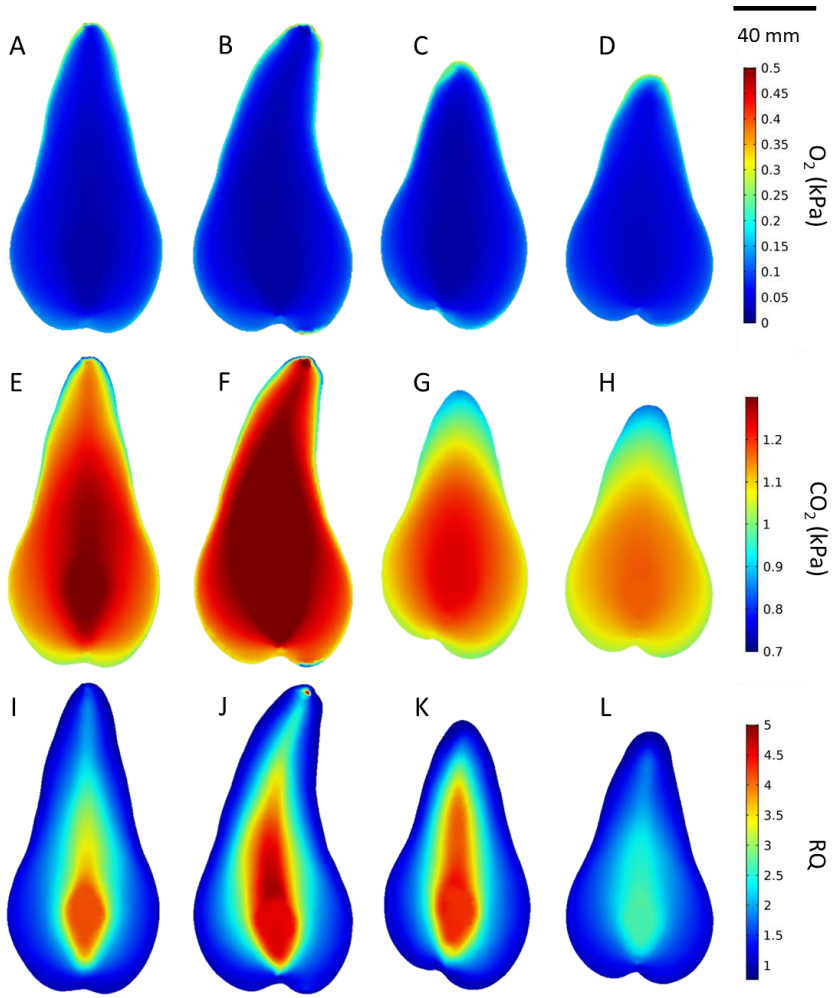

Figure 5.6. Internal O_2 (top) and CO_2 (middle) concentration, and RQ (bottom) profile of (A, E, I) pear 1, (B, F, J) pear 2, (C, G, K) pear 3 and (D, H, L) pear 4 predicted using the diffusivity map at 0.5 kPa O_2, 0.7 kPa CO_2 and 1 ^{o}C.

Compared to the simulation results at 1.0 kPa O_2, the internal O_2 level calculated under 0.5 kPa O_2 condition dropped below 0.1 kPa with slight gradients from the outer to inner parts (Figure 5.6A, B, C and D). The CO_2 concentration at the center was greater than that at the periphery (Figure 5.6E, F, G and H). The internal RQ levels increased considerably above 1 towards the core region (Figure 5.6I, J, K and L) at which the O_2 and CO_2 partial pressures were found minimal and maximal, respectively. The internal RQ gradient was less steep in

pear 4 (1.0 – 2.7) which had a larger O_2 and CO_2 diffusivity (Figure 5.3D and H). The results confirm that differences in tissue porosity (Supplementary Material B3) and, thus, O_2 and CO_2 diffusivity (Figure 5.3), may partially explain differences in internal gas gradients (Figure 5.5 and 5.6).

Different results were found in model simulations based on a homogenous diffusivity for both O_2 and CO_2 (Figure 5.7). The internal O_2 and CO_2 concentration and RQ profiles were more uniform across the entire pear tissue than those computed using the diffusivity map of O_2 and CO_2. The internal RQ levels that were predicted remained around 1 (aerobic respiration) in all tissue positions (Figure 5.7I, J, K and L). This is contradictory with the observed internal browning after storage.

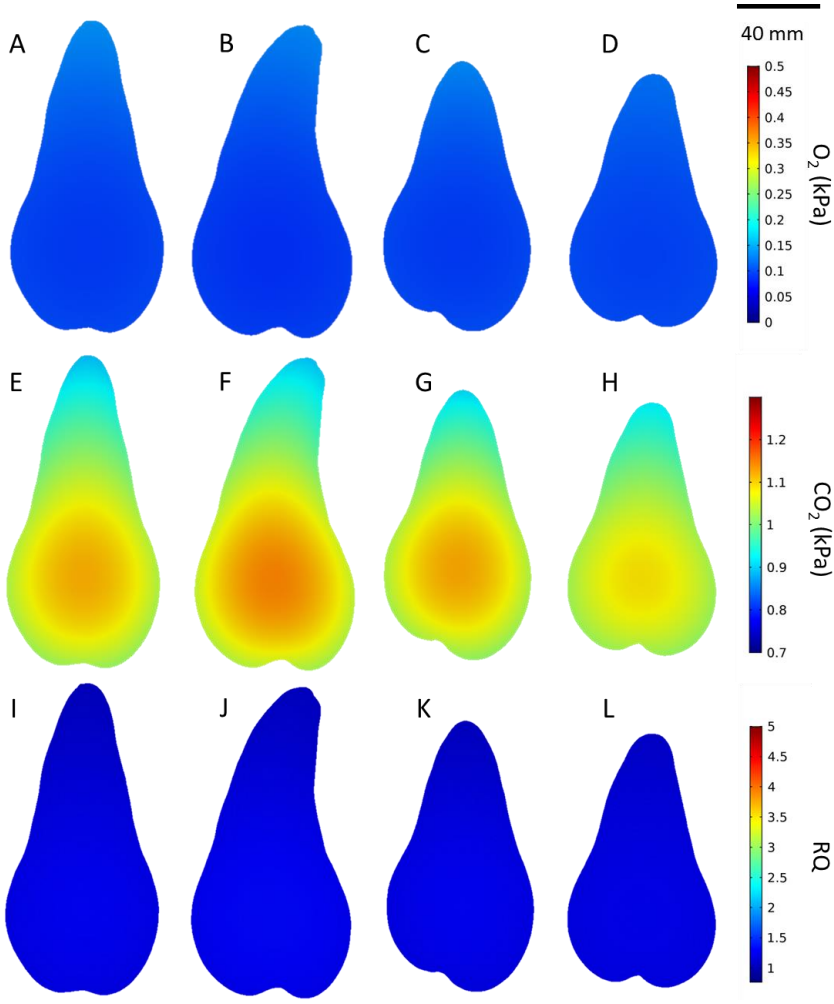

Figure 5.7. Internal O_2 (top) and CO_2 (middle) concentration and RQ (bottom) profile of (A, E, I) pear 1, (B, F, J) pear 2, (C, G, K) pear 3 and (D, H, L) pear 4 predicted using single diffusivity as the model parameter at 0.5 kPa O_2, 0.7 kPa CO_2 and 1 ^oC.

5.3.4 Difference between map and uniform diffusivity-based simulations

The relative difference profiles depended on the relative position along the fruit equator (Figure 5.8). The relative difference is the diffusivity map- and uniform diffusivity-based O_2 and O_2 concentration and RQ profiles divided by those obtained assuming a uniform diffusivity. A negative or positive sign indicates

that the diffusivity map-based prediction results were lower or higher than those obtained with a uniform diffusivity, respectively. At the fruit skin the map-based O_2 concentration profiles were 30 to 50 % larger than the uniform diffusivity-based profile, while at the fruit center they were 80 to 60 % smaller (Figure 5.8A). For the CO_2 concentration the diffusivity map-based simulation resulted in 8 to 20 % larger values than the uniform diffusivity based simulation at the pear center (Figure 5.8B). The relative difference was small compared to that for the oxygen profile. A considerable relative difference can be observed for the respiratory quotient (RQ) level. At the center, the diffusivity map-based prediction results were around 240 % higher than the ones predicted using the uniform diffusivity, except for pear 4 (120 %) (Figure 5.8C).

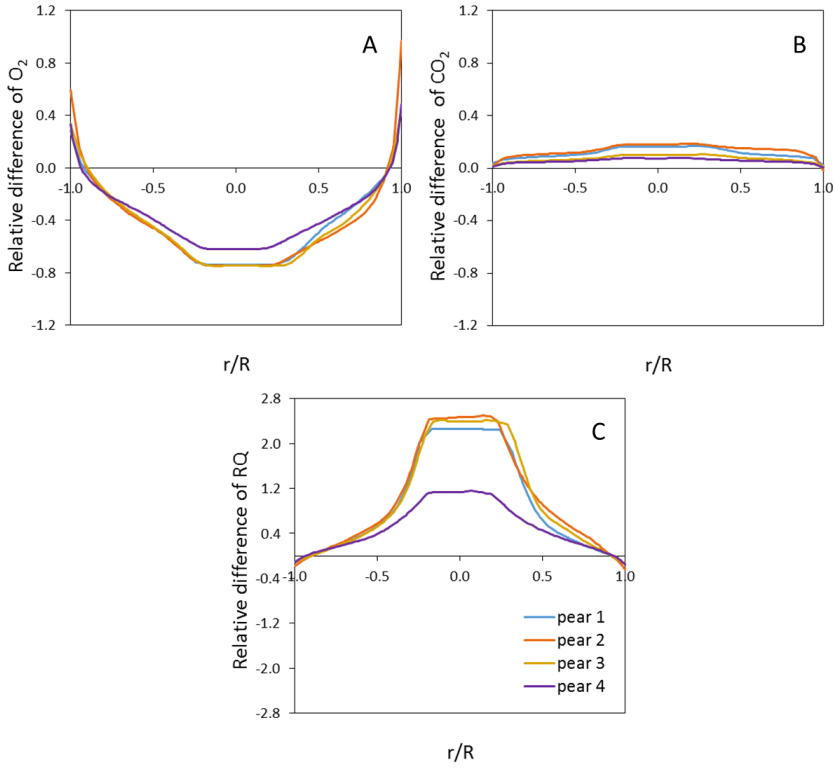

Figure 5.8. Relative difference profiles for (A) O_2 concentration (B) CO_2 concentration and (C) RQ as predicted with the model incorporating the diffusivity map with respect to simulations using a homogenous O_2 and CO_2 diffusivity at 0.5 kPa O_2, 0.7 kPa CO_2 and 1 ^oC. Values are plotted as a function of the non-dimensional position along the radius (*r/R*) of the four pear samples.

5.3.5 Critical O_2 limit and internal browning occurrence

The critical O_2 limit was estimated to explain the occurrence of internal browning based on the simulation results. From the prediction results, the minimal O_2 concentrations in pears 1, 2, 3 and 4 were 0.017 kPa, 0.018 kPa, 0.006 kPa and 0.035 kPa, respectively. Except for pear 4, the lowest O_2 levels were all below the calculated critical O_2 limit ($C^*_{O_2}$) of 0.034 kPa, assuming f_o = 6.33. This value assumes a maximal yield of the respiration pathway (38 ATP), which is hardly ever reached due to the complexity of the respiratory chain and the ATP synthase mechanisms (Rich, 2003). A more realistic range is from 30 to 32 ATP, corresponding to f_o = 30/6 = 5 (Edwards *et al.*, 2012). With this value, the estimated $C^*_{O_2}$ was 0.044 kPa, well above the lowest O_2 concentration in all four pears.

At 1.0 kPa O_2, a slight increase in the RQ level occurred as the level of O_2 decreased from 0.45 to 0.07 (Figure 5.9A). The RQ levels were mostly below 1, indicating an aerobic condition. At 0.5 kPa O_2, an exponential increase in the RQ levels was observed, while the internal O_2 level dropped below the $C^*_{O_2}$ of 0.044 kPa (Figure 5.9B) at which the critical RQ limit (RQ^*) was 2.12.

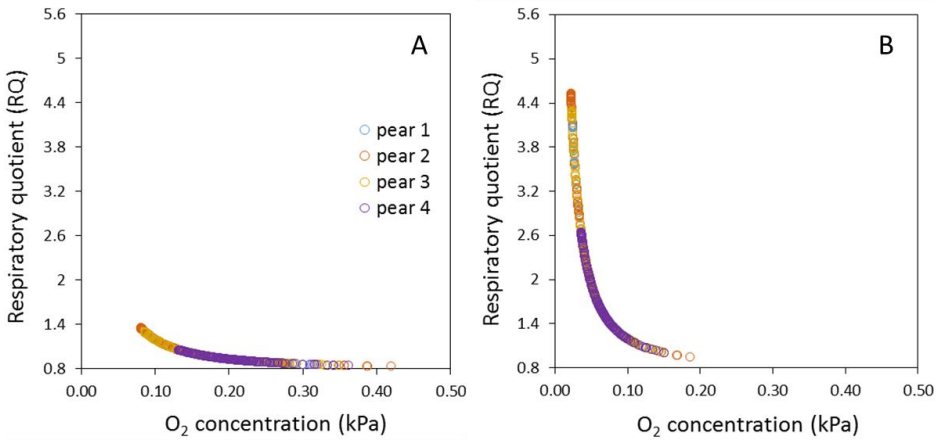

Figure 5.9. Simulated RQ values as a function of the simulated O_2 levels in the pear at (A) 1.0 kPa O_2 and (B) 0.5 kPa O_2. Different colors represent different pear samples.

The region at which the RQ level was above the aforementioned limit was approximately comparable to the area of the browning-affected tissue (Figure 5.10). When fermentation was predicted by the diffusivity map-based simulation in a certain tissue area, this did not necessarily mean that the predicted fermentation area would become brown. As the gas exchange simulation was only conducted on healthy pears, some local incidences which occurred outside the fermentation area were most likely caused by the development of browning during low O_2 storage.

On the contrary, neither internal O_2 concentrations nor RQ levels simulated using the regular multiscale modeling revealed the incidence of internal browning, while the minimal O_2 concentration and/or maximal RQ level of all pears were well below the critical thresholds.

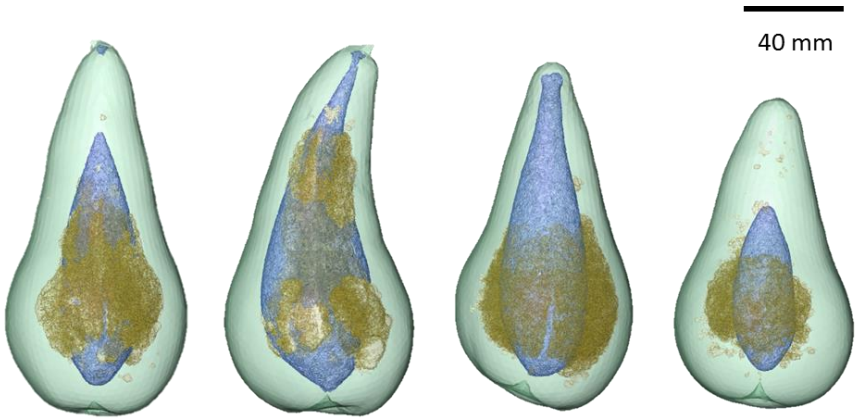

Figure 5.10. Browning area (brown color) imaged using X-ray CT and the area indicated to undergo fermentation (blue color) based on the predicted RQ values inside the pear. The fermentation process was indicated to be dominant when the RQ^* went above 2.12 (or at 0.044 kPa O_2).

5.4 Discussion

Accurate simulation of gas compositions in stored fruit can be greatly beneficial for understanding and improving CA or DCA storage applications. However, the multiscale modeling approach previously developed has limited accuracy in

predicting the internal gas concentrations since the microstructure of the fruit tissue is not uniform over the entire organ and, consequently, affects respiratory gas exchange (Ho *et al*., 2011). Low availability of oxygen in plant cells may result from a high diffusion resistance of oxygen presented by tissues (Gran and Beaudry, 1993; Geigenberger, 2003; van Dongen *et al*., 2011; Ho *et al*., 2013b). In this study, effective oxygen and carbon dioxide diffusivities were quantified and visualized in pears based on X-ray CT images using the technique of the diffusivity map developed in Chapter 4. A large variation in the O_2 and CO_2 diffusivity within a fruit or among the individual pears reflects the heterogeneity in the tissue microstructure (Figure 5.3). The diffusivity variation along the pear radial axis was previously observed by Schotsmans *et al.* (2003). Variations in pear shape and size, the amount of lignified cells, cell distribution and growing condition all contribute to the biological variability in diffusivity of the pear (Ho *et al*., 2006a), which acts in different capacities to facilitate the diffusion of respiratory gasses.

This study integrated the spatial variability in the O_2 and CO_2 diffusivity into an existing gas exchange model developed by Ho *et al*. (2006b, 2008, 2010a, 2011) to predict the local O_2 and CO_2 concentrations inside the pear. Also, the respiratory quotient (RQ) used as a low O_2 stress signal in dynamic controlled atmosphere (DCA) (Bessemans *et al*., 2016, 2020) was, for the first time, predicted and mapped in an entire pear organ. The distribution of internal gas concentrations and RQ level was similar to the spatial variation of the effective O_2 and CO_2 diffusivity and depended on the external gas conditions (Figure 5.5 and 5.6). Furthermore, at 0.5 kPa O_2, depletion of O_2 and an increase of the CO_2 concentration and RQ levels were steeper (Figure 5.6) than when a homogeneous O_2 and CO_2 diffusivity was assumed (Figure 5.7), caused by areas of low diffusivity in the core.

The internal gas concentration plays a vital role in fruit respiration (Lammertyn *et al*., 2003a), and, hence, the energy availability for cell membrane maintenance (Lammertyn *et al*., 2003a; van Dongen *et al*., 2011). Excessively low oxygen

availability in the tissue may stall aerobic respiration and initiate fermentation, leading to a reduced supply of ATP for energy-demanding activities (Boeckx *et al*., 2019). Even though cells can temporarily adapt to a low metabolic energy status, they may lose membrane integrity after a certain period of time (Rawyler *et al*., 1999) and die. For 'Conference' pear, incidence of internal disorders in relation to the limited availability of energy was already observed by Veltman *et al*. (2003). A mechanistic approach based on the supply energy criteria (Ho *et al*,. 2013b) was applied to determine the critical O_2 limit at which the respiration-to-fermentation switch occurs. The critical O_2 limit (0.044 kPa) did correspond approximately to an RQ of 2.12 inside the pear.

The predicted oxygen and RQ levels did not drop below the critical O_2 and above the critical RQ limit, respectively, for storage under 1.0 kPa O_2 (Figure 5.5). This explains the absence of internal browning inside the test samples after 4 months of storage. When the storage O_2 partial pressure was decreased to 0.5 kPa, the internal O_2 and RQ gradients in all pears crossed the critical thresholds (Figure 5.6), indicating insufficient energy for normal cell maintenance of the pear tissue. Previous research found that fermentation occurs when the RQ levels increase above 1.3 (Kader and Saltveit, 2002). The predicted result corresponded to the observation of browning and cavities in the pear samples after storage. Lammertyn *et al*. (2003c,d) hypothesized that the cytoplasm releases into the intercellular space when the cell membrane integrity is lost and locally leads to a reduction of the porosity. The liquid then gradually diffuses through the pear skin, evaporates and leaves cavities inside the pear. These processes result in an increase in the porosity and diffusivity of the affected pear (Supplementary B3 and Figure 5.4).

Furthermore, the level of browning-affected tissue was more or less aligned with the internal gas concentration contours and, thus, the effective tissue diffusivity. For instance, pear 4 with a larger diffusivity showed the shallowest RQ gradients that are closest to the limit and, hence, the smallest fraction of tissue with browning symptoms (18 %) compared to fruit with lower diffusivity (22 – 34

%). These results also support the hypothesis that the internal RQ levels are affected by the diffusion resistance (Gran and Beaudry, 1993; Bessemans *et al*., 2020). The difference in the tissue microstructure between apple cultivars associated with different critical O_2 limits explained the differences in their optimal storage conditions (Ho *et al*., 2013b). In future studies, the experimental measurement of internal gas concentration is, however, required to validate this improved gas exchange model.

The segmented area beyond the critical RQ limit agreed quite well with the actual area of the affected tissue (Figure 5.10). The deviation between the predicted and observed areas is most likely due to that the sample and respiration parameters used for the simulation were estimated for sound pears. In disorder-inducing conditions, some tissue regions which did not become brown might have adapted to the limited availability of energy. Later on, the tissue microstructure and, most likely, the respiration activity of pear may change due to the changes caused by the storage disorder and thus affect internal gas and RQ levels compared to those of healthy pear fruit. Investigation of gas transport in browning-affected pear fruit is, therefore, required in future research.

Besides the morphology of the pore structure and diffusion resistance, the high incidence of browning and cavities, as observed in all investigated pears, was most likely affected by the late harvest date. Franck *et al*. (2007) described that 'Conference' pear fruit harvested at a late harvest date are more susceptible to this disorder than fruit picked at the optimum harvest date. Based on stochastic simulations, Ho *et al*. (2016) found that the occurrence of browning and cavities is high for late picked pears when stored at an O_2 partial pressure of 0.5 kPa (74%) and it increases with storage time (1-9 months). The occurrence decreases with increasing applied O_2 in the storage headspace (Ho *et al*., 2016). The increased susceptibility of late harvested pear is likely due to the higher maximum respiration rate that contributes to the internal gas gradients (Franck *et al*., 2007; Ho *et al*., 2016). Temperature also affects the respiration rate of pear as given by the activation energy (Ho *et al*., 2016, 2018). Hence, temperature is

most likely another factor, which exacerbates internal browning since pear fruit is better preserved at -1 °C rather than 1°C used here. Finally, ripe pears are typically larger than unripe pears and gas transport is highly affected by size.

5.5 Conclusions

Using the diffusivity mapping technique developed in Chapter 4, gas exchange simulations taking into account the spatial variability in the effective diffusivity were successfully pioneered in this study to predict the internal gas gradients in pear. Effective O_2 and CO_2 diffusivity maps incorporated into the macroscale model contributed to more realistic O_2 and CO_2 concentration and respiratory quotient profiles inside 'Conference' pear fruit that were in line with the local magnitude of the diffusivity distribution. The contours of critical O_2 concentrations or RQ levels corresponded to some extent to brown tissue and cavities found after long-term CA storage. Conventional multiscale gas exchange models that assume a homogeneous O_2 and CO_2 diffusivity failed to explain the occurrence of browning and cavities as the predicted gas concentrations indicated a normal aerobic respiration process, even at low oxygen partial pressures. Furthermore, it would be interesting to carry out gas exchange simulations in affected pears as the locally affected tissue changes the gas transport properties. For this purpose, respiration measurements and diffusivity maps of affected pears at different levels of browning and cavity formation should be acquired.

Chapter 6

General conclusions and future perspectives

6.1 General conclusions

Recent studies of the microstructure of pome fruit using X-ray micro CT have shown a considerable variation in the tissue porosity although the tissues seem homogenous from a macroscopic point of view. Until now, the effect of this heterogeneity on the transport of respiratory gasses inside the fruit was not known, due to the fact that it was not yet possible to compute macroscopic O_2 and CO_2 concentration profiles taking into account microscale features. This PhD study has focused on the development of a method to compute the spatial variability in gas transport properties in intact fruit and vegetables and the integration of these properties into an existing metabolic gas exchange model.

First, in chapter 3, a method that high and low resolution X-ray CT scans was combined to generate porosity maps that fit entire fruit shapes and integrate microstructural features of the tissue. The method is based on the computation of the local tissue porosity of fruit and vegetables based on a linear regression model predicting porosity from the grayscale intensity. The actual local porosity was calculated from high resolution X-ray CT images. As the grayscale values of the juice and image background (air) impart the two reference values of the linear regression model (0 % and 100 % porosity), this mapping technique is easily applicable to other horticultural products by only scanning the intact sample with its juice by means of an interpolation method. Assessment of the CT image quality using a homogeneous water phantom helped in minimizing unrealistic predictions due to CT artifacts such as beam hardening.

Next, these porosity maps were converted into effective O_2 and CO_2 diffusivity maps (Chapter 4). The effective oxygen diffusivity strongly depends on the microstructure, but cannot be estimated from the total porosity alone, especially for products with less connected pores. As a result, the diffusivity generally links

better with open porosity that only computes the connected pores as the primary routes of oxygen diffusion. Diffusivity mapping in apple and pear, which have lower pore connectivity, had to be based on the open porosity, while the mapping in eggplant and turnip could be based on the total porosity thanks to their high pore connectivity. A regression model was established between the total and open porosity in apple and pear. Both the 3D porosity and the effective O_2 and CO_2 diffusivity maps nicely reflected the variability in the tissue microstructure that is position and sample dependent. For apple and pear that have long been a subject of gas transport studies, low porosity and diffusivity values were situated below the skin, the core region and around the vascular bundles.

In Chapter 5, the O_2 and CO_2 diffusivity maps were incorporated into a gas exchange model for pear to compute the internal gas concentrations and respiratory quotient (RQ) distribution inside pear fruit stored under hypoxic conditions and linked these to the occurrence of internal browning. Compared to the results predicted using the regular multiscale approach assuming homogeneous O_2 and CO_2 diffusivity, the large spatial variation in the O_2 and CO_2 and diffusivity resulted in more diverse and steeper contours for the O_2 and CO_2 concentrations and *RQ* values in all pears. The predicted gas compositions also explained well browning and cavity formation after browning-inducing storage where the lowest O_2 concentration falls below a critical O_2 threshold, indicating the occurrence of fermentation. The sample that had the highest O_2 and CO_2 diffusivity had the shallowest gradient of the gasses and consequently the lightest internal browning and cavity formation.

6.2 Future perspectives

Several open questions remain that need to be answered in future research.

The method of porosity mapping developed in Chapter 3 can be adapted to perform online porosity measurements. When done immediately after harvest and before storage this would provide an indirect measure for the susceptibility to browning and cavity formation. Fruit with low porosity could then be stored

in less extreme O_2 conditions than high porosity fruit. As online X-ray CT is currently difficult to perform in industrial conditions, it should be investigated whether radiographic images provide sufficient information on overall porosity at a sufficient resolution.

In Chapter 5 we have also assumed that the O_2 and CO_2 diffusivity are correlated based on literature data. However, it is known that O_2 and CO_2 do not follow the same transport path in fruit tissue due to the solubility of CO_2 in water and, thus, the cytoplasm. More research is required to investigate this assumption and, if needed, an alternative regression model between the diffusivity of CO_2 and the local porosity needs to be developed. Recently, two-phase multiscale gas exchange models have been developed in our research group by Janssen *et al*. (2020b). It would be interesting to extend our method to provide the effective transport parameters in this two-phase transport model. Finally, the tissue microstructure suggests that an orthotropic diffusivity tensor would be more appropriate to describe gas transport than a local isotropic diffusivity. Our method may be extended to also compute orthotropic diffusivity tensors.

The O_2 and CO_2 diffusivity maps integrated into the existing gas exchange model allowed to predict gas concentrations that correspond quite well to the observed symptoms of browning and cavity formation (Chapter 5). However, experimental measurement of internal gas concentrations is needed to validate these predictions. Oxygen microsensors have been used by the host lab in the past, but may introduce measurement artifacts as they are invasive, and alternative methods should be developed. Further, respiration might change during storage and possibly also during the development of browning and cavities affecting the local diffusion constant. Additional research is required to quantify these changes.

Diffusivity mapping and modeling of fermentative metabolites such as ethanol, acetaldehyde and ethyl acetate, as well as ethylene (a major regulator of ripening process) would also be very useful to comprehensively predict and monitor the

central metabolism of the fruit during hypoxia condition (in CA or DCA storage) or during ripening.

Appendix A

A.1. Representative elementary volume (REV) analysis

Physical characteristics of heterogeneous materials are affected by the size of the volume of interest (VOI). The size of the VOI has to be sufficiently large to encompass all microstructural parameters, but it must be smaller than the macroscopic structure (Gitman *et al*., 2006; Ukrainczyk and Koenders, 2014). The radial tissue sample was firstly divided into 18-20 cubical tissue samples (1.3×1.3×1.3) at different tissue depths for each species. The original cubical tissues were then resized to be 1.1×1.1×1.1 mm^3, 0.8×0.8×0.8 mm^3, 0.5×0.5×0.5 mm^3, 0.2×0.2×0.2 mm^3 and 0.1×0.1×0.1 mm^3, in order to ensure the right representative elementary volume (REV) as the O_2 diffusivity computation consumed a lot of memory and computational time for the large samples. The appropriate REV size was determined using the standard deviation of the total porosity, open porosity and effective O_2 diffusivity computed for five samples per radial tissue positions per species. The variability of the standard deviations declines as a function of volume size (in length, mm) and the size where the standard deviation stabilizes determines the REV.

Figure 1 shows the standard deviation of the total porosity as a function of the volume length. Its value decreases with increasing VOI size expressed as volume length (mm). The trend clearly depends on the sample position (different line colors) in the radial direction and the product. For eggplant, the changes of the standard deviation are rather small. More obvious changes can be observed in the 0.1×0.1×0.1 mm^3 to 0.8×0.8×0.8 mm^3 turnip samples and the 0.5×0.5×0.5 mm^3 apple samples. For pear, at small values of the total porosity the standard deviation slightly fluctuates and becomes constant above the 0.8×0.8×0.8 mm^3 VOI size.

In general, similar trends were observed for the standard deviation of the open porosity and effective O_2 diffusivity (Figure 2 and 3). The calculation of the O_2 diffusivity of pear at large VOI sizes was, however, restricted by the memory

space of computer and computational time. This was due to the need for a higher resolution X-ray scan for imaging the denser pear microstructure. As a constant standard deviation of the diffusivity was already reached, it was assumed that its value would not considerably decrease further at larger VOIs. This indicates that representative elementary volume (REV) of the tissue had dimensions equal to $0.8\times0.8\times0.8$ mm^3. This VOI size was large enough to compute the effective O_2 diffusivity and corresponded to a cube of 6×6×6 pixels and in the low resolution image (10×10×10 pixels for pear image).

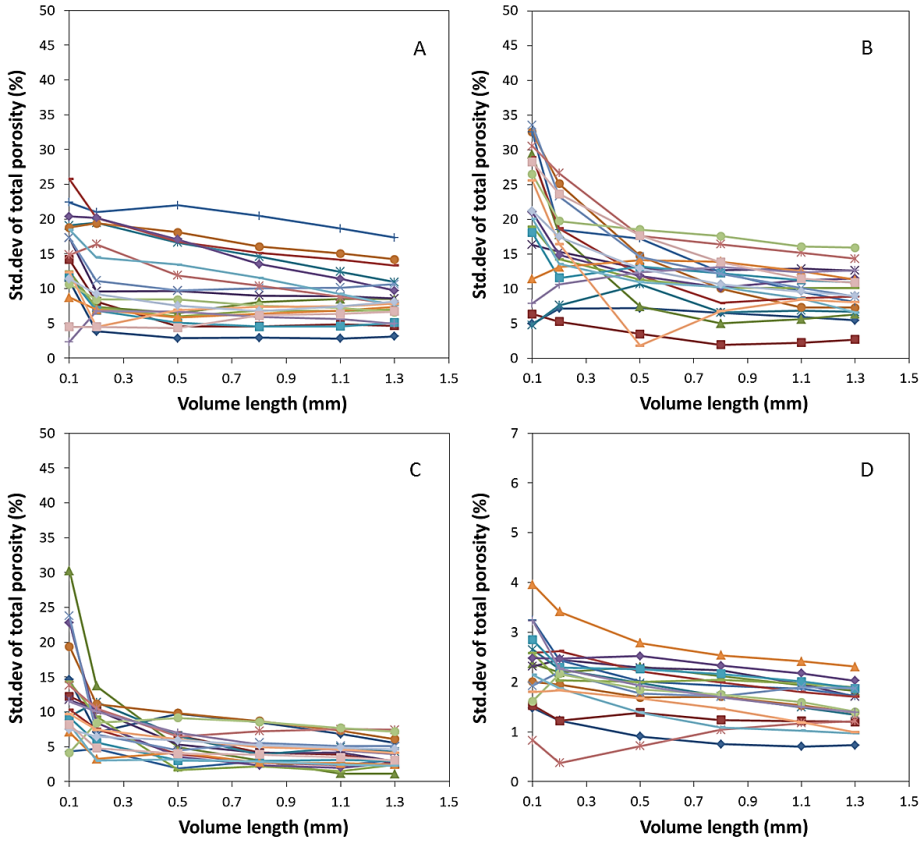

Figure A1. Representative elementary volume (REV) analysis using standard deviation of total porosity (%) plotted versus VOI sizes (in length): (A) eggplant, (B) turnip, (C) apple and (D) pear. Different line colors represent different VOI positions along the radial tissue.

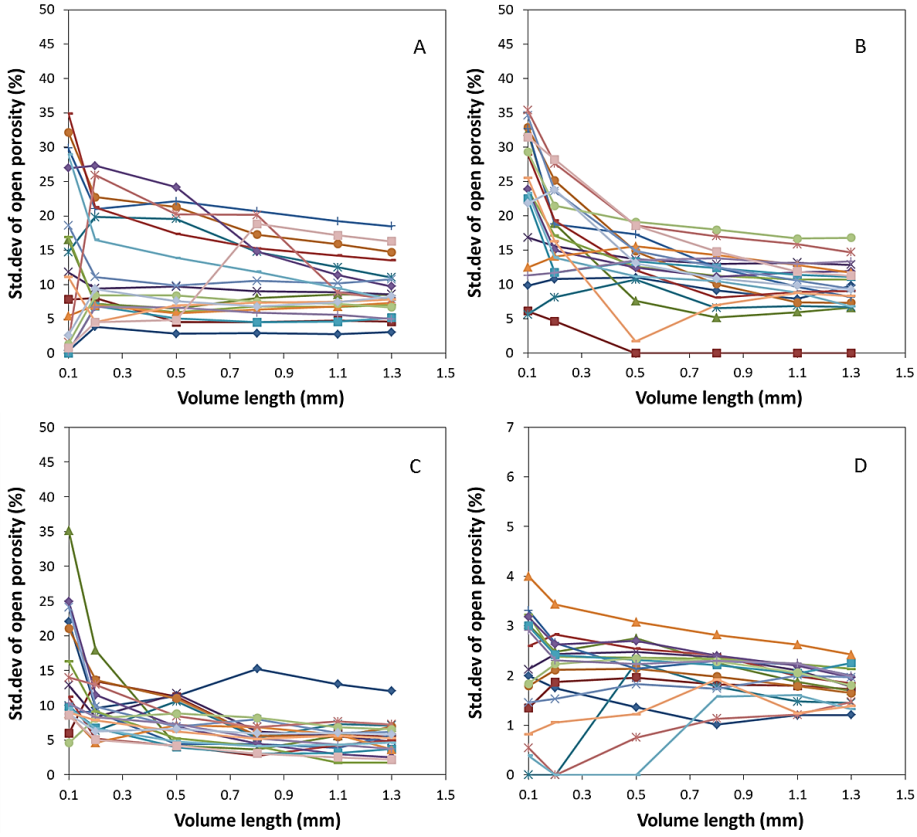

Figure A2. Representative elementary volume (REV) analysis using standard deviation of open porosity (%) plotted versus VOI sizes (in length): (A) eggplant, (B) turnip, (C) apple and (D) pear. Different line colors represent different VOI positions along the radial tissue.

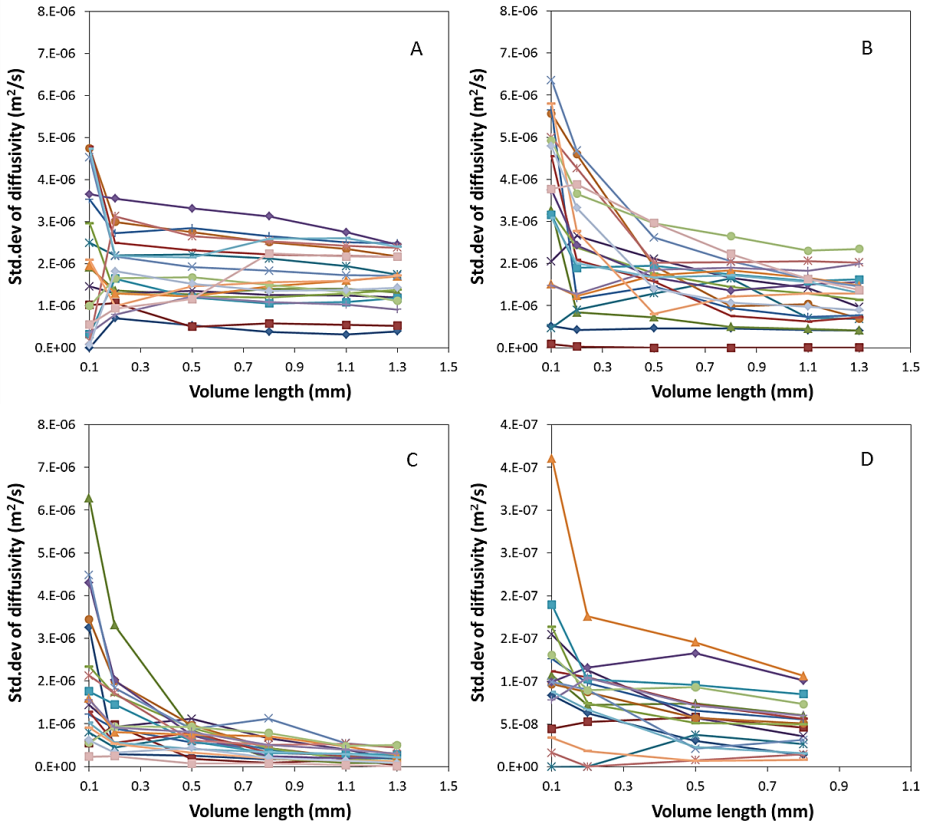

Figure A3. Representative elementary volume (REV) analysis using standard deviation of effective O_2 diffusivity ($m^2\ s^{-1}$) plotted versus VOI sizes (in length): (A) eggplant, (B) turnip, (C) apple and (D) pear. Different line colors represent different VOI positions along the radial tissue.

A.2. Correlation of total porosity versus open porosity for eggplant and turnip

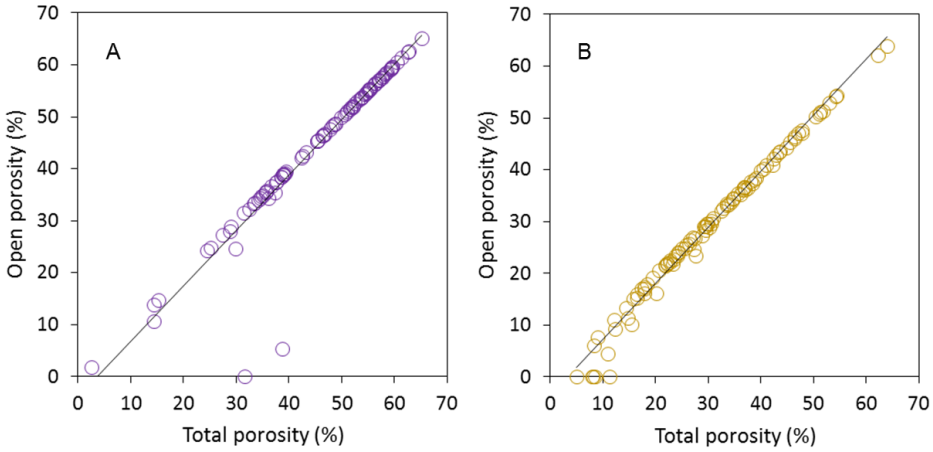

Figure A4. Correlation between total porosity and open porosity for (A) eggplant (R^2 = 0.90; RMSE = 4.49%) and (B) turnip (R^2 = 0.98; RMSE = 1.66%).

A.3. Relation of effective O_2 diffusivity to grayscale intensity

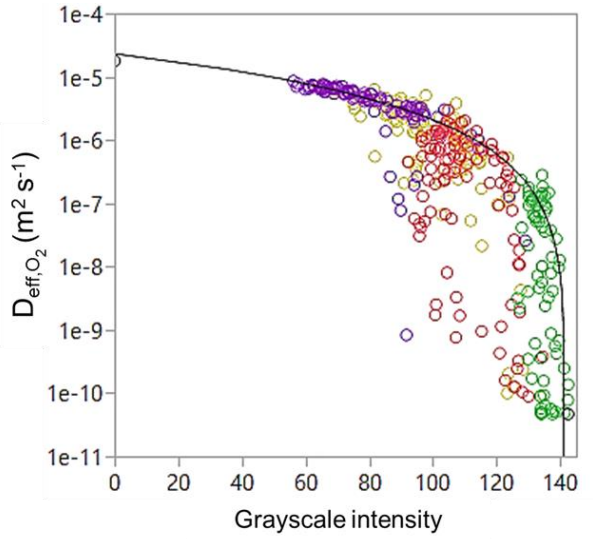

Figure A5. Relation of effective O_2 diffusivity to grayscale intensity of tissue CT image derived from the same position. The model is $D_{O_2,eff} = 1.13e^{-9}g^2 - 3.24e^{-7}g + 2.32e^{-5}$, with $D_{O_2,eff}$ (m^2 s^{-1}) effective O_2 diffusivity and g grayscale intensity ($R^2 = 0.85$; RMSE = $1.012e^{-6}$ m^2 s^{-1}).

A.4. Oxygen concentration profiles

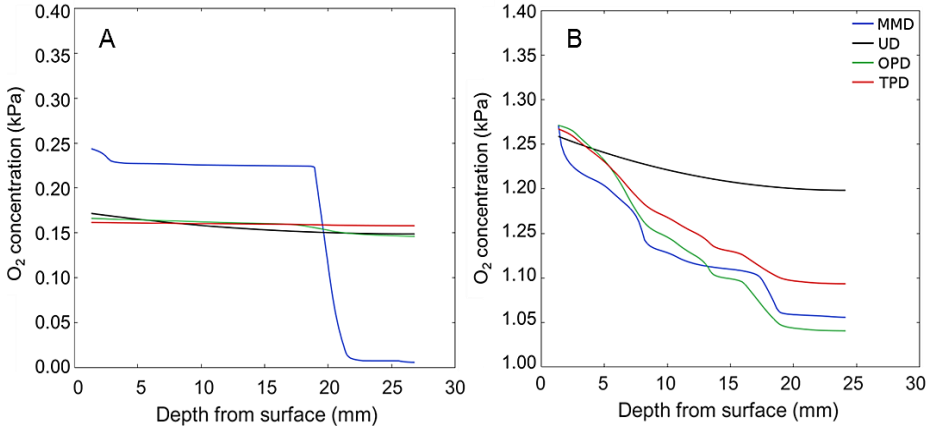

Figure A6. O_2 concentration along the radial tissue of (A) 'Jonagold' apple and (B) 'Conference' pear computed using effective O_2 diffusivity profiles in Figure 4.6. The gas transport computation was performed at the optimal CA storage application for the apple (1 kPa O_2; 2.5 kPa CO_2; 1 ^oC) and pear (2.5 kPa O_2; 0.7 kPa CO_2; -1 ^oC). Different line colors represent the simulations performed using microscale model-based diffusivity (MMD), uniform or single diffusivity (UD), open porosity-based diffusivity (OPD) and total porosity-based diffusivity (TPD).

Appendix B

B.1. Effect of permeation on internal O_2 concentration

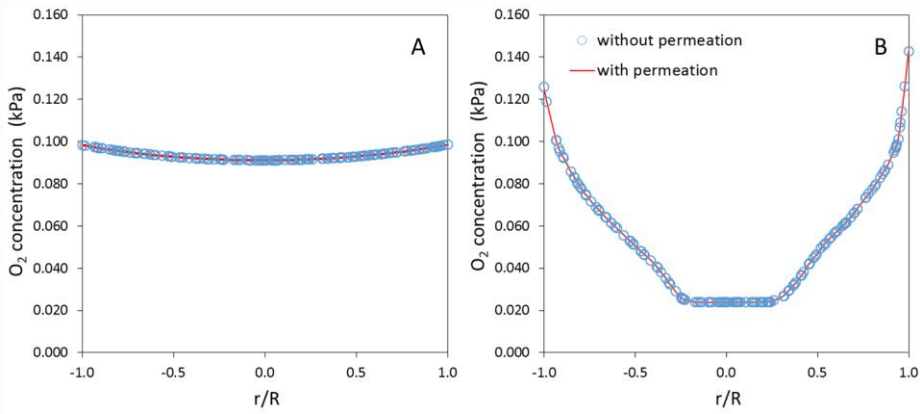

Figure B1. Effect of permeation on internal O_2 concentration simulated using (A) single diffusivity and (B) diffusivity map at 0.5 kPa O_2, 0.7 kPa CO_2, 98.8 kPa N_2 at 1 ^oC. There is no obvious difference between the simulations. Values are plotted as a function of the non-dimensional position along the equatorial axis (*r/R*) of the pear fruit.

B.2. O_2 diffusivity profiles of the original and binned maps

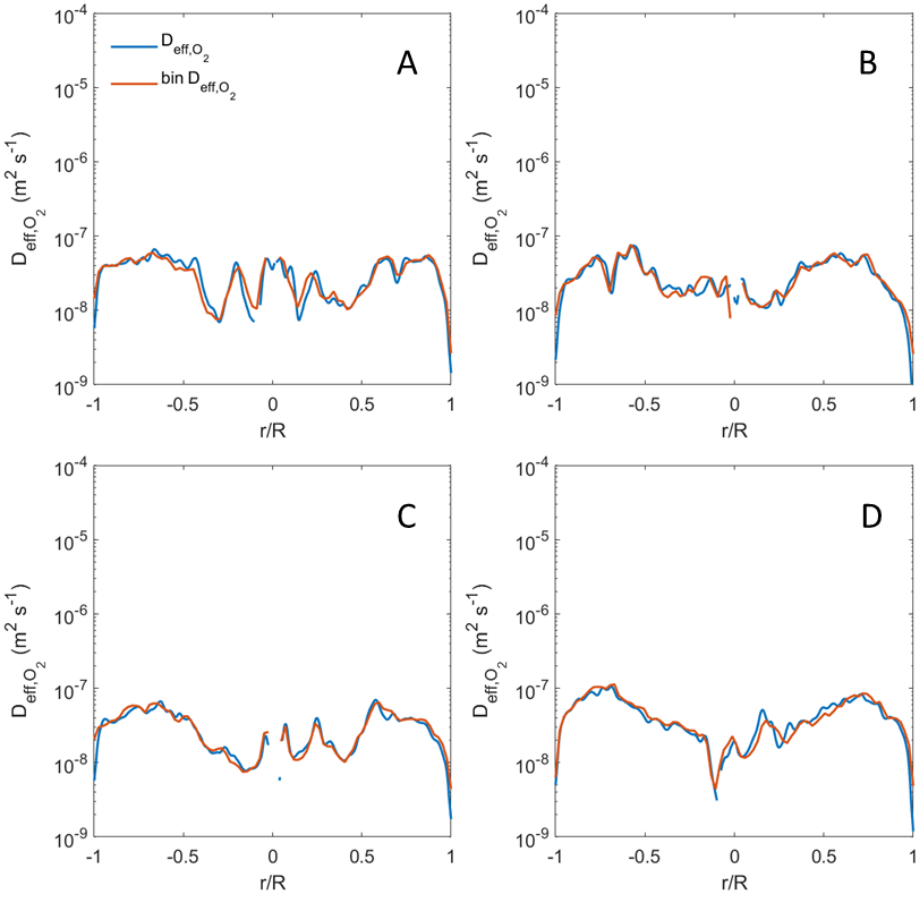

Figure B2. Profiles of effective O_2 diffusivity extracted from the equatorial axis of the original (blue line) and binned (red line) diffusivity maps of (A) pear 1, (B) pear 2, (C) pear 3 and (D) pear 4. The 10 voxels of the original maps were binned by means of an interpolation procedure in Matlab. Only small differences between the two profiles can be observed.

B.3. Porosity map of sound and affected pears

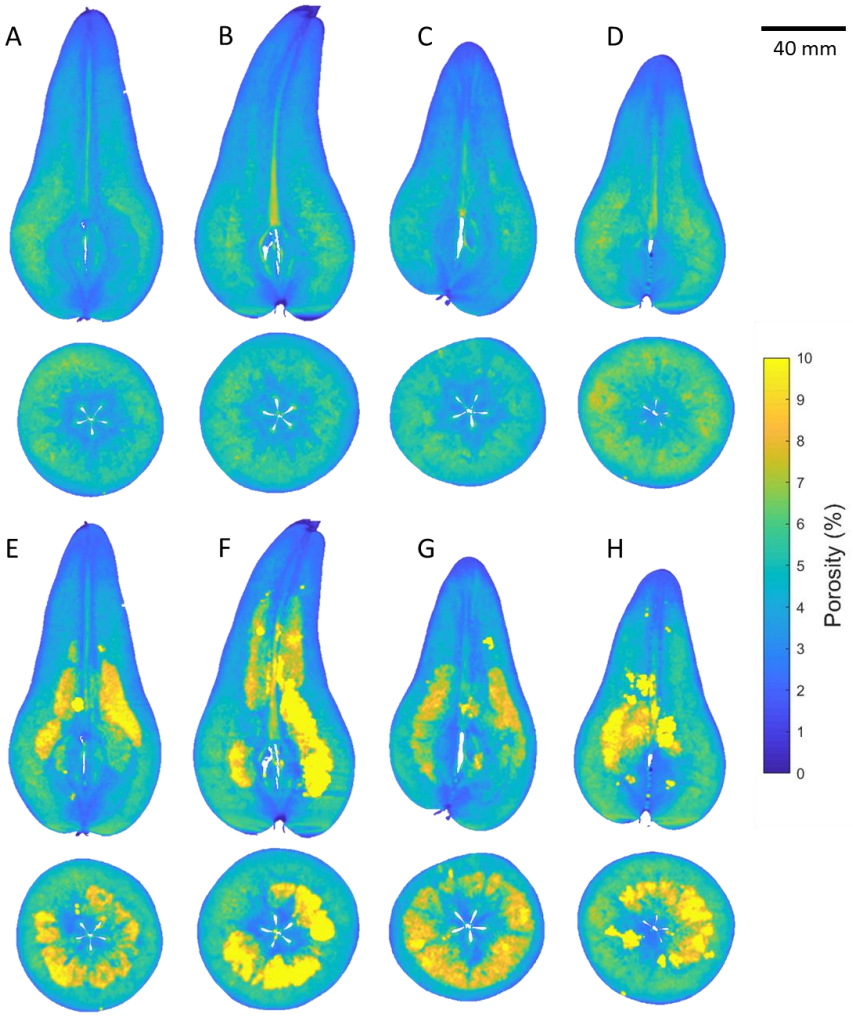

Figure B3. Porosity map of (A, B, C and D) sound and (E, F, G and H) affected pear created using the developed models in Chapter 3.

B.4. Profiles of porosity, O_2 and CO_2 diffusivities

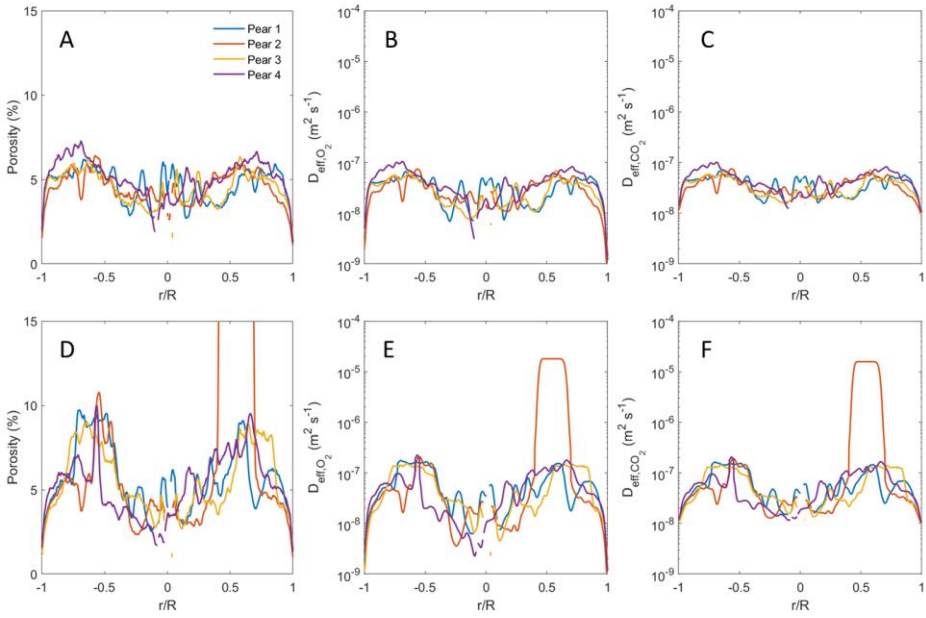

Figure B4. Profiles of (A and D) porosity, (B and E) effective O_2 diffusivity and (C and F) effective CO_2 diffusivity plotted from the equatorial line of the individual pears in (top line) healthy and (bottom line) browning-affected conditions. A profile that drastically increases at certain position (*r/R*) is affected by a cavity.

References

Abdul-Baki, A.A., Solomos, T., 1994. Diffusivity of carbon dioxide through the skin and flesh of `Russet Burbank' potato tubers. J. Am. Soc. Hort. Sci. 119, 742–746. https://doi.org/10.21273/JASHS.119.4.742

Aguilera, J.M., Stanley, D.W., Baker, K.W., 2000. New dimensions in microstructure of food products. Trends in Food Science & Technology 11, 3–9. https://doi.org/10.1016/S0924-2244(00)00034-0

Aguilera, J.M., 2005. Why food microstructure?. Journal of Food Engineering 67, 3–11. https://doi.org/10.1016/j.jfoodeng.2004.05.050

Al-Raoush, R.I., Madhoun, I.T., 2017. TORT3D: A MATLAB code to compute geometric tortuosity from 3D images of unconsolidated porous media. Powder Technology 320, 99–107. https://doi.org/10.1016/j.powtec.2017.06.066

Alsleem, H., Davidson, R., 2013. Factors affecting contrast-detail performance in computed tomography: A Review. Journal of Medical Imaging and Radiation Sciences 44, 62–70. https://doi.org/10.1016/j.jmir.2012.12.001

Armstrong, W., 1979. Aeration in higher plants. Advances in Botanical Research 7, 225–332.

Azeredo, F., de Menezes, L.M., Enciso, R., Weissheimer, A., de Oliveira, R.B., 2013. Computed gray levels in multislice and cone-beam computed tomography. American Journal of Orthodontics and Dentofacial Orthopedics 144, 147–155. https://doi.org/10.1016/j.ajodo.2013.03.013

Bailey-Serres, J., Voesenek, L.A.C.J., 2008. Flooding stress: acclimations and genetic diversity. Annu. Rev. Plant Biol. 59, 313–339. https://doi.org/10.1146/annurev.arplant.59.032607.092752

Balafar, M.A., 2012. Review of noise reducing algorithms for brain MRI images. International Journal on Tecjnical and Physcial Problems of Engineering 4,54-59.

Barker, J., Khan, M.A.A., Solomos, T., 1964. Mechanism of the pasteur effect. Nature 201, 1126–1127. https://doi.org/10.1038/2011126a0

Beaudry, R.M., 1993. Effect of carbon dioxide partial pressure on blueberry fruit respiration and respiratory quotient. Postharvest Biology and Technology 3, 249–258. https://doi.org/10.1016/0925-5214(93)90060-G

Bessemans, N., Verboven, P., Verlinden, B.E., Janssens, M., Hertog, M.L.A.T.M., Nicolaï, B.M., 2020. Apparent respiratory quotient observed in headspace of static respirometers underestimates cellular respiratory quotient of pear fruit. Postharvest Biology and Technology 162, 111104. https://doi.org/10.1016/j.postharvbio.2019.111104

Bessemans, N., Verboven, P., Verlinden, B.E., Nicolaï, B.M., 2016. A novel type of dynamic controlled atmosphere storage based on the respiratory quotient (RQ-DCA). Postharvest Biology and Technology 115, 91–102. https://doi.org/10.1016/j.postharvbio.2015.12.019

Boeckx, J., Pols, S., Hertog, M.L.A.T.M., Nicolaï, B.M., 2019. Regulation of the central carbon metabolism in apple fruit exposed to postharvest low-oxygen stress. Front. Plant Sci. 10, 1384. https://doi.org/10.3389/fpls.2019.01384

Boersig, M.R., Kader, A.A., romani, R.J., 1988. Aerobic-anaerobic respiratory transition in pear fruit and cultured pear fruit cells. Journal of the American Society for Horticultural Science 113, 869–873.

Brady, C.J., Romani, R.J., 1988. Respiration and protein synthesis in nongrowing cultured pear fruit cells in response to ethylene and modified atmospheres: A Model System for Fruits Postharvest. Plant Physiol. 87, 571–576. https://doi.org/10.1104/pp.87.3.571

Brown, M., Brown, L., 2018. Lavin's radiography for veterinary technicians, sixth edition. ed. Elsevier

Cantre, D., Herremans, E., Verboven, P., Ampofo-Asiama, J., Nicolaï, B., 2014. Characterization of the 3-D microstructure of mango (*Mangifera indica* L. cv. Carabao) during ripening using X-ray computed microtomography. Innovative Food Science & Emerging Technologies 24, 28–39. https://doi.org/10.1016/j.ifset.2013.12.008

Chigwaya, K., Karuppanapandian, T., Schoeman, L., Viljoen, D.W., Crouch, I.J., Nugraha, B., Verboven, P., Nicolaï, B.M., Crouch, E.M., 2021a. X-ray CT and porosity mapping to determine the effect of 'Fuji' apple morphological and microstructural properties on the incidence of CO_2 induced internal browning. Postharvest Biology and Technology 174, 111464. https://doi.org/10.1016/j.postharvbio.2021.111464

Chigwaya, K., Plessis, A. du, Viljoen, D.W., Crouch, I.J., Crouch, E.M., 2021b. Use of X-ray computed tomography and 3D image analysis to characterize internal browning in 'Fuji' apples after exposure to CO_2 stress. Scientia Horticulturae 277, 109840. https://doi.org/10.1016/j.scienta.2020.109840

Choudhary, D., Mehta, A., 2010. Fruit crops. Oxford Book Co.

Clennell, M.B., 1997. Tortuosity: a guide through the maze. Geological Society, London, Special Publications 122, 299–344. https://doi.org/10.1144/GSL.SP.1997.122.01.18

Cohen, H., Szymanski, J., Aharoni, A., 2017. Assimilation of 'omics' strategies to study the cuticle layer and suberin lamellae in plants. Journal of Experimental Botany 68, 5389–5400. https://doi.org/10.1093/jxb/erx348

Currie, J.A., 1960. Gaseous diffusion in porous media. Part 2. -Dry granular materials. Journal of Applied Physics 11, 318–324. https://doi.org/10.1088/0508-3443/11/8/303

Dardick, C., Callahan, A.M., 2014. Evolution of the fruit endocarp: molecular mechanisms underlying adaptations in seed protection and dispersal strategies. Front. Plant Sci. 5. https://doi.org/10.3389/fpls.2014.00284

Davis, G.R., Elliott, J.C., 2006. Artefacts in X-ray microtomography of materials. Materials Science and Technology 22, 1011–1018. https://doi.org/10.1179/174328406X114117.

De Chiffre, L., Carmignato, S., Kruth, J.-P., Schmitt, R., Weckenmann, A., 2014. Industrial applications of computed tomography. CIRP Annals 63, 655–677. https://doi.org/10.1016/j.cirp.2014.05.011

Diels, E., Wang, Z., Nicolai, B., Ramon, H., Smeets, B., 2019. Discrete element modelling of tomato tissue deformation and failure at the cellular scale. Soft Matter 15, 3362–3378. https://doi.org/10.1039/C9SM00149B

Dražeta, L., Lang, A., Hall, A.J., Volz, R.K., Jameson, P.E., 2004. Air volume measurement of 'Braeburn' apple fruit. Journal of Experimental Botany 55, 1061–1069. https://doi.org/10.1093/jxb/erh118

Drew, M.C., 1997. Oxygen deficiency and root metabolism: injury and acclimation under hypoxia and anoxia. Annu. Rev. Plant. Physiol. Plant. Mol. Biol. 48, 223–250. https://doi.org/10.1146/annurev.arplant.48.1.223

Duan, Y., Xu, X., Wang, R., Ma, C., 2020. X-ray μCT analysis to characterize cork spot disorder in Chinese pear 'Chili' (*Pyrus bretschneideri*). Postharvest Biology and Technology 170, 111321. https://doi.org/10.1016/j.postharvbio.2020.111321

Edward, J.M., Roberts, T.H., Atwell, B.J. 2012, Quantifying ATP turnover in anoxic coleoptiles of rice (*Oryza sativa*) demonstrates preferential allocation of energy to protein synthesis. Journal of Experimental Botany 63, 4389-4402. doi:10.1093/jxb/ers114.

Fito, P., Chiralt, A., Betoret, N., Gras, M., Ch, M., Andr, A., 2001. Vacuum impregnation and osmotic dehydration in matrix engineering Application in functional fresh food development. Journal of Food Engineering 9, 175-183. https://doi.org/10.1016/S0260-8774(00)00220-X.

Fonseca, S.C., Oliveira, F.A.R., Brecht, J.K., 2002. Modelling respiration rate of fresh fruits and vegetables for modified atmosphere packages: a review. Journal of Food Engineering 52, 99–119. https://doi.org/10.1016/S0260-8774(01)00106-6

Franck, C., Lammertyn, J., Ho, Q.T., Verboven, P., Verlinden, B., Nicolaï, B.M., 2007. Browning disorders in pear fruit. Postharvest Biology and Technology 43, 1–13. https://doi.org/10.1016/j.postharvbio.2006.08.008

Fruit Logistica, 2020. European Statistics Handbook.

Gao, Z., Hu, Q., Liang, H., 2013. Gas diffusivity in porous media: determination by mercury intrusion porosimetry and correlation to porosity and permeability. J Por Media 16, 607–617. https://doi.org/10.1615/JPorMedia.v16.i7.30

Garrouch, Ali.A., Ali, L., Qasem, F., 2001. Using diffusion and electrical measurements to assess tortuosity of porous media. Ind. Eng. Chem. Res. 40, 4363–4369. https://doi.org/10.1021/ie010070u

Geigenberger, P., 2003. Response of plant metabolism to too little oxygen. Current Opinion in Plant Biology 6, 247–256. https://doi.org/10.1016/S1369-5266(03)00038-4

Ghanbarian, B., Hunt, A.G., Ewing, R.P., Sahimi, M., 2013. Tortuosity in porous media: A Critical Review. Soil Science Society of America Journal 77, 1461–1477. https://doi.org/10.2136/sssaj2012.0435

Gibbs, J., Greenway, H., 2003. Review: Mechanisms of anoxia tolerance in plants. I. Growth, survival and anaerobic catabolism. Functional Plant Biol. 30, 353. https://doi.org/10.1071/PP98095_ER

Gitman. I.M., Gitman, M.B., Askes, H., 2006. Quantification of stochastically stable representative volumes for random heterogeneous materials. Archive of Applied Mechanics 75, 79–92. https://doi.org/10.1007/s00419-005-0411-8

Goh, T.Y., Basah, S.N., Yazid, H., Aziz Safar, M.J., Ahmad Saad, F.S., 2018a. Performance analysis of image thresholding: Otsu technique. Measurement 114, 298–307. https://doi.org/10.1016/j.measurement.2017.09.052

Goldman, L.W., 2007. Principles of CT: Radiation dose and image Quality. Journal of Nuclear Medicine Technology 35, 213–225. https://doi.org/10.2967/jnmt.106.037846

Goñi, S.M., Purlis, E., Salvadori, V.O., 2007. Three-dimensional reconstruction of irregular foodstuffs. Journal of Food Engineering 82, 536–547. https://doi.org/10.1016/j.jfoodeng.2007.03.021

Goñi, S.M., Purlis, E., Salvadori, V.O., 2008. Geometry modelling of food materials from magnetic resonance imaging. Journal of Food Engineering 88, 561–567. https://doi.org/10.1016/j.jfoodeng.2008.03.020

Goodenough, D.J., Weaver, K.E., 1984. Factors related to low contrast resolution in CT scanners. Computerized Radiol. 8, 297–308. https://doi.org/10.1016/0730-4862(84)90042-8

Gran, C.D., Beaudry, R.M., 1993. Determination of the low oxygen limit for several commercial apple cultivars by respiratory quotient breakpoint. Postharvest Biology and Technology 3, 259–267. https://doi.org/10.1016/0925-5214(93)90061-7

Gras, M., Vidal-Brotóns, N., Betoret, A., Chiralt, Fito, P., 2002. The response of some vegetables to vacuum impregnation. Innovative Food Science & Emerging Technologies 3, 263–269. https://doi.org/10.1016/S1466-8564(02)00032-2

Guelpa, A., Manley, M., 2015. Non-destructive estimation of maize (*Zea mays* L.) kernel hardness by means of an X-ray micro-computed tomography (µCT) Density Calibration. Food Bioprocess Technol 11. https://doi.org/10.1007/s11947-015-1502-3.

Gueven, A., Hicsasmaz, Z., 2011. Geometric network simulation of high porosity foods. Applied Mathematical Modelling 35, 4824–4840. https://doi.org/10.1016/j.apm.2011.03.047

Gulliksrud, K., Stokke, C., Trægde Martinsen, A.C., 2014. How to measure CT image quality: Variations in CT-numbers, uniformity and low contrast resolution for a CT quality assurance phantom. Physica Medica 30, 521–526. https://doi.org/10.1016/j.ejmp.2014.01.006

Gunning, B.E.S., Steer, M.W., 1996. Plant cell biology: structure and function. Jones and Bartlett Publishers.

Gupta, A.K., Teja, A.S., Chai, X.S., Zhu, J.Y., 2000. Henry's constants of *n*-alkanols Žmethanol through n-hexanol. in water at temperatures between 40 ºC and 90 ºC. Food Phase Equilibria 170, 183-192. https://doi.org/10.1016/S0378-3812(00)00350-2

Herremans, E., Verboven, P., Defraeye, T., Rogge, S., Ho, Q.T., Hertog, M.L.A.T.M., Verlinden, B.E., Bongaers, E., Wevers, M., Nicolai, B.M., 2014a. X-ray CT for quantitative food microstructure engineering: The apple case. Nuclear Instruments and Methods in Physics Research Section B: Beam Interactions with Materials and Atoms 324, 88–94. https://doi.org/10.1016/j.nimb.2013.07.035

Herremans, E., Melado-Herreros, A., Defraeye, T., Verlinden, B., Hertog, M., Verboven, P., Val, J., Fernández-Valle, M.E., Bongaers, E., Estrade, P., Wevers, M., Barreiro, P., Nicolaï, B.M., 2014b. Comparison of X-ray CT and MRI of watercore disorder of different apple cultivars. Postharvest Biology and Technology 87, 42–50. https://doi.org/10.1016/j.postharvbio.2013.08.008

Herremans, E., Verboven, P., Verlinden, B.E., Cantre, D., Abera, M., Wevers, M., Nicolaï, B.M., 2015a. Automatic analysis of the 3-D microstructure of fruit parenchyma tissue using X-ray micro-CT explains differences in aeration. BMC Plant Biol 15, 264. https://doi.org/10.1186/s12870-015-0650-y

Herremans, E., Verboven, P., Hertog, M.L.A.T.M., Cantre, D., van Dael, M., De Schryver, T., Van Hoorebeke, L., Nicolaï, B.M., 2015b. Spatial development of transport structures in

apple (*Malus* × *domestica Borkh*.) fruit. Frontiers in Plant Science 6, 1–14. https://doi.org/10.3389/fpls.2015.00679

Hertog, M.L.A.T.M., Peppelenbos, H.W., Evelo, R.G., Tijskens, L.M.M., 1998. A dynamic and generic model of gas exchange of respiring produce: the effects of oxygen, carbon dioxide and temperature. Postharvest Biology and Technology 14, 335–349. https://doi.org/10.1016/S0925-5214(98)00058-1

Ho, Q.T., Verlinden, B.E., Verboven, P., Nicola, B.M., 2006a. Gas diffusion properties at different positions in the pear. Postharvest Biology and Technology 41, 113–120. https://doi.org/10.1016/j.postharvbio.2006.04.002

Ho, Q.T., Verlinden, B.E., Verboven, P., Vandewalle, S., Leuven, K.U., Computing, S., Leuven, K.U., 2006b. A permeation – diffusion – reaction model of gas transport in cellular tissue of plant materials. Journal of Experimental Botany 57, 4215–4224. https://doi.org/10.1093/jxb/erl198

Ho, Q.T., Verboven, P., Verlinden, B.E., Lammertyn, J., Vandewalle, S., Nicolaï, B.M., 2008. A Continuum Model for Metabolic Gas Exchange in Pear Fruit. PLoS Computational Biology 4, 13. https://doi.org/10.1371/journal.pcbi.1000023.

Ho, Q.T., Verboven, P., Mebatsion, H.K., Verlinden, B.E., Vandewalle, S., Nicolaï, B.M., 2009. Microscale mechanisms of gas exchange in fruit tissue. New Phytologist 182, 163–174. https://doi.org/10.1111/j.1469-8137.2008.02732.x

Ho, Q.T., Verboven, P., Verlinden, B.E., Nicolaï, B.M., 2010a. A model for gas transport in pear fruit at multiple scales. Journal of Experimental Botany 61, 2071–2081. https://doi.org/10.1093/jxb/erq026

Ho, Q.T., Verboven, P., Verlinden, B.E., Schenk, A., Delele, M.A., Rolletschek, H., Vercammen, J., Nicolaï, B.M., 2010b. Genotype effects on internal gas gradients in apple fruit. Journal of Experimental Botany 61, 2745–2755. https://doi.org/10.1093/jxb/erq108

Ho, Q.T., Verboven, P., Verlinden, B.E., Herremans, E., Wevers, M., Carmeliet, J., Nicolaï, B.M., 2011. A three-dimensional multiscale model for gas exchange in fruit. Plant physiology 155, 1158–1168. https://doi.org/10.1104/pp.110.169391

Ho, Q.T., Carmeliet, J., Datta, A.K., Defraeye, T., Delele, M.A., Herremans, E., Opara, L., Ramon, H., Tijskens, E., van der Sman, R., Van Liedekerke, P., Verboven, P., Nicolaï, B.M., 2013a. Multiscale modeling in food engineering. Journal of Food Engineering 114, 279–291. https://doi.org/10.1016/j.jfoodeng.2012.08.019

Ho, Q.T., Verboven, P., Verlinden, B.E., Schenk, A., Nicolaï, B.M., 2013b. Controlled atmosphere storage may lead to local ATP deficiency in apple. Postharvest Biology and Technology 78, 103–112. https://doi.org/10.1016/j.postharvbio.2012.12.014

Ho, Q.T., Verboven, P., Fanta, S.W., Abera, M.K., Retta, M.A., Herremans, E., Defraeye, T., Nicolaï, B.M., 2014. A Multiphase Pore Scale Network Model of Gas Exchange in Apple Fruit. Food Bioprocess Technol 7, 482–495. https://doi.org/10.1007/s11947-012-1043-y

Ho, Q.T., Rogge, S., Verboven, P., Verlinden, B.E., Nicolaï, B.M., 2016. Stochastic modelling for virtual engineering of controlled atmosphere storage of fruit. Journal of Food Engineering 176, 77–87. https://doi.org/10.1016/j.jfoodeng.2015.07.003

Ho, Q.T., Hertog, M.L.A.T.M., Verboven, P., Ambaw, A., Rogge, S., Verlinden, B.E., Nicolaï, B.M., 2018. Down-regulation of respiration in pear fruit depends on temperature. Journal of Experimental Botany 69, 2049–2060. https://doi.org/10.1093/jxb/ery031

Hsieh, J., 2009. Computed tomography: principles, design, artifacts, and recent advances, 2nd ed. Wiley Interscience ; SPIE Press, Hoboken, N.J. : Bellingham, Wash.

Huang, S., Ishizawa, K., Greenway, H., Colmer, T.D., 2005. Manipulation of ethanol production in anoxic rice coleoptiles by exogenous glucose determines rates of ion fluxes and provides estimates of energy requirements for cell maintenance during anoxia. Journal of Experimental Botany 56, 2453–2463. https://doi.org/10.1093/jxb/eri238

Huijs, S., Huysmans, T., de Jong, A., Arnout, N., Sijbers, J., Bellemans, J., 2018. Principal component analysis as a tool for determining optimal tibial baseplate geometry in modern TKA design. Acta Orthop. Belg 84, 452–460. PMID: 30879450.

Ireland, H.S., Yao, J.-L., Tomes, S., Sutherland, P.W., Nieuwenhuizen, N., Gunaseelan, K., Winz, R.A., David, K.M., Schaffer, R.J., 2013. Apple *SEPALLATA1/2* -like genes control fruit flesh development and ripening. Plant J 73, 1044–1056. https://doi.org/10.1111/tpj.12094.

Janssen, S., Verboven, P., Nugraha, B., Wang, Z., Boone, M., Josipovic, I., Nicolaï, B.M., 2020a. 3D pore structure analysis of intact 'Braeburn' apples using X-ray micro-CT. Postharvest Biology and Technology 159, 111014. https://doi.org/10.1016/j.postharvbio.2019.111014

Janssen, S., 2020b. Gas exchange in apple during controlled atmosphere storage. MeBioS, KU Leuven.

Kader, A.A., 1989. Mode of action of oxygen and carbon dioxide on postharvest physiology of "Bartlett" pears. Acta horticulturae 258, 161–167.

Kader, A., Saltveit, M., 2002. Respiration and Gas Exchange, in: Bartz, J. (Ed.), Postharvest Physiology and Pathology of Vegetables. CRC Press. https://doi.org/10.1201/9780203910092.ch2

Kalnin, J.R., Kotomin, E.A., Maier, J., 2002. Calculations of the effective diffusion coefficient for inhomogeneous media. Journal of Physics and Chemistry of Solids 63, 449–456. https://doi.org/10.1016/S0022-3697(01)00159-7.

Ke, D., Kader, A.A., 1990. Tolerance of `Valencia' oranges to controlled atmospheres, as determined by physiological responses and quality attributes. jashs 115, 779–783. https://doi.org/10.21273/JASHS.115.5.770.

Ke, D., Rodriguez-Sinobas, L., Kader, A.A., 1991. Physiology and prediction of fruit tolerance to low-oxygen atmospheres. jashs 116, 253–260. https://doi.org/10.21273/JASHS.116.2.253.

Ketcham, R.A., Hanna, R.D., 2014. Beam hardening correction for X-ray computed tomography of heterogeneous natural materials. Computers and Geosciences 67, 49–61. https://doi.org/10.1016/j.cageo.2014.03.003

Kierklo, A., Tabor, Z., Pawińska, M., Jaworska, M., 2015. A microcomputed tomography-based comparison of root canal filling quality following different instrumentation and obturation techniques. Med Princ Pract. 84, 84–91. https://doi.org/10.1159/000368307

Knee, M., G.S. Hatfield, S., 1976. A comparison of methods for measuring the volatile components of apple fruits. J. Fd Technol. 11, 485–493. https://doi.org/10.1111/j.1365-2621.1976.tb00748.x

Kowalska, G., 2008. Flowering biology of eggplant and procedures intensifying fruit set-Review. Acta Sci. Pol., Hortorum Cultus 7, 63–76.

Kruth, J.P., Bartscher, M., Carmignato, S., Schmitt, R., Chiffre, L. De, Weckenmann, A., 2011. CIRP Annals - Manufacturing Technology Computed tomography for dimensional metrology. CIRP Annals - Manufacturing Technology 60, 821–842. https://doi.org/10.1016/j.cirp.2011.05.006

Lammertyn, J., Aerts, M., Verlinden, B.E., Schotsmans, W., Nicolaï, B.M., 2000. Logistic regression analysis of factors influencing core breakdown in 'Conference' pears. Postharvest Biology and Technology 20, 25–37. https://doi.org/10.1016/S0925-5214(00)00114-9

Lammertyn, J., Scheerlinck, N., Verlinden, B.E., Schotsmans, W., Nicolaï, B.M., 2001. Simultaneous determination of oxygen diffusivity and respiration in pear skin and tissue. Postharvest biology and Technology 23, 93–104 https://doi.org/10.1016/S0925-5214(01)00113-2.

Lammertyn, J., Scheerlinck, N., Jancso, P., Verlinden, B.E., Nicolaï, B.M., 2003a. A respiration-A diffusion model for 'Conference' pears I: model development and validation Postharvest biology and Technology 30, 29–42. https://doi.org/10.1016/S0925-5214(03)00061-9

Lammertyn, J., Scheerlinck, N., Jancso, P., Verlinden, B.E., Nicolaï, B.M., 2003b. A respiration-A diffusion model for 'Conference' pears II: Simulations and relation to core breakdown. Postharvest biology and Technology 30, 43–55. https://doi.org/10.1016/S0925-5214(03)00062-0

Lammertyn, J., Dresselaers, T., Van Hecke, P., Jancsók, P., Wevers, M., Nicolaï, B.M., 2003c. MRI and x-ray CT study of spatial distribution of core breakdown in 'Conference' pears. Magnetic Resonance Imaging 21, 805–815. https://doi.org/10.1016/S0730-725X(03)00105-X

Lammertyn, J., Dresselaers, T., Van Hecke, P., Jancsók, P., Wevers, M., Nicolaï, B.M., 2003d. Analysis of the time course of core breakdown in 'Conference' pears by means of MRI and X-ray CT. Postharvest Biology and Technology 29, 19–28. https://doi.org/10.1016/S0925-5214(02)00212-0

Lech, K., Michalska, A., Wojdyło, A., Nowicka, P., Figiel, A., 2018. The influence of physical properties of selected plant materials on the process of osmotic dehydration. LWT - Food Science and Technology 91, 588–594. https://doi.org/10.1016/j.lwt.2018.02.012

Lee, D.S., Haggar, P.E., Lee, J., Yam, K.L., 1991. Model for Fresh Produce Respiration in Modified Atmospheres Based on Principles of Enzyme Kinetics. J Food Science 56, 1580–1585. https://doi.org/10.1111/j.1365-2621.1991.tb08645.x

Li, S., Qiao, C., Li, Z., Hui, Y., 2018. The effect of permeability on supercritical CO_2 diffusion coefficient and determination of diffusive tortuosity of porous media under reservoir conditions. Journal of CO_2 utilization 28, 1–14. https://doi.org/10.1016/j.jcou.2018.09.007

Liu, M., Bassetti, N., Petrasch, S., Zhang, N., Bucher, J., Shen, S., Zhao, J., Bonnema, G., 2019. What makes turnips: anatomy, physiology and transcriptome during early stages of its

hypocotyl-tuber development. Hortic Res 6, 38. https://doi.org/10.1038/s41438-019-0119-5.

Macdaniels, L.H., 1940. The morphology of the apple and other pome fruits. Memoirs. Cornell Agricultural Experiment Station 230, 32 pp

Mannapperuma, J.D., Singh, R.P., Montero, M.E., 1991. Simultaneous gas diffusion and chemical reaction in foods stored in modified atmospheres. Journal of Food Engineering 14, 167–183. https://doi.org/10.1016/0260-8774(91)90006-E

Marrero, T.R., Mason, E.A., 1972. Gaseous diffusion coefficients. Journal of Physical and Chemical Reference Data 1, 3–118. doi: https://doi.org/10.1063/1.3253094.

Martin, L.B.B., Rose, J.K.C., 2013. There's more than one way to skin a fruit: formation and functions of fruit cuticles. Journal of Experimental Botany 65, 4639–4651. https://doi.org/10.1093/jxb/eru301

Masschaele, B., Dierick, M., Loo, D. Van, Boone, M.N., 2013. HECTOR : A 240kV micro-CT setup optimized for research 012012. https://doi.org/10.1088/1742-6596/463/1/012012

Mditshwa, A., Fawole, O.A., Opara, U.L., 2018. Recent developments on dynamic controlled atmosphere storage of apples—A review. Food Packaging and Shelf Life 16, 59–68. https://doi.org/10.1016/j.fpsl.2018.01.011

Mebatsion, H.K., Verboven, P., Ho, Q.T., Verlinden, B.E., Nicolaï, B.M., 2008a. Modelling fruit (micro)structures, why and how? Trends in Food Science & Technology 19, 59–66. https://doi.org/10.1016/j.tifs.2007.10.003

Mebatsion, H K, Verboven, P., Jancsók, P.T., Ho, Q.T., Verlinden, B.E., Nicolaï, B.M., 2008b. Modeling 3d fruit tissue microstructure using a novel ellipsoid tessellation algorithm. Computer Modeling in Engineering and Science 29, 137-150. DOI:10.3970/cmes.2008.029.137.

Mebatsion, H.K., Verboven, P., Melese Endalew, A., Billen, J., Ho, Q.T., Nicolaï, B.M., 2009. A novel method for 3-D microstructure modeling of pome fruit tissue using synchrotron radiation tomography images. Journal of Food Engineering 93, 141–148. https://doi.org/10.1016/j.jfoodeng.2009.01.008

Meganck, Jeffrey A., Kozloff, K.M., Thornton, M.M., Broski, S.M., Goldstein, S.A., 2009. Beam hardening artifacts in micro-computed tomography scanning can be reduced by X-ray beam filtration and the resulting images can be used to accurately measure BMD. Bone 45, 1104–1116. https://doi.org/10.1016/j.bone.2009.07.078

Mendoza, F., Verboven, P., Mebatsion, H.K., Kerckhofs, G., Wavers, M., Nicolai, B., 2007. Three-dimensional pore space quantification of apple tissue using X-ray computed microtomography Planta 226, 559–570. https://doi.org/10.1007/s00425-007-0504-4.

Mendoza, F., Verboven, P., Ho, Q.T., Kerckhofs, G., Wevers, M., Nicolaï, B., 2010. Multifractal properties of pore-size distribution in apple tissue using X-ray imaging. Journal of Food Engineering 99, 206–215. https://doi.org/10.1016/j.jfoodeng.2010.02.021

Mezedur, M.M., Kaviany, M., Moore, W., 2002. Effect of pore structure , randomness and size on effective mass diffusivity. AIChe Journal 48. 15-24. doi: https://doi.org/10.1002/aic.690480104.

Millar, A.H., Whelan, J., Soole, K.L., Day, D.A., 2011. Organization and regulation of mitochondrial respiration in plants. Annu. Rev. Plant Biol. 62, 79–104. https://doi.org/10.1146/annurev-arplant-042110-103857

Moustakides, G., Briassoulis, D., Psarakis, E., Dimas, E., 2000. 3D image acquisition and NURBS based geometry modelling of natural objects. Advances in Engineering Software 31, 955–969. https://doi.org/10.1016/S0965-9978(00)00060-0

Mu, D., Liu, Z.-S., Huang, C., Djilali, N., 2007. Prediction of the effective diffusion coefficient in random porous media using the finite element method. J Porous Mater 14, 49–54. https://doi.org/10.1007/s10934-006-9007-0

Musse, M., Guio, F. De, Quellec, S., Cambert, M., Challois, S., Davenel, A., 2010. Quantification of microporosity in fruit by MRI at various magnetic fields: comparison with X-ray microtomography. Magnetic Resonance Imaging 28, 1525–1534. https://doi.org/10.1016/j.mri.2010.06.028

Muziri, T., Theron, K.I., Cantre, D., Wang, Z., Verboven, P., Nicolai, B.M., Crouch, E.M., 2016. Microstructure analysis and detection of mealiness in 'Forelle' pear (*Pyrus communis* L.) by means of X-ray computed tomography. Postharvest Biology and Technology 120, 145–156. https://doi.org/10.1016/j.postharvbio.2016.06.006

Navarre-Sitchler, A., Steefel, C.I., Yang, L., Tomutsa, L., Brantley, S.L., 2009. Evolution of porosity and diffusivity associated with chemical weathering of a basalt clast. J. Geophys. Res. 114, F02016. https://doi.org/10.1029/2008JF001060

Neale, G.H., Nader, W.K., 1973. Prediction of transport processes within porous media: diffusive flow processes within an homogeneous swarm of spherical particles. AIChE Journal 19, 112-119. doi: https://doi.org/10.1002/aic.690190116.

Nishida, C., Uauy, R., Kumanyika, S., Shetty, P., 2004. The Joint WHO/FAO Expert Consultation on diet, nutrition and the prevention of chronic diseases: process, product and policy implications. Public Health Nutr. 7, 245–250. https://doi.org/10.1079/PHN2003592

Nugraha, B., Verboven, P., Janssen, S., Wang, Z., Nicolaï, B.M., 2019. Non-destructive porosity mapping of fruit and vegetables using X-ray CT. Postharvest Biology and Technology 150, 80–88. https://doi.org/10.1016/j.postharvbio.2018.12.016

Otsu, N., 1979. A treshold selection method from gray-level histograms. IEEE Transactions on Systems, Man and Cybernetics 9, 62-66. doi: 10.1109/TSMC.1979.4310076.

Ozuna, C., Álvarez-Arenas, T.G., Riera, E., Cárcel, J.A., Garcia-Perez, J. V., 2014. Influence of material structure on air-borne ultrasonic application in drying. Ultrasonics Sonochemistry 21, 1235–1243. https://doi.org/10.1016/j.ultsonch.2013.12.015

Ögren, E., 1990. Evaluation of chlorophyll fluorescence as a probe for drought stress in willow leaves. Plant Physiol. 93, 1280–1285. https://doi.org/10.1104/pp.93.4.1280.

Pedreschi, R., Franck, C., Lammertyn, J., Erban, A., Kopka, J., Hertog, M., Verlinden, B., Nicolaï, B., 2009. Metabolic profiling of 'Conference' pears under low oxygen stress. Postharvest Biology and Technology 51, 123–130. https://doi.org/10.1016/j.postharvbio.2008.05.019

Peng, S., Hu, Q., Hamamoto, S., 2012. Diffusivity of rocks: Gas diffusion measurements and correlation to porosity and pore size distribution: Gas diffusion and rock porosity and pore size. Water Resour. Res. 48. https://doi.org/10.1029/2011WR011098

Peppelenbos, H.W., Leven, J. Van, 1996a. Evaluation of four types of inhibition for modelling the influence of carbon dioxide on oxygen consumption of fruits and vegetables. Postharvest Biology and Technology 7, 27–40 https://doi.org/10.1016/0925-5214(96)80995-1.

Peppelenbos, H.W., Tijskens, L.M.M., van 't Leven, J., Wilkinson, E.C., 1996b. Modelling oxidative and fermentative carbon dioxide production of fruits and vegetables. Postharvest Biology and Technology 9, 283–295. https://doi.org/10.1016/S0925-5214(96)00029-4.

Perez, R., Beaudry, R.M., 1998. Fractional surface coating modifies gas diffusion and ripening in bananas. J. Amer. Soc. Hort. Sci 123, 115–118. https://doi.org/10.21273/JASHS.123.1.115

Puig, A., Perez-Munuera, I., Carcel, J.A., Hernando, I., Garcia-Perez, J.V., 2012a. Moisture loss kinetics and microstructural changes in eggplant (*Solanum melongena* L.) during conventional and ultrasonically assisted convective drying. Food and Bioproducts Processing 90, 624–632. https://doi.org/10.1016/j.fbp.2012.07.001

Rajapakse, N.C., Banks, N.H., Hewett, E.W., Cleland, D.J., 1990. Development of oxygen concentration gradients in flesh tissues of bulky plant organs. jashs 115, 793–797. https://doi.org/10.21273/JASHS.115.5.793

Rashapov, R.R., Gostick, J.T., 2016. In-plane effective diffusivity in PEMFC gas diffusion layers. Transp Porous Med 115, 411–433. https://doi.org/10.1007/s11242-016-0648-4

Raven, J., 1996. Into the voids: the distribution, function, development and maintenance of gas spaces in plants. Annals of Botany 78, 137–142. https://doi.org/10.1006/anbo.1996.0105

Rawyler, A., Pavelic, D., Gianinazzi, C., Oberson, J., Braendle, R., 1999. Membrane lipid integrity relies on a threshold of atp production rate in potato cell cultures submitted to anoxia. Plant Physiol. 120, 293–300. https://doi.org/10.1104/pp.120.1.293

Rich, P.R., 2003. The molecular machinery of Keilin's respiratory chain. Biochemical Society Transactions 31, 1095–1105. https://doi.org/10.1042/bst0311095

Ritschl, L., Bergner, F., Fleischmann, C., Kachelrieß, M., 2010. Water calibration for CT scanners with tube voltage modulation. Phys. Med. Biol. 55, 4107–4117. https://doi.org/10.1088/0031-9155/55/14/010

Roberts, J.K.M., Callis, J., Wemmer, D., Walbot, V., Jardetzky, O., 1984. Mechanism of cytoplasmic pH regulation in hypoxic maize root tips and its role in survival under hypoxia. Proc. Natl. Acad. Sci. USA 81, 3379-3383. doi: 10.1073/pnas.81.11.3379.

Rogge, S., Defraeye, T., Herremans, E., Verboven, P., Nicolaï, B.M., 2015. A 3D contour based geometrical model generator for complex-shaped horticultural products. Journal of Food Engineering 157, 24–32. https://doi.org/10.1016/j.jfoodeng.2015.02.006

Russ, J.C., 2015. Image Analysis of Foods: Image analysis of foods. Journal of Food Science 80, E1974–E1987. https://doi.org/10.1111/1750-3841.12987

Saenmuang, S., Al-Haq, M.I., Samarakoon, H.C., Makino, Y., Kawagoe, Y., Oshita, S., 2012. Evaluation of Models for Spinach Respiratory Metabolism Under Low Oxygen Atmospheres. Food Bioprocess Technol 5, 1950–1962. https://doi.org/10.1007/s11947-010-0503-5

Sander, R., 2015. Compilation of Henry's law constants for water as solvent (version 4.0). Atmospheric Chemistry and Physics 15, 4399–4981.

Salvo, L., Cloetens, P., Maire, E., Zabler, S., Blandin, J.J., Buffière, J.Y., Ludwig, W., Boller, E., Bellet, D., Josserond, C., 2003. X-ray micro-tomography an attractive characterisation technique in materials science. Nuclear Instruments and Methods in Physics Research

Section B: Beam Interactions with Materials and Atoms 200, 273–286. https://doi.org/10.1016/S0168-583X(02)01689-0

Schotsmans, W., Verlinden, B.E., Lammertyn, J., Nicolaï, B.M., 2003. Simultaneous measurement of oxygen and carbon dioxide diffusivity in pear fruit tissue. Postharvest Biology and Technology 29, 155–166. https://doi.org/10.1016/S0925-5214(02)00251-X

Segal, E., Ellingson, W.A., Segal, Y., Zmora, I., 1987. A linearization beam-hardening correction method for X-ray computed tomographic imaging of structural ceramics, in: Thompson, D.O., Chimenti, D.E. (Eds.), Review of Progress in Quantitative Nondestructive Evaluation. Springer US, Boston, MA, pp. 411–419. https://doi.org/10.1007/978-1-4613-1893-4_47

Seeram, E., 2010. Computed tomography: physical principles and recent technical advances. Journal of Medical Imaging and Radiation Sciences 41, 87–109. https://doi.org/10.1016/j.jmir.2010.04.001

Shaw, C. C., 2014. Cone beam computed tomography (imaging in medical diagnosis and therapy). CRC Press, Taylor & Francis Group, New York

Shen, L., Chen, Z., 2007. Critical review of the impact of tortuosity on diffusion 62, 3748–3755. https://doi.org/10.1016/j.ces.2007.03.041

Silva, M.A., Kerkhof, P.J.A.M., Coumans, W.J., 2000. Estimation of effective diffusivity in drying of heterogeneous porous media. Ind. Eng. Chem. Res. 39, 1443–1452. https://doi.org/10.1021/ie990563n

Smith, S.W., 1999. The scientist and engineer's guide to digital signal processing. California Technical Pub., San Diego, Calif.

Solomon, C., Breckon, T., 2011. Fundamentals of Digital Image Processing 355.

Sun, W., Chen, S.-L., Xu, M., Wei, Y., Fan, T., Huang, L., Ma, B., Guo, J., 2019. The measurements of the intrinsic diffusivity in pores and surface diffusivity inside the porous materials in liquid phase. Chemical Engineering Science 196, 176–187. https://doi.org/10.1016/j.ces.2018.11.006

Tadege, M., 1999. Ethanolic fermentation: new functions for an old pathway. Trends in Plant Science 4, 320–325. https://doi.org/10.1016/S1360-1385(99)01450-8

Tan, Ye, Kiekens, K., Welkenhuyzen, F., Kruth, J., Dewulf, W., 2012. Beam hardening correction and its influence on the measurement accuracy and repeatability for CT dimensional metrology applications 355–362.

Tanaka, Fumihiko, Imamura, K., Tanaka, Fumina, Uchino, T., 2018a. Determination of thermal diffusivity of persimmon flesh tissue using three-dimensional structure model based on X-ray computed tomography. Journal of Food Engineering 221, 151–157. https://doi.org/10.1016/j.jfoodeng.2017.10.021

Thewes, F.R, Brackmann, A., Both, V., Anese, R. de O., Schultz, E.E., Ludwig, V., Wendt, L.M., Berghetti, M.R.P., Thewes, Flavio Roberto, 2020. Dynamic controlled atmosphere based on carbon dioxide production (DCA – CD): Lower oxygen limit establishment, metabolism and overall quality of apples after long-term storage. Postharvest Biology and Technology 168, 111285. https://doi.org/10.1016/j.postharvbio.2020.111285

Tjaden, B., Cooper, S.J., Brett, D.J., Kramer, D., Shearing, P.R., 2016. On the origin and application of the Bruggeman correlation for analysing transport phenomena in

electrochemical systems. Current Opinion in Chemical Engineering 12, 44–51. https://doi.org/10.1016/j.coche.2016.02.006

Tomadakis, Manolis M., Sotirchos, S.V., 1993. Ordinary and transition regime diffusion in random fiber structures. AIChE J. 39, 397–412. https://doi.org/10.1002/aic.690390304

Toro, G., Pinto, M., 2015. Plant respiration under low oxygen. Chilean J. Agric. Res. 75, 57–70. https://doi.org/10.4067/S0718-58392015000300007

Troeh, F.R., Jabro, J.D., Kirkham, D., 1982. Gaseous diffusion equations for porous materials. Geoderma 27, 239–253. https://doi.org/10.1016/0016-7061(82)90033-7

Uchida, K., Matsuyama, K., Tanaka, K., Doi, K., 1992. Diffusion coefficient for O_2 in plasma and mitochondrial membranes of rat cardiomyocytes. Respiration Physiology 90, 351–362. https://doi.org/10.1016/0034-5687(92)90114-C

Ukrainczyk, N., Koenders, E.A.B., 2014. Representative elementary volumes for 3D modeling of mass transport in cementitious materials Representative elementary volumes for 3D modeling of mass transport in cementitious materials. https://doi.org/10.1088/0965-0393/22/3/035001

USDA, 2015. 2015-2020 Dietary guidelines for Americans. https://health.gov/our-work/food-nutrition/previous-dietary-guidelines/2015

Valle-Guadarrama, S., Saucedo-Veloz, C., Peña-Valdivia, C.B., Corrales-García, J.J.E., Chávez-Franco, S.H., 2004. Aerobic-anaerobic metabolic transition in 'Hass' avocado fruits. Food sci. technol. int. 10, 391–398. https://doi.org/10.1177/1082013204049488

van Dael, M., Verboven, P., Dhaene, J., Van Hoorebeke, L., Sijbers, J., Nicolai, B., 2017. Multisensor X-ray inspection of internal defects in horticultural products. Postharvest Biology and Technology 128, 33–43. https://doi.org/10.1016/j.postharvbio.2017.02.002

van Dongen, J.T., Gupta, K.J., Ramírez-Aguilar, S.J., Araújo, W.L., Nunes-Nesi, A., Fernie, A.R., 2011. Regulation of respiration in plants: A role for alternative metabolic pathways. Journal of Plant Physiology 168, 1434–1443. https://doi.org/10.1016/j.jplph.2010.11.004

Veltman, R.H., 2002. On the origin of internal browning in pears (*Pyrus communis* L. cv Conference). Thesis. https://edepot.wur.nl/199019.

Veltman, R.H., Lenthéric, I., Van der Plas, L.H.W., Peppelenbos, H.W., 2003. Internal browning in pear fruit (*Pyrus communis* L. cv Conference) may be a result of a limited availability of energy and antioxidants. Postharvest Biology and Technology 28, 295–302. https://doi.org/10.1016/S0925-5214(02)00198-9

Veraverbeke, E.A., Verboven, P., Van Oostveldt, P., Nicolaï, B.M., 2003. Prediction of moisture loss across the cuticle of apple (*Malus sylvestris* subsp. mitis (Wallr.)) during storage. Postharvest Biology and Technology 30, 75–88. https://doi.org/10.1016/S0925-5214(03)00083-8

Verboven, P., Kerckhofs, G., Mebatsion, H.K., Ho, Q.T., Temst, K., Wevers, M., Cloetens, P., Nicolaï, B.M., 2008. Three-Dimensional Gas Exchange Pathways in Pome Fruit Characterized by Synchrotron X-Ray Computed Tomography. Plant Physiol. 147, 518–527. https://doi.org/10.1104/pp.108.118935

Verboven, P., Pedersen, O., Herremans, E., Ho, Q.T., Nicolaï, B.M., Colmer, T.D., Teakle, N., 2012. Root aeration via aerenchymatous phellem: three-dimensional micro-imaging and

radial O_2 profiles in Melilotus siculus. New Phytologist 193, 420–431. https://doi.org/10.1111/j.1469-8137.2011.03934.x

Vincent, V., 2019. Imaging and modeling of the microstructure of frozen foods during recrystallization and sblimation: A case study on plant-based products. KU Leuven-AgroParisTech.

Vogel, H.-J., 2002. Topological characterization of porous media, in: mecke, k., stoyan, d. (eds.), morphology of condensed matter, lecture notes in physics. Springer Berlin Heidelberg, Berlin, Heidelberg, pp. 75–92. https://doi.org/10.1007/3-540-45782-8_3

Wallace, T.C., Bailey, R.L., Blumberg, J.B., Burton-Freeman, B., Chen, C.O., Crowe-White, K.M., Drewnowski, A., Hooshmand, S., Johnson, E., Lewis, R., Murray, R., Shapses, S.A., Wang, D.D., 2020. Fruits, vegetables, and health: A comprehensive narrative, umbrella review of the science and recommendations for enhanced public policy to improve intake. Critical Reviews in Food Science and Nutrition 60, 2174–2211. https://doi.org/10.1080/10408398.2019.1632258

Wang, Z., Verboven, P., Nicolai, B., 2017. Contrast-enhanced 3D micro-CT of plant tissues using different impregnation techniques. Plant Methods 13, 105. https://doi.org/10.1186/s13007-017-0256-5

Wang, Z., Van Beers, R., Aernouts, B., Watté, R., Verboven, P., Nicolaï, B., Saeys, W., 2020. Microstructure affects light scattering in apples. Postharvest Biology and Technology 159, 110996. https://doi.org/10.1016/j.postharvbio.2019.110996

Wills, R., Golding, J., 2016. Postharvest: An introduction to the physiology and handling of fruit and vegetables. 6th Edition

Winisdorffer, G., Musse, M., Quellec, S., Devaux, M., Lahaye, M., Mariette, F., 2015. MRI investigation of subcellular water compartmentalization and gas distribution in apples Parenchyma Seeds Vascular. Magnetic Resonance Imaging 33, 671–680. https://doi.org/10.1016/j.mri.2015.02.014

Wright, H., DeLong, J., Harrison, P.A., Gunawardena, A.H.L.A.N., Prange, R., 2010. The effect of temperature and other factors on chlorophyll a fluorescence and the lower oxygen limit in apples (*Malus domestica*). Postharvest Biology and Technology 55, 21–28. https://doi.org/10.1016/j.postharvbio.2009.07.011

Yamauchi, T., Colmer, T.D., Pedersen, O., Nakazono, M., 2018. Regulation of root traits for internal aeration and tolerance to soil waterlogging-flooding stress. Plant Physiol. 176, 1118–1130. https://doi.org/10.1104/pp.17.01157

Yan, C., Yin, M., Zhang, N., Jin, Q., Fang, Z., Lin, Y., Cai, Y., 2014. Stone cell distribution and lignin structure in various pear varieties. Scientia Horticulturae 174, 142–150. https://doi.org/10.1016/j.scienta.2014.05.018

Yearsley, C.W., Banks, N.H., Ganesh, S., 1997. Temperature effects on the internal lower oxygen limits of apple fruit. Postharvest Biology and Technology 11, 73–83. https://doi.org/10.1016/S0925-5214(97)00019-7

Yearsley, C.W., Banks, N.H., Ganesh, S., Cleland, D.J., 1996. Determination of lower oxygen limits for apple fruit. Postharvest Biology and Technology 8, 95–109. https://doi.org/10.1016/0925-5214(96)00064-6

Zaki, H.E.M., Takahata, Y., Yokoi, S., 2012. Analysis of the morphological and anatomical characteristics of roots in three radish (*Raphanus sativus*) cultivars that differ in root

shape. Journal of Horticultural Science and Biotechnology 87, 172–178. https://doi.org/10.1080/14620316.2012.11512849

Zhang, J., Bunn, J., 2000. Oxygen diffusivities of apple flesh and skin. Transactions of the ASAE 43, 359–363. https://doi.org/10.13031/2013.2712

Zhang, N., Zhao, J., Lens, F., de Visser, J., Menamo, T., Fang, W., Xiao, D., Bucher, J., Basnet, R.K., Lin, K., Cheng, F., Wang, X., Bonnema, G., 2014. Morphology, carbohydrate composition and vernalization response in a genetically diverse collection of asian and european turnips (*Brassica rapa subsp. rapa*). PLoS ONE 9, e114241. https://doi.org/10.1371/journal.pone.0114241

Zou, W., Hunter, N., Swain, M.V., 2011. Application of polychromatic μCT for mineral density determination. J Dent Res 90, 18–30. https://doi.org/10.1177/0022034510378429

List of publication and conference

Publications

Nugraha, B., Verboven, P., Janssen, S., Wang, Z., Verboven, P. Nicolaï, B. (2019). *Non-destructive porosity mapping of fruit and vegetables using X-Ray CT*. Postharvest Biology and Technology, 150, 80-89. doi: 10.1016/J.Postharvbio.2018.12.016

Nugraha, B., Verboven, P., Janssen, S., Hertog, M.L.A.T.M., Boone, M., Josipovic, I., Nicolaï, B. M. 2021. *Oxygen diffusivity mapping of fruit and vegetables based on X-ray CT*. Journal of Food Engineering. doi: https://doi.org/10.1016/j.jfoodeng.2021.110640

Janssen, S., Verboven, P., **Nugraha, B.,** Wang, Z., Boone, M., Josipovic, I., Nicolaï, B.M. (2020). *3-D pore structure analysis of intact 'Braeburn' apples using X-ray micro-CT*. Postharvest Biology and Technology, 159, doi: 10.1016/j.postharvbio.2019.111014

Chigwaya, K., Karuppanapandian, T., Schoeman, L., Viljoen D.W., Crouch, I.J., **Nugraha, B.,** Verboven, P., Nicolaï, B.M. (2021). *X-ray CT and porosity mapping to determine the effect of 'Fuji' apple morphological and microstructural properties on the incidence of CO_2 induced internal browning*. Postharvest Biology and Technology, 174. doi: doi.org/10.1016/j.postharvbio.2021.111464

International conferences

Nugraha, B., Verboven, P., Janssen, S., Wang, Z., Nicolai, B. (2018). Non-destructive porosity mapping of fruit and vegetables using X-Ray CT. Presented at 32nd EFFoST International Conference, Nantes, France, 06 Nov 2018-09 Nov 2018. **Poster**

Janssen, S., Wang, Z., **Nugraha, B.,** Piovesan, A., Boone, M., Josipovic, I., Verboven, P., Nicolai, B. (2018). 3-D pore network quantification of apples using X-ray CT of the microstructure of intact fruit. Presented at 32nd EFFoST International Conference, Nantes, France, 06-08 Nov 2018. **Poster**

Nugraha, B., Verboven, P., Janssen, S., Nicolaï, B. (2019). Respiratory gas diffusivity mapping of horticultural product using X-ray CT. Presented at Model-IT Conference 2019, Molfetta, Italy, 09-12 Jun 2019. **Oral presentation**. Proceeding: https://doi.org/10.17660/ActaHortic.2021.1311.35

Nugraha, B., Verboven, P., Janssen, S., Nicolaï, B. (2019). How respiratory gas diffusivity correlates with porosity of plant organ tissues. Presented at 3rd International Symposium on Agrocultural and Biosystem Engineering, Makassar, Indonesia, 06-08 August 2019. **Oral presentation.** Proceeding: https://doi.org/10.1088/1755-1315/355/1/012052

Nugraha, B., Verboven, P., Janssen, S., Nicolaï, B. (2021). A technique to map diffusivity in fruit and vegetable organs. Presented at XIIIth International Controlled and Modified Atmosphere Research Conference (CAMA2021), Leuven, Belgium, 15-18 August 2021. **Oral presentation.** Proceeding: *not available yet.*

FACULTY OF BIOSCIENCE ENGINEERING
DEPARTMENT OF BIOSYSTEMS
MECHATRONICS, BIOSTATISTICS AND SENSORS (MEBIOS) DIVISION
Willem de Croylaan 42
B-3001 LEUVEN, BELGIUM
bayu.nugraha@kuleuven.be
https://www.biw.kuleuven.be/